Olivine as a Probe into the Early Thermal Histories of Solar System Samples

A DISSERTATION SUBMITTED TO THE GRADUATE DIVISION OF THE
UNIVERSITY OF HAWAIʻI AT MĀNOA IN PARTIAL FULFILLMENT OF THE
REQUIREMENTS FOR THE DEGREE OF

DOCTOR OF PHILOSOPHY

IN

GEOLOGY AND GEOPHYSICS

December 2023

By

William Scott Nelson

Dissertation Committee:

Julia Hammer, Chairperson

Thomas Shea

Gary Huss

Hope Ishii

Ralf Kaiser, University representative

Acknowledgements

I have worked for about five years on the contents of this thesis. That is, without a doubt, the most time I have put into a single document. I love this research, whether it be sitting in front of my computer struggling to get a piece of code to run like I want it to, spending God knows how many hours tinkering with the microprobe, or sitting in the lab figuring out just what is happening to my experiments when I shoot them up to high temperature (and where my rhenium is going?!). This love is obviously tied to a reasonable degree of struggle. Struggle is not easily overcome alone, and I have found myself surrounded by people who have supported me and got me through the frustrations, mistakes, and self-doubt that malign any endeavor like this.

First, foremost, and above anyone, is my family. Whether it is talking about my problems to my parents, playing games with my brother on a Saturday night, or having my father walk me through finances, they have had the largest impact on this dissertation. Both through emotional as well as direct support. There is no way this thesis would exist without their presence. When the second chapter of this thesis was published, I was thrown into the deep end of answering interviewers' questions and trying to communicate to the general public. Luckily, my aunt, with her scientific journalism chops provided me with valuable tips to avoid making too much of a fool of myself.

I want to thank those who helped me find my love of this science. Bruce Geller brought me on as a high school volunteer for his mineralogy museum and let me find my love of teaching and mineralogy. Elenor Camann introduced me to geology and keeps up with me all the while. Brian Hynek introduced me to planetary geology and had me research under him for several years in college, letting me explore my interests and develop my first scientific programming skills that I use so heavily in my research.

Sarah Black gave me so much advice as I transitioned from undergrad to grad school, and accidentally introduced me to experimental petrology.

The list of my friends who have gotten me here is far too large to list. I frankly had very few friends through most of my childhood and was blown away with the caring community that greeted me here, acting as a family away from my family. Dinner, hikes, game nights, scuba dives, free dives and beach days kept me sane. The cohort of both EARTH and HIGP graduate students are and will remain my closest friends. I especially want to note Rebecca deGraffenried, who was a ceaseless font of advice and ideas. Even years after she graduated, she still pops up in my life and is willing to talk.

I want to add a more somber acknowledgement to Dr. Mac Rutherford who passed away this year. He played a substantial role in a portion of this thesis that had to be cut but was one of my favorite projects I have ever worked on. I hope to move forward with this research, if it is at all possible, if only to honor the man who put so much effort into it. I only got to meet Mac two years ago, but he had a profound impact on me. Beyond the inherent impact of being my advisor's postdoc advisor, he was willing to not only help me with my own research, but train me in many different methods, and introduce me to his scientific community. He even allowed me to stay with him when I went to his institution for research. He showed me a role model for a lifelong love of science, and provided a sense of altruism and kindness that permeated every interaction I had with him. If I can become half the scientist and man Mac was, I will be content.

My committee has given me so much guidance. I hope all of you can see how you have changed how I think and have guided me to improve. I especially want to thank Thomas Shea, who practically served as a second advisor, and whose sense of humor have helped calm my nerves even when I have been at my most stressed (that

Bulbasaur question in my comps probably stopped me from passing out during the intermission).

Finally, I want to acknowledge Julia Hammer, my advisor and mentor over the past five years. I was so lucky that she happened to contact me when I was graduating. She has been unreasonably patient with me over these years and has taught me more than she knows. Our meetings that always drifted off topic and usually went at least an hour long were always a highlight. I know I still have so much to learn in this field, but most of what I do know is because of her. I can’t imagine getting a better advisor.

Abstract

Clues of our solar system's history exist in igneous rocks that exist on every terrestrial body in the solar system. Temperature is one of the most important variables to describe and infer the formation and evolution of these rocks. If the temperatures a rock has experienced throughout its formation are known, we can gain a substantial understanding of the processes and conditions behind a rock and its surroundings. This thesis explores the utilization of the heterogeneous distribution of trace elements in olivine to reconstruct the high-temperature thermal histories of igneous rocks. A study of Apollo troctolite 76535 reveals comparatively rapid cooling timescales and demonstrates how one can use diffusive relaxation of heterogeneities to determine the maximum cooling timescales even with minimal constraints on high-temperature cooling rates. This study finds that phosphorus in olivine displays less diffusive relaxation than expected. So, we investigate the diffusive behavior of this element in olivine, both through models and in the lab. We find no evidence of phosphorus heterogeneities diffusively relaxing when reheated. So, we investigate these heterogeneities using nanoscale microscopy. We find these heterogeneities are many orders of magnitude smaller than previously assumed and determine a plausible accommodation mechanism that would explain a lack of diffusive relaxation. Finally, we investigate the relative cooling histories of porphyritic and barred olivine chondrules using a variety of other systems, demonstrating how one can use these methods even when uncertain about the environment, diffusivity of the element, and temperature. Altogether, this dissertation discusses how trace elements behave in olivine and how they can be used to reveal the high-temperature thermal histories of olivine crystals.

Table of Contents

List of tables

List of figures

List of key abbreviations and symbols

D_x	Diffusivity of element x. Unless otherwise stated, this is the diffusivity of the element x in olivine.
EPMA	Electron probe microanalysis
SEM	Scanning electron microscope
PPL	Plane polarized light microscopy
XPL	Crossed polarized light microscopy
SEI	Secondary electron image
BSE	Backscattered electron image
WDS	Wavelength dispersive spectroscopy
EDS	Energy dispersive spectroscopy
EBSD	Electron backscatter diffraction
TEM	Transmission electron microscopy
APT	Atom probe tomography
CL	Cathodoluminescence (referring to images produced in SEM)
LMO	Lunar magma ocean
KREEP	Potassium rare earth element and phosphorus – markers of interaction with late-stage lunar melts
Ur-KREEP	The late-stage lunar melt postulated to impart KREEP signatures
CDM	Comparative diffusion models
DDE	Diffusion dwell experiments
Ol	Olivine
Pl	Plagioclase
Pyx	Pyroxene
Fo	Forsterite
Fa	Fayalite
PCO	Pine canyon olivine
GP	Golden pumice
ORT	Olivine rich troctolite
KV	Kröger-Vink notation
$_{oct}$	Octahedral site (in olivine)
$_{tet}$	Tetrahedral site (in olivine)
$_{i}$	Interstitial ion
□	Vacancy
•	Positive charge defect
′	Negative charge defect
PO	Porphyritic olivine (chondrule)
POP	Porphyritic olivine and pyroxene (chondrule)
BO	Barred olivine (chondrule)

Chapter 1: Introduction

1.1 Olivine

Olivine ($(Mg,Fe)_2SiO_4$) is among the most common minerals throughout the solar system (Basaltic Volcanism Study project, 1981; Chakraborty, 2010). Olivine is an orthosilicate that crystallizes in the orthorhombic system (Dana & Ford, 1932; Deer et al., 1966). It is composed of silica tetrahedra and octahedrally coordinated cations and anions (oxygen) packed in a hexagonal close-packed (HCP) structure (Condit, 1985; Kingery et al., 1976; Figure 1.1). These cations can include Mg, Fe^{2+}, Mn, Cr^{2+}, Ni^{2+}, and others, but by far the most common olivines are in the forsterite (Mg_2SiO_4)- fayalite (Fe_2SiO_4) series, which form a complete solid solution between endmembers (Dana & Ford, 1932; Deer et al., 1966).

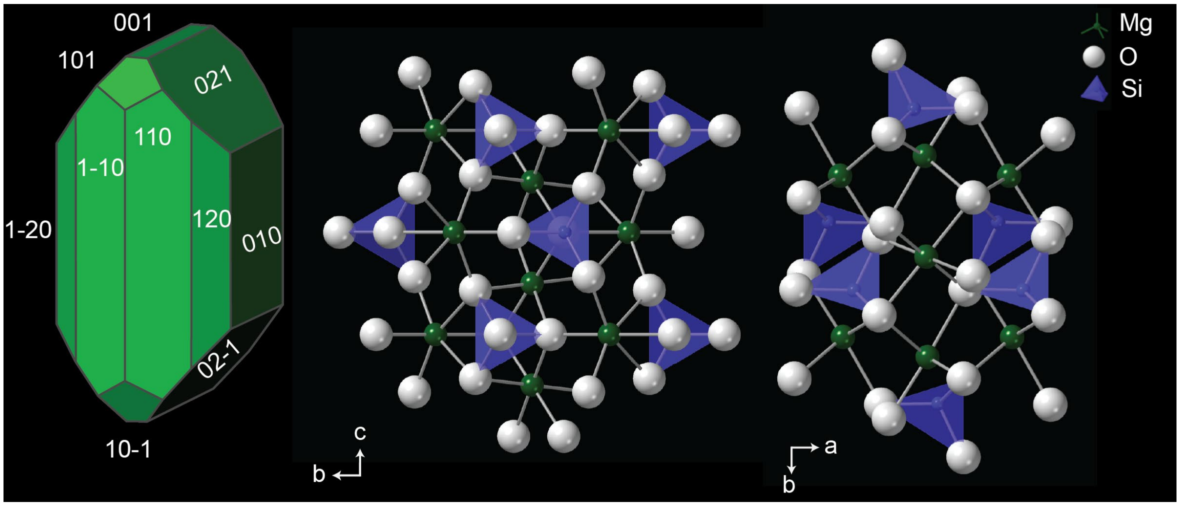

Figure 1.1: Typical olivine structure. On the left are common crystal faces of olivine, with labeled Miller indices, and on the right are ball-and-stick models of forsterite's crystal structure, with orientations relative to a=[100], b=[010], c=[001] labeled.

Olivine can occur in igneous (e.g. Barth et al., 2019; Elardo & Shearer, 2014; Faure et al., 2022; First & Hammer, 2016; Helz, 1987; Lynn et al., 2017), metamorphic (e.g. Beno et al., 2020; Clarke et al., 2020; Johnson et al., 1977; Turner, 1968), and hydrothermal rocks (e.g. Agrell et al., 1998; Gose et al., 2010). The solid solution between forsterite and fayalite is most useful to igneous petrologists, where Mg concentration in an olivine crystal can often be used to track the relative differentiation of a melt. Mg decreases as crystallization continues, and the temperature of the melt decreases. This is usually communicated using the term Fo#$= 100 * \frac{Mg_{ol}(at\%)}{Mg_{ol}(at\%)+Fe_{ol}^{2+}(at\%)}$. It is expected, in a "normally zoned" olivine crystal, that Fo# decreases from the core of the crystal to the rim (Dana & Ford, 1932; Deer et al., 1966), recording evolution in temperature and composition of the surrounding melt.

Importantly, olivine is the first phase to crystallize out of a variety of primitive melts, making it the first solid record of many rock formation histories (Basaltic Volcanism Study project, 1981; Bowen, 1956; Deer et al., 1966; Dodd, 1981; Helz, 1987; McSween, 1999; Rapp & Draper, 2018). An understanding of the cooling history of olivine can, therefore, reveal detail about the formation histories of a variety of rocks.

1.2 Electron Probe Microanalysis

All of the research in this thesis involves the technique of Electron Probe Microanalysis (EPMA). This technique provides non-destructive quantitative or qualitative chemical abundances of a material. Measurements are made using characteristic X-ray emission, stimulated by the bombardment of electrons on a material of interest (Barkla & Sadler, 1909; Kaye, 1909). These characteristic X-rays are then collected by a wavelength dispersive spectrometer (WDS), which uses crystal diffraction of X-rays to analyze only the X-rays of interest (Hillier & Ramberg, 1947; Reed, 1993). Data can either be reported in raw X-ray counts (qualitative analysis, typically in the form of x-ray intensity maps), or the data can be converted to wt% or at% of each element (quantitative analysis). Quantitative analysis uses a standard with known concentrations of an element and 'matrix corrections', which correct for the many factors that affect the relationship between intensity and concentration. These factors can include diverse elements present, represented by the element's atomic number (Z), absorption within the sample (A), and fluorescence (F) (Reed, 1993). Throughout this thesis, ZAF matrix corrections are completed using the calculations of Armstrong/Love Scott (Armstrong, 1988) applied using the Probe for EPMA (PFE) software.

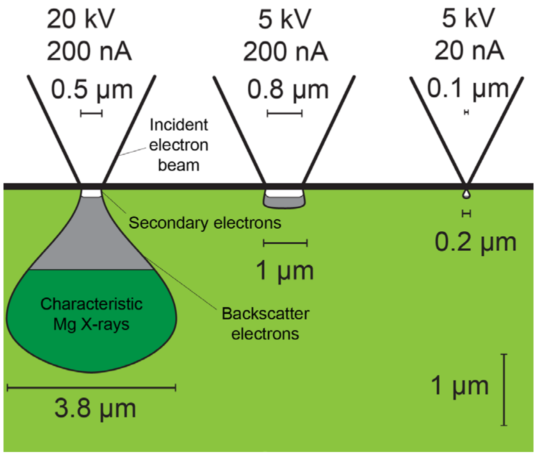

Figure 1.2: Probe beam diameter and interaction volume as a function of accelerating voltage and beam current. Beam diameters from Kimura et al. (2006). Volumes from Casino simulations for characteristic Mg X-rays in Forsterite with a carbon coating. Image is vertically stretched. Scale bars beneath interaction volume indicate the effective area a focused beam would probe with the given analytical conditions.

During any quantitative analysis, standards are frequently reanalyzed to gauge how accurate the analyses should be and ensure that there is no drift in analyses. These are called "check standards" and are carefully selected to approximate the material being analyzed as closely as possible. The standard deviation of these analyses is the primary contributor to the error term in EPMA, and ±1 to 2 σ of this analysis is frequently reported directly as the error in analysis (Bell et al., 2021; Lynn et al., 2020; McCarthy et al., 2020; Welsch et al., 2013, 2014).

The microprobe's electron beam has two primary controls: the beam current and the accelerating voltage. The beam current controls the total flux of electrons. A higher beam current will cause more interactions between electrons and atoms within the sample, increasing the signal. Meanwhile, the accelerating voltage controls the potential energy of electrons being emitted from the field emission gun. The higher the energy of bombarding electrons, the higher energy electrons can be ejected from the analyzed material. This means that higher accelerating voltage allows for analysis of higher atomic number elements since they have higher electron bonding energies. Higher accelerating voltage also leads to significant increases in interaction volumes. Simulations using the Monte-Carlo simulation software "Casino" show that an increase from 5 to 20 kV increases penetration depth by 1.7 μm and interaction radius by 2.8 μm (Illustrated in Figure 1.2).

In chapters 3, 4, and 5 of this dissertation, trace elements needed to be mapped with high spatial resolution, beyond the typical resolution produced by EPMA. To obtain this data, we leverage the relationship illustrated in Figure 1.2. Reducing the accelerating voltage of incident electrons reduces the interaction volume. However, at 5 kV, the dominant restriction to good spatial resolution becomes the size of the focused beam itself. Beam size can be reduced by decreasing the current (Kimura et al., 2006). This trades intensity per second for spatial resolution. Extremely long dwell times for a map (>1 second/pixel) are used to collect these maps, allowing for both high spatial resolution of trace elements. Note that this technique only works with elements that have an atomic number beneath 20, as 5 kV electrons do not have sufficient energy to produce enough X-rays in elements with high atomic numbers.

1.3 Diffusion Chronometry

Most minerals can have a variety of compositions depending on what elements are available and what conditions exist during crystallization. Variations in the chemical compositions of minerals as they crystalize create chemical gradients. The diffusion of elements within the crystal lattice relaxes these gradients over time in a predictable manner. This process can be modeled through the application of the diffusion equation.

1.3.1 The Diffusion Equation

The diffusion equation (also called Fick's second law) is a second order partial differential equation proposed by Adolf Fick (Fick, 1855). When applied to diffusing concentrations, it takes the form of Equation 1.1.

$$\text{a)}\ \frac{\partial C}{\partial t} = D\frac{\partial^2 C}{\partial x^2}$$

$$\text{b)}\ \frac{\partial C}{\partial t} = D\Delta C$$

Equation 1.1: Fick's second law for diffusion, assuming D is not a function of x. a) 1D diffusion equation. Here C(x, t) represents the concentration for each point $-\infty < x < \infty$, $0 \leq t < \infty$ is time, and D is the diffusivity (see Chapter 3). b) n-Dimensional diffusion equation. Here $C(x_1, \ldots, x_n, t)$ represents the concentration for each point $(x_1,\ldots,x_n) \in \mathbb{R}^n$, and Δ is the Lambertian operator ($\Delta x = \text{div}(\nabla x)$). Typically, $n \leq 3$.

Equation 1.1 can be solved by applying the invariance properties of the diffusion equation and solving for a special case of this equation. We define a diffusion equation Q, where Q(x,0) = 1 for x > 0 and Q(x,0) = 0 for x < 0. The solution of this can be transformed to create countless other equations that solve Equation 1.1. This is because one of the invariance properties is that "An integral of solutions is again a solution" (Strauss, 2008). Thus, we can transform this 0-centered equation to an arbitrary starting condition, φ(y)=C(y, 0). In this case, $C = \int_{-\infty}^{\infty} \frac{\partial Q(x-y,t)}{\partial x} \phi(y)\, dy$, which must be a solution to Equation 1.1 by the invariance properties. Simplifying, this takes the form of Equation 1.2.

$$C(x,t) = \frac{1}{\sqrt{at}} \int_{-\infty}^{\infty} e^{-\frac{(x-y)^2}{bt}} \phi(y)\, dy$$

Equation 1.2: Analytical solution to the diffusion equation, a and b are constants.

However, one will note that the integral in Equation 1.2 is typically impossible to solve. In special cases, its similarity to the normal distribution from statistics can be used, and the error function: $Erf(x) = \frac{2}{\sqrt{\pi}} \int_0^x e^{-p^2} dp$ can force out analytical solutions from an otherwise impossible problem (Chakraborty, 2008; Costa et al., 2020; Strauss, 2008). Unfortunately, it is exceedingly rare for natural samples to possess the well-defined initial conditions that make an analytical solution of the diffusion problem possible.

1.3.2 Numerical modeling

Fortunately, analytical solutions are not the only approach to solving differential equations. Here, we aim to approximate derivatives to directly approximate solutions to Equation 1.1. Throughout this dissertation, we complete this through the finite difference method. This method approximates derivatives of an equation using one of three solutions. Forward finite differences (Equation 1.3 a), backwards finite differences (Equation 1.3 b), and central finite differences (Equation 1.3 c).

a) $\frac{\partial f(x)}{\partial x} \approx \frac{f(x+dx)-f(x)}{dx}$

b) $$\frac{\partial f(x)}{\partial x} \approx \frac{f(x)-f(x-dx)}{dx}$$

c) $$\frac{\partial f(x)}{\partial x} \approx \frac{f(x+1)-f(x-1)}{2dx}$$

Equation 1.3: finite differences in the forward (a), backward (b) and central (c) directions.

These three equations can be used in different combinations to address the diffusion equation in arbitrarily shaped systems. In the one-dimensional case, this is solved in Equation 1.4. This solution can then be iteratively solved to find C(x,t) for all t.

a) $$\frac{\partial C}{\partial t} = D\frac{\partial^2 C}{\partial x^2} \approx \frac{C(x,t+dt)-C(x,t)}{dt} = D\frac{\left(C(x+2dx,t)-2C(x,t)+C(x-2dx,t)\right)}{4dx^2}$$

b) $$dt \leq \frac{dx^2}{2D}$$

Equation 1.4: a) a numerical solution of Fick's second law using forward differences for the time derivative, and central differences for the spatial derivative. b) The stability criterion for dt.

Note that for all solutions, the stability criterion (Equation 1.4 b for 1D) must be obeyed. This ensures that there is no net increase in numerical error in each round of computation of this equation, and this question remains well posed (Strauss, 2008). If this is not obeyed, erratic results will spoil the model. Prior to all models, a user should find the maxima for D, and ensure dt is chosen such that the stability criterion is not violated.

To numerically model diffusion in a crystal, a user typically provides initial conditions, iteratively solves Equation 1.4 (or a similar numerical solution) until the model matches a measured concentration gradient. This is typically done by calculating the root mean squared deviation (RMSD) between the model and the dataset in each loop. The timestep with a minimum RMSD is then selected as the diffusive timescale.

1.4 Kröger-Vink notation

Kröger-Vink notation has become a common way to communicate behaviors inside a crystal lattice, particularly when dealing with point defects (Burgess & Cooper, 2013; Chakraborty, 2010; Connelly et al., 2005; Dohmen et al., 2010; Kingery et al., 1976). Kröger-Vink notation utilizes a combination of normal chemical symbols combined with subscripts that describe the site an element is in and a superscript that describes the charge of the site relative to neutral charge. Though typically, only normal elemental symbols are used, in the case of vacancies on a site, a “□” symbol is used. As for the superscript, an “x” means that the site has no charge defect, a “·” means the site has a +1 charge defect, and a “ʹ” means the site has a -1 charge defect (Connelly et al., 2005; Kröger, 1985; Kröger & Vink, 1956). This dissertation will only describe point defects in the olivine structure, so there are only four possible subscripts. An “O” means the element resides in the anionic site typically filled with O^{2-}. An “M” means the element is in the octahedral site typically occupied by Mg^{2+} or Fe^{2+}. A “T” means that the element resides in the tetrahedrally coordinated cation site, typically filled by Si^{4+}. Finally, “i” means that the element is interstitial in the crystal lattice.

For example, a pure fayalite (Fe_2SiO_4) is written as $2Fe_M^x + Si_T^x + 4O_O^x$. A common way to create point defects in the octahedral site of olivine is communicated with this notation by Nakamura & Schmalzried (1983, Eq. 1.x).

$$6Fe_M^x + SiO_2 + O_2(g) = 2\square_M'' + 4Fe_M^\bullet + Fe_2SiO_4$$

Equation 1.5: Nakamura & Schmalzried (1983) equation for octahedral site vacancy production in olivine.

Eq 1.5 represents the "equivalence" between 6 moles of Fe^{2+} ions in the M site, a mole SiO_2, and a mole of O_2 gas and 2 moles of vacancies on the M site, 4 moles of Fe^{3+} ions on the M site, and a mole of fayalite. Note, as (Chakraborty, 2010) points out, "equivalence" here means that a reaction can take place without violating charge, site, and mass balance.

1.5 Outline of this Dissertation

Here we demonstrate the use and behaviors of chemical heterogeneities in olivine. In Chapter 2 we explore the use of diffusion modeling to constrain formation times of a sample from the Apollo 17 mission. As a byproduct, we find a possible issue with how phosphorus records diffusion timescales. So, in Chapter 3, we investigate the diffusive behavior of this element in detail. In Chapter 4, the behavior of phosphorus in olivine at the nanoscale is investigated. In Chapter 5, we then apply diffusion chronometry onto a series of type I PO and BO chondrules, to demonstrate how diffusion chronometry can be applied in olivine without the pitfalls discussed in Chapters 3 and 4. Finally, at the end of this dissertation, we will summarize how diffusion chronometry can best be applied in olivine, and what research we intend to do next.

Chapter 2: Diffusion Chronometry on Apollo Sample 76535

As published in: Nelson W.S., Hammer J.E., Shea T., Hellebrand E., and Taylor J.G. (2021). *Chemical heterogeneities reveal early rapid cooling of Apollo Troctolite 76535*. Nature Communications **12**, 7054

2.1 Abstract

The evolution of the lunar interior is constrained by samples of the magnesian-suite of rocks returned by the Apollo missions. Reconciling the paradoxical geochemical features of this suite constitutes a feasibility test of lunar differentiation models. Here we present the results of a microanalytical examination of the archetypal specimen, troctolite 76535, previously thought to have cooled slowly from a large magma body. We report a degree of intra-crystalline compositional heterogeneity (phosphorus in olivine and sodium in plagioclase) fundamentally inconsistent with prolonged residence at high temperature. Diffusion chronometry shows these heterogeneities could not have survived magmatic temperatures for >20.1 My, i.e., far less than the previous estimated cooling duration of >100 My. Quantitative modeling provides a constraint on the thermal history of the lower lunar crust, and the textural evidence of dissolution and reprecipitation in olivine grains supports reactive melt infiltration as the mechanism by which the magnesian suite formed.

2.2 Introduction

Lunar evolution has been defined by the samples returned by the Apollo missions, culminating in the generally accepted Lunar Magma Ocean (LMO) model. This model postulates that the Moon was once largely molten, and the lithologies now present on the Moon are produced from geochemical reservoirs defined by crystallization products of this melt. However, the magnesian suite (Mg-suite) was found to possess characteristics that prompted amendments to the basic LMO model. This suite contains the combination of some of the most anorthitic plagioclase (An_{98-84}) and the most Mg rich mafic silicates (Mg# 95-60) ever found in lunar samples (Shearer et al., 2015), suggesting crystallization from a parent melt that is highly primitive (unmodified by fractional crystallization). However, these rocks are also enriched in potassium, rare earth elements, and phosphorus (KREEP; Shearer et al., 2015), which indicate a highly evolved (influenced by fractional crystallization) parent melt. Any plausible model of lunar magmatic evolution must explain these paradoxical chemical features.

Various hypotheses for Mg-suite petrogenesis have been proposed (c.f., Shearer et al. 2015). Early studies postulated its direct formation during crystallization of the LMO (McCallum, 1983; Raedeke & McCallum, 1980; Wood, 1975). The resulting models succeeded in generating primitive mineral compositions but required late-stage metasomatism to introduce the KREEP signature. Alternatively, Longhi (1981) suggested the Mg-suite was formed by high-pressure partial melting of a bulk-Moon source composition, followed by assimilation of anorthite and a highly evolved melt. Prissel and Gross (Prissel & Gross, 2020) modified this theory, eliminating the requirement of anorthite crust assimilation, and demonstrating that partial melting at high pressure after cumulate overturn could produce a suitable Mg-suite parent melt. This liquid could then have been extracted from its source, as has been proposed for the younger picritic glasses (Delano, 1986). Warren and Wasson (1979) postulated the existence of a layer of late-stage fluids called "ur-KREEP", which could have been intersected by the Mg-suite parent melts, with the two melts mixing and imparting a KREEP signature to the Mg-suite parent (Hess et al., 1978; Papike et al., 1996). Ringwood and Kesson (Ringwood et al., 1976) suggested that overturn of magma ocean cumulates brought solid Mg-rich cumulates near the lunar surface. Elardo et al. (2011, 2020) demonstrated that mixing these cumulates with ur-KREEP would lower the liquidus of the system, and radiogenic heat from the decay of potassium and thorium would have also helped produce the Mg-suite parent melt. Another possibility is that cooling and crystallization of an impact melt sheet generated during an impact event (Hess, 1994; Norman et al., 2016) caused direct mixing of anorthite-rich crust, ur-KREEP, and mantle material. The variety of mechanisms still being debated after 45 years demonstrates the need for additional constraints on the controlling variables of Mg suite formation: the timing and process of melt production, the style and geometry of magma emplacement, and the thermal evolution of the lower crust. Chemical zoning within mineral grains can be leveraged to determine the maximum length of time the grains could have remained at magmatic temperatures without being compositionally homogenized by element diffusion (Costa et al., 2003). This study constrains the highest temperature portion of the Mg-suite cooling path by evaluating chemical heterogeneities imparted in olivine and plagioclase crystals in troctolite 76535 during their growth from a silicate liquid.

Apollo 17 astronauts collected troctolite 76535 at geology station six (Butler, 1973). It is a coarse-grained phaneritic rock composed of plagioclase (60%), olivine (35%), and orthopyroxene (5%) (Dymek et al., 1975). This sample is the most pristine (displaying the least evidence for impact modification) in the Mg-suite, and thus has become one of the most scientifically valuable samples of the Moon (Shearer et al., 2015). Notably, 76535 has been used to quantify the amount of water in the primitive Moon (Barnes et al., 2014), the evolution and cessation of the lunar magnetic dynamo (Garrick-Bethell et al., 2009), and the effect of shock on radiometric ages (Edmunson & Cohen, 2009).

Our current understanding of this sample's cooling history presents a paradox. Radiometric, petrographic, and petrologic studies of the sample indicate slow subsolidus cooling rates and long cooling times. Age determinations from independent isotopic systems suggest subsolidus cooling rates around 3.9 degrees per million years

(Borg et al., 2017). However, radiogenic age determinations are not suitable for determining the higher temperature (magmatic) cooling history of this sample. If the cooling path defined by a three-point line connecting paired radiometric closure temperatures and ages (Borg et al., 2017) is extrapolated to higher temperatures, the sample would have begun crystallizing around 4,421±11 Ma, before the estimated 4,383±17 Ma formation of sample 60025, the best-constrained member of the ferroan anorthosite suite (FAS) (Borg et al., 2011, 2017). As the FAS is postulated to represent the flotation anorthosite crust, this line of reasoning poses a conundrum: The Mg-suite would have begun crystallizing before formation of the crust into which it was emplaced (Borg et al., 2017).

In this study of troctolite 76535, we present new evidence of subtle chemical heterogeneities in plagioclase and olivine crystals, which we interpret to represent arrested diffusive homogenization. Applying the technique of diffusion chronometry, we conduct extensive numerical modelling to find the maximum amount of time this sample remained above the closure temperature for Na-Ca interdiffusion in plagioclase and P diffusion in olivine. Our results constrain the thermal history of this sample to <~20 Ma. By extension to the entire suite, these results challenge the notion that the Mg-suite lithologies represent layers of large, slowly cooled igneous intrusions. Rather, the faster magmatic cooling duration, along with new evidence of crystal dissolution and reprecipitation, suggest the Mg-suite formed by a process involving reactive melt infiltration.

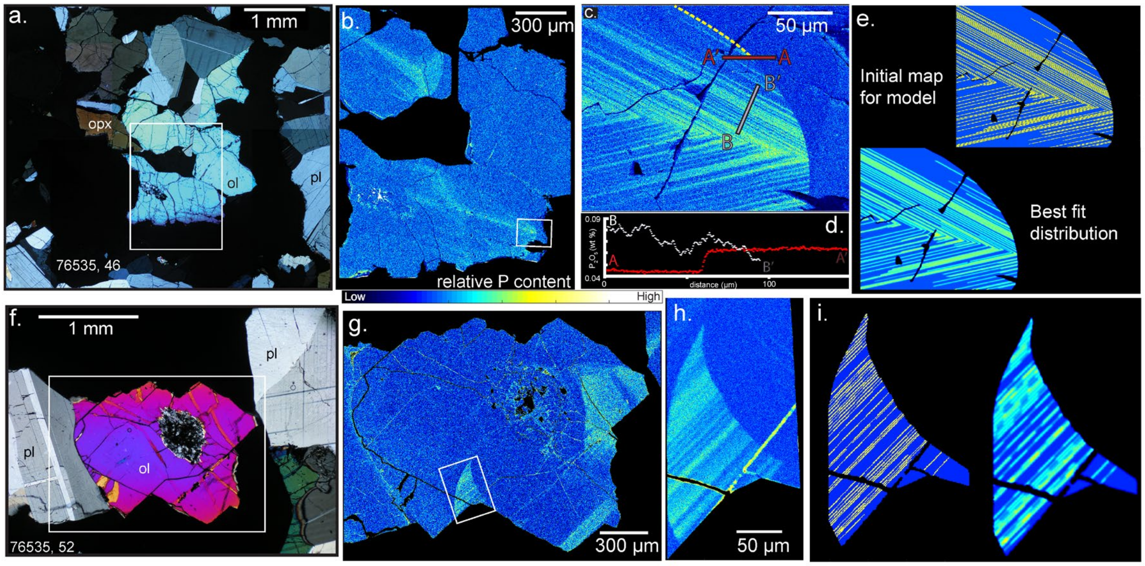

Figure 2.1: Cross-polarized light (XPL) images (**a**, **f**), P kα intensity maps (**b**, **c**, **g**, **h**), profiles (**d**) (red: averaged along truncation surface, white: along line), and diffusion models' initial conditions and final results (**e**, **i**).

2.3 Results

2.3.1 Chemical heterogeneities in 76535. Previous petrologic studies of 76535 report chemical homogeneity of its major phases (Gooley et al., 1974; Shearer et al., 2015), a finding that has gone unchallenged since the 1970s, likely because it is consistent with the sample's extensively annealed texture. Intragrain compositional variations can now be detected at much finer spectral and spatial resolution. Electron probe microanalysis (EPMA) X-ray mapping and profiling on slides of 76535 reveal compositional heterogeneities (Figure 2.1, 2.2) in every crystal that we mapped. Concentric sodium

(Na) zoning in plagioclase is very subtle (given the range in Na) but resolvable. Phosphorus (P) heterogeneities in olivine are lamellar and sharp, similar in appearance to those in terrestrial samples (de Maisonneuve et al., 2016; Milman-Barris et al., 2008; Shea et al., 2015; Welsch et al., 2014), as well as lunar basalts (Elardo & Shearer, 2014) and soils (Demidova et al., 2018). The existence of these heterogeneities implies rapid initial olivine growth (Welsch et al., 2014), which is most readily induced by relatively rapid cooling at magmatic temperatures (Shea et al., 2019), and preservation of initial growth zoning down to the closure temperature of P diffusion.

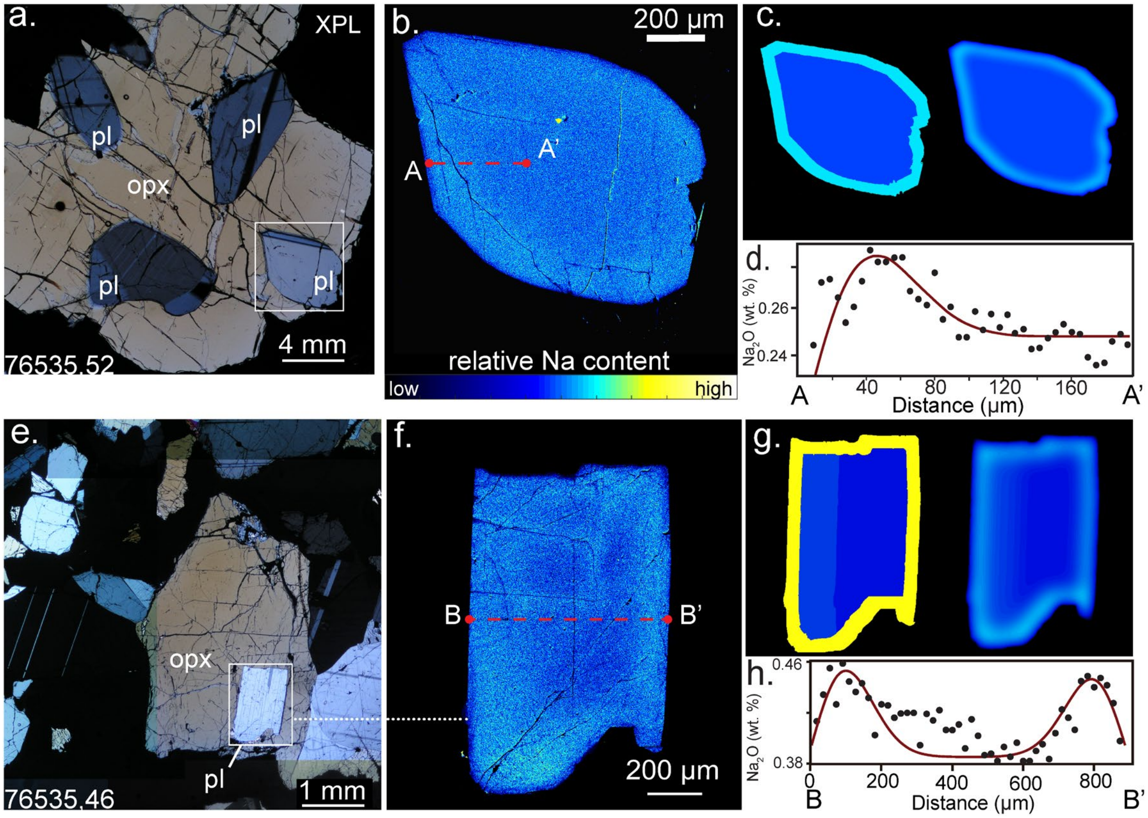

Figure 2.2: XPL context (**a**, **e**), Na kα X-ray intensity maps (**b**, **f**), profiles (black dots, **d**, **h**), and initial/final diffusion models (**c**, **g** and red lines in **d**, **h**).

All olivine crystals we analyzed possess regions of P-enriched lamellae alternating with relatively P-poor zones, and regions that are homogeneous and P-poor throughout (Figure 2.1). There are no differences in the concentrations of Ca, Fe, Mg, Al, Cr (Figure A-6), or crystallographic orientation (Figure A-8) between the two regions. The boundaries between the two types of regions are sharp and cuspate, a cross-cutting relationship that indicates dissolution of the P-enriched olivine and precipitation (i.e., overgrowth) of P-poor olivine. In detail, the gradient across the dissolution front is significantly sharper than across the P-rich lamellar heterogeneities. If the lamellae were sharper when the P-enrichments formed (Shea et al., 2015; Welsch et al., 2014), the steeper concentration gradient across the cuspate boundaries suggests that dissolution occurred after most of the diffusive relaxation in the P enriched regions had occurred.

2.3.2 Diffusion modeling. Diffusion chronometry resolves timescales necessary to relax compositional heterogeneities diffusively by forward modeling of Fick's second law (Figure 2.3), given appropriate laboratory-determined values for cation diffusivities (D_P^{ol} (Watson et al., 2015) and $D_{Ca\text{-}Na}^{plag}$ (Grove et al., 1984)). The cooling path is the dominant variable in determining total diffusion timescales and need to be chosen carefully. To complete any diffusion modeling, we must assume an initial temperature and cooling path to obtain the total time scale over which diffusion occurred. A temperature of 1297 °C was used for olivine (liquidus temperature), and of 1229 °C for plagioclase (appropriate for the most sodic portion of the rim). Using these initial temperatures, a 3.9 °C/Myr linear cooling path (Borg et al., 2017) results in complete homogenization of Na in plagioclase before the system cools by 0.2 °C. Phosphorus in olivine homogenizes by 1296 °C. Even if P diffusivity approaches that of slow diffusing, similarly coordinated elements (Boesenberg & Hewins, 2010) like Si (Dohmen, 2002), ~5 orders of magnitude lower than the published D_p^{ol}, (Watson et al., 2015) complete chemical homogenization of P is still attained by 1241 °C. Regardless of the diffusivity value chosen, the temperatures at which grains achieve chemical homogeneity are well above the diffusive closure temperature of Ca-Na in plagioclase and P in olivine. Therefore, it is necessary to consider faster, nonlinear cooling to explain the preservation of chemical zoning.

We sought the maximum survival time of these heterogeneities by iteratively

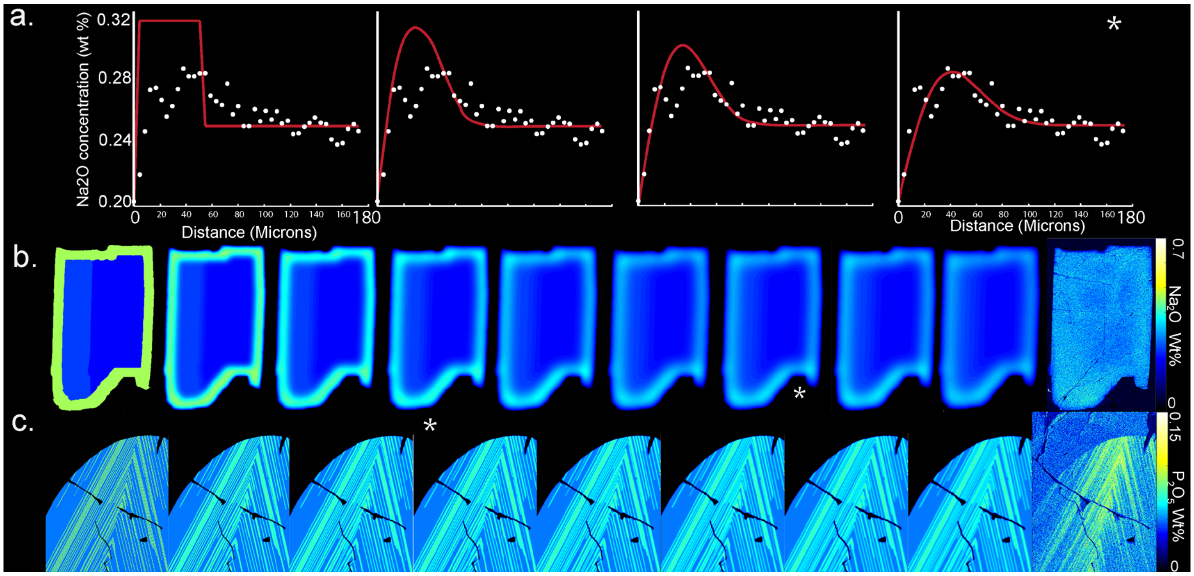

Figure 2.3: **a** 1D on plagioclase in slide, 52 (Fig. 2.2b). **b** 2D on plagioclase in slide, 46. **c** 2D on olivine in slide, 46. Asterisk represents minimum RMSD.

testing various functions and fit coefficients over many millions of runs to impose non-linear cooling paths. The boundary conditions are detailed in the methods section; in summary, all cooling paths are set up to end between 800-900^{o}C where they connect with the linear cooling rate proposed by Borg et al. (2017).

If phosphorus diffusion coefficients for olivine are calculated using the existing expressions (Watson et al., 2015), the timescales are extremely short (Table 2.1), 6 orders of magnitude shorter than indicated by Na-Ca interdiffusion in the neighboring plagioclase crystals. However, petrography indicates co-crystallization, such that each crystal in the rock provides an independent expression of the same cooling history. Seeking to remedy this inconsistency, we substituted D_{Si}^{ol} for D_{P}^{ol} in most olivine diffusion models. Like Si, P is a high-valence cation occupying tetrahedral sites in the olivine lattice (Boesenberg & Hewins, 2010; Buseck & Clark, 1984; Shea et al., 2019). The maximum cooling times allowable by the diffusion models are 20 and 27 My for plagioclase and olivine respectively. These cooling timescales are an order of magnitude shorter than previous estimates (Borg et al., 2017; Gooley et al., 1974; McCallum et al., 2006; Stewart, 1975) (all above 100 My). Note that subsequent reheating events are included in this estimate. Thus, should reheating take place, initial magmatic cooling timescales would have to be even shorter than our estimates in order to preserve these heterogeneities.

	Plagioclase ,46	Plagioclase ,52	Olivine , 46		Olivine , 52	
			D_P	D_{Si}	D_P	D_{Si}
Diffusion Time (My)	22.0	20.1	$1.2*10^{-5}$	27.1	$9.5*10^{-6}$	27.1

Table 2.1: Maximum calculated survival timescales for the observed compositional heterogeneities. Slide numbers are given to represent the crystals described in Figure A-5, with plagioclase , 52 referring to crystal Pl52_1

Though these results contradict previous estimates for the early cooling history of troctolite 76535, they do not invalidate past measurements of the cooling rates in this sample. Magmatic cooling histories have previously been reconstructed from the lower-temperature portion of the overall cooling history (Borg et al., 2017; Gooley et al., 1974; Stewart, 1975). Therefore, the cooling rates reported by each of these studies form a coherent but nonlinear single cooling path. Our results pertain to the highest temperature portion of this path (Figure 2.4).

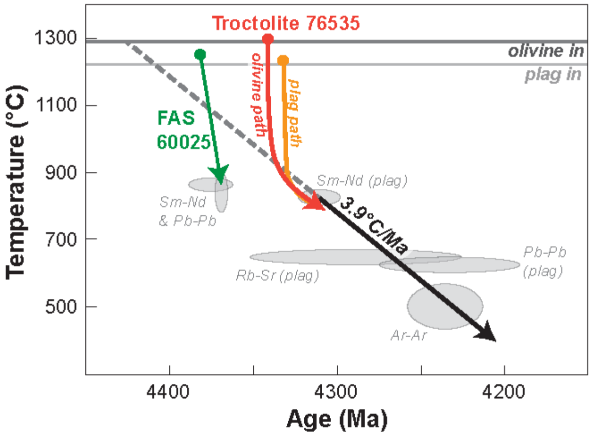

Figure 2.4: Neither solution conflicts with the formation of FAS 60025 (green line). FAS liquidus from Rapp and Draper (2018) and cooling path from Mcallum and O'Brien (2018). After Borg et al. (2017).

2.4 Discussion

2.4.1 Implications for the petrogenesis of troctolite 76535. The discovery of sharp compositional gradients in the form of P-rich lamellae in olivine from 76535 (Figure 2.1) imposes important new qualitative constraints in addition to the quantitative maximum cooling timescales. A comparison with a terrestrial troctolite in slow-spreading oceanic crust at the Atlantis Massif (Hellebrand et al., 2013; Welsch et al., 2014) (previously mischaracterized as a gabbro (Welsch et al., 2014)) illustrates these constraints. Like the olivine in 76535, high-Fo olivine grains in these terrestrial lower crustal rocks contain P-enrichments (Hellebrand et al., 2013; Welsch et al., 2014) . The P-rich lamellae in lunar troctolite 76535 (Figure 2.1) are much sharper than those preserved within the Atlantis olivine grains (Figure A-4), suggesting more rapid overall cooling for 76535. The average magma cooling rate estimated using the massif assembly duration (0.2-2 My (Grimes et al., 2008; Pariso et al., 1996)) is 600-6000 °C/Ma, which in itself is rapid due to the tectonic exhumation of this lower crustal section along a long-lived normal fault. Thus, the petrographic comparison indicates that 76535 cooled through diffusion-active temperatures ≥2 orders of magnitude faster than previously suggested for 76535 (1-50 °C /Ma; Borg et al., 2017; Gooley et al., 1974; McCallum et al., 2006). Having established rapid initial cooling of the magma from which 76535 parent magma crystallized, we review prior observations and suggest a new conceptual model for the origin of the Mg-suite.

Mineral texture such as euhedral external morphology, concentric plagioclase compositional zoning, and poikilitic intergrowths require crystallization to have occurred initially from a liquid. The preservation of steep concentration gradients of phosphorus in olivine, and resolvable Ca-Na zoning in plagioclase, require relatively rapid cooling through magmatic temperatures. Relatively sharp, fine-scale lamellae of P in olivine further reveal that initial crystal growth was rapid (Milman-Barris et al., 2008; Shea et al., 2019; Welsch et al., 2014). Yet the presence of regions lacking P enrichments (Figure 2.1) outside cuspate dissolution surfaces imply that olivine precipitation resumed at a relatively low growth rate. These new observations must be reconciled with indicators of a slow subsolidus (and thus below diffusion closure temperature) cooling rate: triple junctions at plagioclase grain boundaries and a three-point cooling rate line formed by radiometric ages (Borg et al., 2017).

Terrestrial troctolites are interpreted to have formed primarily by either accumulation of mineral grains within a magma body, or partial replacement of rock via reactive melt infiltration (Suhr, Hellebrand, et al., 2008). We consider these geneses in view of the thermal constraints mandated by 76535. The first scenario requires the existence of a magma body with a high volumetric proportion of liquid relative to solid phases. Recent experimental and numerical treatments have rekindled and refined two long-standing models for the formation of a liquid-dominated body in the lunar interior. Melting may have occurred at the boundary between overturned mantle cumulates and FAS crust units in the vicinity of (and possibly augmented by) a liquidus-lowering ur-KREEP component (Elardo et al., 2011, 2020). Alternatively, liquid may have accumulated as the result of decompression-driven partial melting associated with the overturn itself, and not require a hybrid source (Prissel & Gross, 2020). A third possibility is that the liquid-rich magma body formed via impact (Hess, 1994; Norman et al., 2016). In all of these cases, formation of troctolite occurs as the liquid lens progressively crystallizes to form a layered sequence of lithologies (c.f. the lower units of the Kiglapait or Skaergaard intrusions (McBirney & Noyes, 1979; Morse, 2015)). Our results inform the discussion of Mg-suite petrogenesis chiefly through considering the implications for the thermal history. Importantly, a liquid-rich magma body capable of generating layered cumulate lithologies is likely to be spatially compact and coherent over length scales of 100's of m to 10's of km. The maximum size of a spherical magma body consistent with the modeled magmatic thermal histories has a radius of 11km (Methods (2.5), Figure A-8). A more realistic lenticular magma body could be of higher volume and still satisfy the initial rapid cooling criterion but would then cool too quickly (internally) to satisfy the subsolidus slow-cooling criterion.

A second scenario is that the troctolites form via reactive melt infiltration, (Figure 2.5). This model differs from those above in that the system is solid-dominated rather than liquid-dominated. Within the context of this solid-dominated system, our results make it possible to consider, in greater detail, the physical picture of troctolite generation from the hybrid source (Elardo et al., 2011, 2020). Hybridization requires that the crust behaves as a plastic solid upon interacting with rising lower mantle material. Mafic cumulates could mechanically mix with the lower crust, permitting the two lithologies to mingle chaotically and creating intimate mixtures characterized by high inter-lithologic contact area over small (cm to m) length scales. Cotectic melting would thus occur over a widely distributed volume comprising the former lower crust and upper mantle, but melt would accumulate locally to form plexuses of melt-rich lenses that promote reactive melt infiltration (Drouin et al., 2009; Renna et al., 2018; Renna & Tribuzio, 2011; Suhr, Hellebrand, et al., 2008). The hybrid (LMO olivine and FAS anorthite) would then partially melt and interact with ur-KREEP, forming a reactive liquid saturated in forsteritic olivine (Yang et al., 2019) as well as anorthite. Unsteady melt production and pulsatory porous flow during the interaction of the mingled parent lithologies could produce the cycles of local olivine and plagioclase dissolution-reprecipitation that are required by the new observations we present.

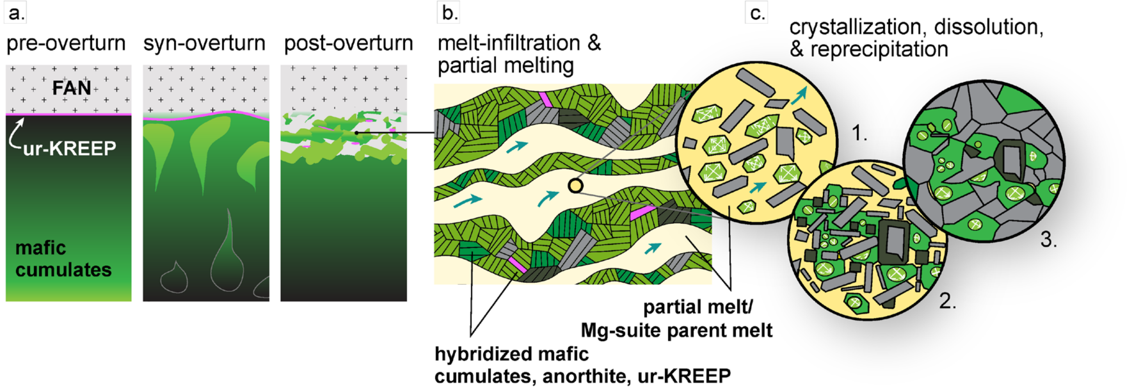

Figure 2.5: **a** Mg-rich lower mantle interacts with a warm anorthitic crust, and ur-KREEP, mechanically mixing the three components. **b** Partial melting occurs; the liquid infiltrates the surrounding rock and accumulates in lenses (cm–m scale). **c** Microscopic views of rapid initial crystallization followed by dissolution and crystallization of plagioclase (gray), olivine (green), and orthopyroxene (dark green) during rapid cooling. As the magma temperature approaches the temperature of the surroundings, the cooling rate slows. Grains anneal during protracted subsolidus cooling.

As with Atlantis Massif units, this sequence of events could be expected to produce all lithologies found in the Mg-suite (Suhr, Johnson, et al., 2008). In the chaotic mixing of cumulates, mixtures ranging between pure mafic cumulates and pure crustal material would be created. Melts in these different zones would have a range of compositions, and crystallize different products, potentially producing several Mg-suite lithologies. In addition, reactive melt that interacts with the surrounding crust could create the pink spinel anorthosites (Prissel et al., 2014). The KREEP-poor members of the Mg-suite-like meteorites (Gross et al., 2020) could also be explained in this scenario; should ur-KREEP have not been evenly distributed beneath the lunar crust (Elardo et al., 2020; Shearer et al., 2015) , the reactive infiltration process would create KREEP-poor Mg-suite samples as posited for regions outside of the PKT.

The conceptual description above presumes the Mg-suite parent is a hybridized source. Formation of the Mg-suite parent liquids by decompression melting of mafic cumulates (Prissel & Gross, 2020) is also compatible with the reactive melt infiltration process, as demonstrated by the existence of olivine-rich troctolites of the Atlantic Massif that owe their existence to iterative reaction between partial melts of Earth's mantle and lithospheric peridotite. In fact, formation of the suite of the lunar Mg-suite lithologies by progressive reaction of mantle-derived liquids with just-formed lithologies may pose fewer challenges than the hybrid-source model, as it requires involvement (physical juxtaposition) of fewer physically distinct sources.

We suggest that the preferred scenario involving reactive melt infiltration presents two advantages over cumulate layering. First, in the context of the hybrid-source model, the fine (cm) length-scale interaction among FAS and lower mantle crystals would promote cotectic melting, which is energetically favorable because interphase grain boundaries melt at much lower temperatures than pure end members (O'Driscoll et al., 2010); the exorbitant heat budget required to melt FAS is a long-standing problem in Mg-suite genesis (O'Sullivan & Neal, 2013). Second, and relevant to both source-melt models, reactive infiltration provides a compelling explanation for the observed textures. The olivine P-enrichment patterns in 76535 require rapid crystal growth, dissolution, and lastly slow re-growth, a cycle that is more compatible with solid-dominated than liquid-dominated systematics.

Powerful constraints of Mg-suite petrogenesis have been provided by a detailed analysis of troctolite 76535. However, to truly test these findings similar analysis must be completed on more samples from the Mg-suite in the Apollo collection, and magnesian suite like meteorite clasts (especially a comparison of KREEP rich and KREEP poor clasts, exploring the thermal histories of these two suites, which would give insight into the role of KREEP signatures in the petrogenesis of the Mg-suite). Of special interest to the question of petrogenesis is an analysis of the different major olivine and plagioclase bearing rock types of the Mg-suite, such as dunites (prime candidates: 72415-72418), spinel troctolites (prime candidate: 67435), norites (15360), and perhaps gabbronorites (should any suitable grains be found). The data from such studies could provide significant new constraints on Mg-suite petrogenesis and the evolution of the lunar crust. Given the recent discovery that many samples of the Mg-suite formed nearly contemporaneously (Borg et al., 2020), it may be possible to obtain a cooling history for the rest of the suite as well.

Resolving the timing of important events in the Moon's history is at the frontier of lunar science. The Moon-forming giant impact (GI) is suggested to have occurred "early and old" relative to the formation of the solar system (Yin et al., 2014), or "late and young"(Borg et al., 2011). Combined U-Pb and Lu-Hf isotopic systematics of lunar zircon crystals are only consistent with the older GI ages and they suggest that the LMO solidifed rapidly(Barboni et al., 2017). These old zircon ages contrast with the slower time frame of LMO solidification(Maurice et al., 2020) proposed to resolve the paradox posed by coincident model ages for the FAN and Mg-suite (Borg et al., 2011), as well as the considerably younger Sm-Nd model ages obtained for the Mg-suite samples (Borg et al., 2017). Our data set is not capable of critically evaluating the GI ages or the duration of LMO overturn. However, our observations do refute the suggestion that the young Mg-suite Sm-Nd ages are an artefact of very slow cooling from the magmatic liquidus through the low closure temperature of the Sm-Nd system(Barboni et al., 2017). Our results support rapid cooling through the Sm-Nd closure temperature in 76535 and by extension, contiguity of the model Sm-Nd ages with magmatic ages for the Mg-suite.

Preservation of sharp P-rich lamellae impose thermal constraints for future dynamic modeling. If the troctolite parent liquid crystallizes in an area dominated by hot lower-mantle, then it would cool too slowly at subsolidus temperatures for relatively sharp P-lamellae retention. Hence, 76535 poses a goldilocks scenario. The proportions of the dominant thermal masses (hot lower-mantle cumulates and warm anorthite) and the intimacy of their mixing in the melt source region, must have been just right.

2.5 Methods

2.5.1 Grain Selection

2.5.1.1 Plagioclase

Na-Ca interdiffusion in plagioclase may be modeled in grains that: a) preserved igneous growth facets, b) were isolated from phases that possess or accept Na, c) possessed minimal cataclastic features such as cracks and brecciation. One grain lacking requirements b and c was mapped and found to be homogeneous with respect to sodium, suggesting grain contact limited preservation of heterogeneities (Figure A-2). Thus, we regard all conditions (a-c) as requirements for application of the numerical diffusion chronometry technique.

Despite the large proportion of plagioclase in this sample, very few grains match all three criteria. We inspected six slides of troctolite 76535 that contained hundreds of plagioclase grains. Of these grains, four were suitable for diffusion chronometry. All four grains are surrounded by either olivine or orthopyroxene, preserving igneous growth facets.

2.5.1.2 Olivine

The skeletal structure of phosphorus enrichment patterns in olivine removes the growth facets condition as well as the isolation condition. The high pristinity of this sample ensures that virtually any grain containing P heterogeneities is suitable for modeling. From the crystals we mapped at low magnification, we selected two nested areas for high-resolution mapping to be used for diffusion modeling.

2.5.2 Analytical Methods

Quantitative profiles and qualitative X-ray intensity maps were acquired using the University of Hawai'i at Mānoa's JEOL JXA-8500F field emission electron microprobe.

2.5.2.1 Olivine

Olivine profiles in Mg, Fe, Si and P were collected using a 15 kV accelerating voltage, a 200 nA beam current, 1-μm beam size, and 90s on peak time. The background was modeled using an exponential fit using Probe for EPMA v.12.7.2 (PfE). Phosphorus was measured on two spectrometers using the "aggregate intensities" function on PfE to increase analytical precision. Following precedent for the study of phosphorus in olivine(Grant & Kohn, 2013; Milman-Barris et al., 2008), an apatite standard (USNM 104021) was used for phosphorus, San Carlos USNM 111312/444 and Springwater USNM 2566) with concentrations of phosphorus known to be below the detection limit of our instrument were used as blanks, corrected by PfE. These two olivine standards are also used for Fe, Mg, and Si calibration. An A-99 Basaltic glass standard, and

Springwater USNM 2566 were analyzed as unknowns to track drift and accuracy (Table A-2). No drift correction was necessary, and standard analysis remained accurate throughout measurement.

Olivine maps were collected with a 15 kV accelerating voltage, a 200 nA beam current, a 100 ms dwell time, a step size between points of half a μm for high resolution maps used for modeling, up to 3.5 μm for overview maps, a focused beam was used. All 5 spectrometers were set to measure phosphorus.

2.5.2.2 Plagioclase

Analytical profiles of Na, Si, Ca, Fe, Mg and K in plagioclase were collected with a 15 kV accelerating voltage, beam currents of 40-100 nA, and a beam diameter of 4 μm. On peak times of 60 seconds were used for all modeled profiles.

Compositional maps were produced under similar conditions, though conditions varied by grain. The plagioclase grain in slide 46 is greater in size, permitting a larger beam diameter. For this grain, the following conditions were used for mapping: 15 kV accelerating voltage, 200 nA probe current, a 3-μm beam diameter, a 90 ms dwell time, and a 1.40-μm step size. The rest of the maps were collected over a smaller region, necessitating different conditions: 15 kV accelerating voltage, 125 nA probe current, focused probe diameter, a 90 ms dwell time, and a 0.60-μm step size. An anorthite standard (NMNH 137041) was analyzed as an unknown to track drift and accuracy (Table A-3). No drift correction was necessary for Na in either slide used for modeling.

2.5.3 Diffusion Modeling

The presence of compositional heterogeneities in these samples can be leveraged to quantify maximum allowable timescales of diffusion during cooling. In order to model diffusive relaxation, boundary conditions appropriate for the two different diffusive systems are required.

2.5.3.1 Olivine Set-up

The initial phosphorus distribution in the 2D olivine maps were assumed to be sharp and drawn as smaller than or equal to two pixels wide (Figure 2.1,2.3). Choosing thin phosphorus zones results in longer diffusion timescales than thick zones. We assumed very thin initial P enrichments in order to recover the maximum duration of cooling. Moreover, high-resolution phosphorus maps reveal phosphorus lamellae are on the order of a μm thick (Figure 2.1).

Lacking independent constraint on the initial concentrations of phosphorus (in addition to the original lamellae thickness, as explained above) we again choose based on the goal of maximizing the retrieved diffusion time. In this case, we take the maximum observed concentration from the high-precision profiles to be the initial P concentration in lamellae. The maximum observed value must be lower than the initial value, if any diffusive homogenization has occurred. This underestimation in the initial concentration serves to maximize the calculated diffusion times, as, if all other variables are held constant, a lower concentration gradient leads to lower diffusive flux (i.e. Fick's first law).

2.5.3.2 Plagioclase Set-up

The initial conditions in plagioclase were set up to simulate the complex "shoulder-shaped" Na zoning after diffusion starting with a normally zoned grain. This normal zoning was, for simplicity, modeled as a step function in Na content (Figure 2.2, 2.3). This maximizes the diffusion timescale; as explained above. The thickness of the rim was determined by trial and error to be the minimum necessary to match the observed shape of the compositional gradient. This choice also maximizes the calculated diffusion times, as thicker bounds require less time for diffusive homogenization to occur. A semi-open boundary on the outside of the grain that permitted a degree of diffusive escape, creating the "shoulder" pattern.

One grain on slide 46 contains a region of exsolved pyroxene on the left side of the grain. Sodium content in this area is generally higher than the surrounding portions of the grain. Therefore, the right side of the grain more accurately preserves the pre-exsolution concentration gradient. The model was therefore optimized to favor the right side of the crystal. This was done by adding a zone of higher sodium content in the interior of the crystal on the left side (Figure 2.2, 2.3). In effect, this reduces the deviation on the left side of the grain, weighing diffusive timescales to be affected more by the region outside of the exsolution zone.

The X-ray map was calibrated using Na concentrations measured along an analytical profile through the width of the crystal. The average Na concentration at the core of the grain was chosen as the concentration for the interior of the grain in modeling. The value of the rim was then picked by finding the total sodium content above the background concentration. This was done using Simpson’s rule for Riemann Sums, which is a method of area approximation using a sum of boxes with caps approximating the curve using simple polynomials. Once the total sodium content above background is known, the sodium density of the rim is fixed so the sodium content is invariant between the model and the data.

2.5.3.3 Initial Temperature

To define initial temperatures, it is necessary to characterize the composition of the parent melt for this system. We attempt to recreate the parent melt using the trapped melt composition of Mg-norite 78235,47 (Sonzogni & Treiman, 2015), combined with O'Sullivan and Neal's (O'Sullivan & Neal, 2013) constraints on 76535 parent melts. Finally, the composition was altered to produce the magnesian olivine and calcic plagioclase compositions reported for this sample(Elardo et al., 2012) using rhyolite-MELTS(Ghiorso & Sack, 1995; Gualda et al., 2012). The resultant liquid composition is reported in Table A-1.

The mineral-in temperatures for both olivine and plagioclase are calculated using rhyolite-MELTS (Ghiorso & Sack, 1995; Gualda et al., 2012). All calculations utilized an oxygen fugacity corresponding to one log unit below the iron-wüstite buffer (IW-1), in order to match the fO_2 inferred from lunar basalts(Papike et al., 1998). Magmas are nominally anhydrous on the Moon(Ganapathy & Anders, 1974), hence phase appearance temperatures increase with pressure (Figure A-1). Diffusion rates increase with temperature, so a pressure of 1 bar was used to maximize diffusion times. If this sample formed deep in the crust, it would have experienced more rapid magmatic cooling than determined here to accommodate the faster diffusion associated with higher crystallization temperatures. The MELTS models predict mineral-in temperatures of 1297 °C (1570 K) for olivine, and 1244 °C (1417) for plagioclase. These values are used as initial temperatures in the diffusion models.

Diffusive relaxation can only begin after the sodic portion of the grain forms. Therefore, to ensure conservative timescales, we chose a starting temperature associated with the most sodic portion of the rim as calculated by MELTS. A concentration gradient must have existed before this temperature, and our initial bounds will start at this lower temperature, essentially both delaying the start of diffusion, and slowing the diffusion that does occur.

As no systematic variation in Mg is detected in the olivine grains, this procedure to lower the starting temperature from the liquidus could not be completed for those crystals, and the liquidus temperature was used as the initial temperature. Skeletal olivine morphology is a hallmark of rapid crystal growth, supporting the validity of this approximation.

2.5.3.4 Diffusion

We model diffusion using both profiles and X-ray intensity maps collected on all samples as output constraints. Fick's Second Law for Diffusion (Equations 2.1 & 2.2, Section 1.3.1) was solved using finite differences in the forward direction (Section 1.3.2).

$$\frac{\partial \mathrm{C}}{\partial \mathrm{t}} = D * \frac{\partial^2 C}{\partial \mathrm{x}^2}$$

Equation 2.1: Fick's second law for diffusion in the 1-dimensional case

$$\frac{\partial \mathrm{C}}{\partial \mathrm{t}} = D \, \Delta C$$

Equation 2.2: Fick's second law for diffusion in the n-dimensional case.

Where C= the concentration at any given point in wt. %, t= time [s], x= position [μm], and D is the diffusivity [$\mu m^2/s$] Defined in Equation 2.3.

$$D = D_0 e^{-\frac{Q}{RT}}$$

Equation 2.3: Diffusivity calculation for the systems utilized here

Here T= temperature [K], R=the ideal gas constant [m^3 Pa K^{-1} mol^{-1}], D_0 is the pre-exponential factor [m^2/s], and Q is the activation energy [m^3 Pa mol^{-1}]. Values for D_0 and Q are from Dohmen (Dohmen, 2002) and Watson et al. (Watson et al., 2015) for olivine and Grove (Grove et al., 1984) for plagioclase. Temperature is recalculated at each time step to follow the cooling path being considered decreasing from the initial temperature for the crystal.

2.5.3.5 Fit coefficients for cooling paths

Fit coefficients were found in the form $T=T_0-a*f(b*t)$, where T=temperature, T_0=Initial temperature, t=time, and constants a,b that we wish to find. Only a certain range of a and b coefficients will produce a cooling function that is continuous and differentiable with respect to the smooth-transition condition (3.9 ˚C/Myr cooling at 850 ˚C after Borg (Borg et al., 2017)). The range of acceptable a,b coefficient pairs were found by repeated diffusion modeling on each crystal. The temperature and temperature rate of change were then plotted as functions of a and b (Video A-1). These plots were then used to guide the choice of the next pair of coefficients, with the aim of interpreting the shape of the two surfaces and finding where they constitute solutions to the smooth-transition condition. Of this range of acceptable values, the solution that provides the maximum diffusive timescale is chosen as the representative function. This is very computationally intensive, and hundreds of thousands to millions of calculations were completed for each crystal, requiring the scripts to be parallelized, and run on the University of Hawai'i's High-Performance Compute Cluster, as well as multiple personal computers.

2.5.4 Thermal Modeling

We construct a simple thermal model to determine the maximum size of a magma chamber that could cool within 20 My, the maximum duration permitted by our thermal modeling of the compositional heterogeneities. The thermal model assumes a spherical, radially symmetrical chamber emplaced into a cool anorthosite crust. This is solved, as for the case of chemical diffusion, by application of finite differences to Fick's second law. In this case:

$$\frac{dT}{dt} = \frac{k}{\rho * c_p} * \frac{dT^2}{d^2r}$$

Where T=temperature [K], t=time [s], k=the thermal conductivity [W/(m*K)], c_p is the specific heat (J/(kg K)], and r is radius [r]. A cooler crust would permit a larger magma chamber to cool within a given time frame. As crustal temperature could be highly variable and we have no independent constraints, we choose a temperature of 650 ˚C (923 K) as an extrapolation of the 18 ˚C/Myr cooling path (McCallum and O'Brien (McCallum & O'Brien, 1996)). Should the crust have been cooler, a larger magma body would be possible. The initial melt temperature of 1297 ˚C, was the same as used in the olivine diffusion models. For the crust, a k=1.76 $Wm^{-1}K^{-1}$, ρ =2730 kg m^{-3} for anorthosite(Pasquale et al., 2015), and a c_p=716 K kg^{-1} K^{-1} of anorthite (Robie et al., 1978). Parameters for the initial melt were: k=1.09 $Wm^{-1}K^{-1}$, ρ =2993 kg m^{-3}, and c_p=1700 K kg^{-1} K^{-} for an olivine-melilitite melt (Büttner et al., 1998). One the temperature dropped below 1229°C, the thermal parameters were switched to troctolitic values (Kelemen et al., 2004): k=3.06 $Wm^{-1}K^{-1}$, ρ =2850 kg m^{-3}.

2.5.5 Electron Backscatter Diffraction

Crystal orientation for five grains on slide 76535, 46 and 76535, 52 was collected using Electron Backscatter Diffraction (EBSD). This technique was completed on a JEOL 5900LV scanning electron microscope operated at low vacuum (11 Pa), using an Oxford Instruments HKL Channel 5 EBSD detector. The slides were prepared by light polishing to remove the existing carbon coat. The prepared surface was sufficiently smooth that beam interaction with the sample surface produced indexible electron backscatter diffraction patterns (EBSPs) without colloidal silica polishing. The samples were tilted at a 70 degree angle relative to the 15 kV electron beam.

Working distances (and thus beam currents) were minimized given the constraints of our instrument's detector geometry. For the olivine in slide , 46, a 20 mm working distance was used for the grain in the bottom right of Figure A-7, and an 18 mm working distance was used for the two points on either side of the truncation. For the plagioclase in slide ,56, a 15 mm working distance was used. Finally, for the two points in the olivine an plagioclase in slide , 52, a 17 mm working distance was used. Background was subtracted using the in-software image enhancement tools in Flamenco acquisition module of Channel 5 (Oxford Instruments) software; the binning, noise reduction, and background frame integration and timing-per-frame values were tuned manually to minimize the acquisition time required to obtain indexible patterns, i.e., EBSPs matching the solutions generated by phases in the American Mineralogist library. As 76535 is a very coarse grained sample, background patterns were usually collected either using a symplectite, or at junctions with more than 5 grains in view. Band detection and indexing conditions (Hough resolution, number of reflectors) were tested iteratively on live Electron Backscatter Diffraction Patterns (EBSPs) to ensure proper indexing in automated mapping jobs.

To collect the data, a 12x12 map was made on each grain. Step size was varied between maps to avoid cracks and any surface debris. The data were post-processed and displayed using the Channel 5 modules Tango (misorientation maps) and Mambo (pole figures).

Chapter 3: The Diffusivity of Phosphorus in Olivine

In preparation as: Nelson W., Hammer J., Shea T., and Chakraborty S., *Re-evaluating the diffusivity of phosphorus in olivine: implications for thermochronology*, Geochimica et Cosmochimica Acta

3.1 Abstract

Skeletal enrichments of the element phosphorus in olivine have been used to address the thermal histories of various igneous rocks. Heterogeneities in the phosphorus content in olivine are more resistant to dissolution events and are resistant to diffusive homogenization than other compositional heterogeneities. This means P heterogeneities preserve petrological information about olivine crystals that have been otherwise eliminated. However, compared to independent determinations of cooling timescales in slowly cooled rocks, P enrichments are sharp to a degree that may suggest a complete lack of diffusive relaxation. Here, we heat olivine with sharp P heterogeneities in a 1-atmosphere gas-mixing furnace for durations of 10 to 20 days at 1400℃, thus exposing them to conditions that should be sufficient for a detectable extent of diffusive relaxation according to existing P diffusivity data. Thin (≤ 0.5 μm) P enrichments are not expected to survive even ten days at 1400℃ using published diffusivity values. However, high-precision chemical analysis of the same interior section before and after heating reveals no difference in the sharpness of phosphorus enrichments. Therefore, diffusion chronometry applied to skeletal P enrichments in

olivine currently provides erroneously short diffusive timescales. We discuss several probable causes for these discrepancies and whether diffusion chronometry should be applied to phosphorus in olivine.

3.2 Introduction

In the quest to understand how different rocky materials formed, one of the most important aspects is the path through time of a material's temperature. This thermal history is rigorously pursued in petrology (e.g., Borg et al., 2017; Chen et al., 2023; First & Hammer, 2016; Helz, 2020; Miyamoto et al., 2009; Mutch et al., 2019; K. Putirka, 2016; Wong et al., 2022) because it exerts a first-order control over many attributes of mineral textures and the distribution of elements among and within crystalline phases. A working understanding of the relationship between temperature and mineral features can be applied in reverse, whereby textures and chemical relations between phases can narrow down the range of a rock's possible thermal histories (e.g. Auxerre et al., 2022; Chen et al., 2023; Costa et al., 2020; Faure et al., 2022; First & Hammer, 2016; Grove et al., 2013; Hammer et al., 2016; K. D. Putirka, 2008; Stolper & McSween, 1979; Wong et al., 2022). However, in many cases, crystallization, subsolidus modification, or other complex post-crystallization processes obscure the high-temperature portion of the igneous history. Diffusion chronometry is a widely exploited technique that can place constraints on estimates of the high-temperature cooling history within a single mineral grain. Diffusion chronometry simulates the diffusive relaxation of chemical heterogeneities within a crystal to approximate timescales (Costa et al., 2003) for any temperatures that are sufficiently high to permit efficient diffusion. This can only be done with careful determination of element diffusivity, which describes how quickly an element diffuses in a material.

Characterizing the thermal history of olivine ($(Mg, Fe)_2SiO_4$) can reap considerable dividends. It is the liquidus phase in many mafic-intermediate silicate melts throughout the solar system. Reconstructing the high-temperature cooling history of olivine reveals key information about the critical earliest stages of crystallization. The most applied diffusive chronometer for olivine leverages the interdiffusion of Fe and Mg in the octahedral site. Mg and Fe diffuse relatively rapidly in olivine, and heterogeneities are not preserved in slowly cooled grains (Mourey et al., 2023). Other elements like Ca, Mn, Ni, and Cr diffuse at rates comparable to Fe-Mg (Coogan et al., 2005; Ito & Ganguly, 2006; Morioka, 1981). Therefore, establishing the potential of using other trace elements like phosphorus in olivine as diffusion chronometers could significantly advance our ability to characterize the thermal history of olivine crystals.

Phosphorus is a trace or minor element in olivine, typically occurring at concentrations lower than 0.4 wt% P_2O_5 (Milman-Barris et al., 2008). Anomalously high phosphorus concentrations are typically distributed in olivine as μm to nm scale lamellae (Milman-Barris et al., 2008, Figures 3.1, 3.2, 3.3). These phosphorus enrichments appear far more complex than the zoning of other elements in the same crystal. Their spatial distribution led to the suggestion that these lamellae are records of the earliest period of crystal grown and are skeletal in nature, not oscillatory (Welsch et al., 2014).

Phosphorus diffuses slowly in olivine (Watson et al., 2015), meaning that it is resistant to diffusive homogenization and can outlast other compositional heterogeneities in a crystal. Phosphorus is sometimes the only surviving chemical heterogeneity in an olivine grain, making it the sole record of the grains' early history (Ersoy et al., 2019; Nelson et al., 2021). Diffusion chronometry involves iterative numerical solutions of Fick's second law ($\frac{\partial C}{\partial t} = D * \frac{\partial^2 C}{\partial x^2}$ in 1-D) until initial conditions diffusively relax to a degree that matches the crystal's measured chemical gradients. To solve for time (t), the initial and final spatial distribution of lamellae (C, x) must be evaluated, and the diffusivity (D) must be well defined. The final spatial distribution of lamellae and their compositions are generally characterized using analytical instrumentation with adequate spatial resolution like electron probe microanalysis (EPMA). However, quantifying diffusivity is a more daunting task requiring controlled laboratory experiments. Relatively small variations in D can lead to large deviations in the timescales retrieved by diffusion chronometry. Diffusivity depends on temperature following the relationship $D \propto e^{-\frac{1}{T}}$. Defining the nature of this proportionality is vital to understanding and utilizing diffusive timescales. However, diffusivity can also rely on a multitude of other terms, such as oxygen fugacity (*f*O_2, Coogan et al., 2005), pressure (Li et al., 2018), the concentration of any element in the mineral (Cherniak, 1995), crystal orientation (Dohmen & Chakraborty, 2007), local radiation (Riviere, 1995), and any other terms that create or modify defects in the crystal lattice. Evaluating each of these terms is a major undertaking, and the contribution of these variables to D can be complicated by the difficulty of determining complex interdependencies. Additionally, elements in a material can have more than one mechanism for diffusion or can be accommodated and diffuse across more than one crystallographic site. Lithium in olivine, for example, has two mechanisms for diffusion. Lithium ions can diffuse either through vacancies in the octahedral sites of the crystal or interstitially through the crystalline lattice (Dohmen et al., 2010).

The diffusivity of phosphorus in olivine has been determined experimentally by Watson et al. (2015). Olivine was coated with a P-rich powder and heated at near atmospheric pressure and moderate (650-850℃) temperatures. They found diffusion coefficients lower than those for most elements in the octahedral site of olivine. These coefficients are consistent with phosphorus heterogeneities consistently being less diffuse than other elements in the same minerals. However, note that D_P is many orders of magnitude larger than tetrahedrally coordinated elements in olivine, like silicon. This diffusivity has since been used in several studies to obtain diffusive timescales across a variety of magmatic systems (e.g., de Maisonneuve et al., 2016; Manzini et al., 2017; Xing et al., 2017; Bradshaw et al., 2018; Baziotis et al., 2019; Albert et al., 2020; Konzett et al., 2020; Lynn et al., 2020; McCarthy et al., 2020; Zhou et al., 2021; Nelson et al., 2021). However, some observations of natural systems appear inconsistent with diffusivities obtained by Watson et al. (2015). There have been multiple discoveries of fine-scale lamellar P heterogeneities preserved in plutonic rocks that are known to have cooled slowly (Suhr, Johnson, et al., 2008; Welsch et al., 2014; Xing et al., 2017). For example, Nelson et al. (2021) find that diffusion timescales obtained using the diffusivities of Watson et al. (2015) for P in olivine are fundamentally incompatible with the long timescales for plagioclase Na/Ca interdiffusion in the same rock. These discrepancies have several possible explanations unrelated to any methodological or analytical errors. First, the extrapolation of this diffusivity above the range Watson et al. (2015) evaluated (650-850℃) could be unreliable (Ellis et al., 1981). The slow-cooling plutonic rocks in which P heterogeneities were observed (Nelson et al., 2021; Suhr, Johnson, et al., 2008; Welsch et al., 2014; Xing et al., 2017) have liquidus temperatures well above 850℃, and diffusion-based analysis could be affected by this problem. Second, Watson et al. (2015) used an $AlPO_4$ powder coated on San Carlos olivine to determine the diffusivity. A phase coating the surface, acting as a P source, may change the diffusive mechanism when compared to natural intragrain processes. The source is comparatively extremely rich in P compared to the concentration of P in natural olivine. Third, the defect structure and mechanisms of diffusion will be different between an intragrain heterogeneity and grain boundary. Fourth, there could be more than one diffusive mechanism for P, as for Li in olivine (Dohmen et al., 2010). In the case of multiple diffuse mechanisms, it is possible Watson et al. (2015) evaluated the faster of two (or more) diffusive mechanisms. Finally, the influence of pressure, fO2, olivine composition, crystal orientation, or other terms have not yet been investigated.

Here, we investigate the diffusive behavior of P in natural magmatic olivine and evaluate whether diffusion chronometry can be reliably applied to obtain timescales. We take a two-pronged approach. 1) We utilize comparative diffusion modeling to compare diffusion timescales between different compositional heterogeneities in a natural sample. 2) We heat olivine grains with controlled T and t at 1-atm to drive diffusive relaxation of pre-existing P-heterogeneities. These will be referred to as comparative diffusion models (CDM) and diffusion dwell experiments (DDE), respectively.

3.3 Materials and Methods

3.3.1 Samples

Grains of olivine containing skeletal heterogeneities in phosphorus were selected for both DDE and CDM approaches. For the DDE, crystals of olivine from the 1820-1823 Golden Pumice from Kīlauea are ideal as they are euhedral and display abundant heterogeneities in phosphorus content (Lynn et al., 2017, 2020). The euhedral crystal shapes made it possible to orient grains without electron backscatter diffraction (EBSD). For the CDM, an olivine crystal from the 1983 Pu'u'ō'ō eruption of Kīlauea previously studied by Shea et al. (2015) was used. They resolved the diffusive timescale for this crystal to be 160- 300 days by Fe-Mg diffusion chronometry.

3.3.2 EPMA

3.3.2.1 Analytical conditions

Micron-scale chemical characterization of olivine was carried out using high precision X-ray quantitative transects, micron-scale qualitative X-ray intensity maps, and submicron-scale qualitative X-ray intensity maps, acquired by the JEOL JXA-8500F field emission electron microprobe at the University of Hawai'i at Mānoa.

Quantitative transects of Mg, Fe, Si, Al, and P were collected using a 15 kV accelerating voltage, a 200 nA beam current, a focused beam, and 90s on peak time. The background was modeled using an exponential fit with the tools provided in Probe for

EPMA v.12.7.2 (PfE). Following Grant and Kohn (2013) and others (McCanta et al., 2016; Milman-Barris et al., 2008; Nelson et al., 2021; Shearer et al., 2013), an apatite standard (USNM 104021) was used for phosphorus. San Carlos (USNM 111312/444) standards with phosphorous concentrations below the detection limit of our instrument were used as blanks, corrected by PfE. These two olivine standards are also used to calibrate Fe, Mg, and Si. A-99 Basaltic glass (NMNH 113498-1) and Springwater olivine (USNM 2566) standards were analyzed as unknowns to track any drift and evaluate analytical accuracy. Ultimately, no drift correction was necessary, and standard analyses remained accurate (<0.02 wt% P_2O_5 variation) throughout the measurements.

Grain-scale x-ray intensity maps of Mg and P were collected using a ten kV accelerating voltage, a 300 nA beam current, a focused beam, and a dwell time of 150 ms. These maps were designed to have a spatial resolution of 1.5 μm, with maps covering entire regions of interest (typically an entire grain). Much finer scale inset maps were obtained on certain grains with a spatial resolution of 0.25 μm. These fine-scale maps require both a low (5 kV) accelerating voltage, and low beam currents (20 nA) combined with very long dwell times (~ 1 second per pixel) to obtain accurate, high spatial resolution P k-alpha maps.

3.3.2.2 Quantifying X-ray intensity maps

Qualitative X-ray intensity maps were converted into quantitative concentration maps by calibrating intensities with quantitative transects. The maps were quantified by averaging pixels within the map corresponding to the radius of the P k-α x-ray interaction volume for each point on the quantitative transect. Averaging was done using the zonal statistics function in ArcMap 10.6.1. The relationship between each point and the corresponding map pixels was framed as a ratio, using methods similar to other studies (Hammer et al., 2016; Lanari et al., 2014). The average of all ratios was then taken and applied to the rest of the map.

3.3.3 Diffusion Dwell Experiments (DDE)

After olivine was extracted from golden pumice, they were washed in hydrofluoric or fluoroboric acid to remove the adhering glass, following the methods of Luhr (2001). The crystals were then mounted in epoxy on a glass slide perpendicular to either the b or c axes using crystal faces and characterized by EPMA. After this initial chemical characterization, olivine grains were reheated in a 1 atmosphere CO_2-H_2 gas mixing furnace with an oxygen fugacity (fO2) corresponding to 1 log unit below the QFM buffer. The runs dwelled for ten days at a constant temperature of 1400 +/- 1℃.

Insertion prior to the experiment, and removal from the furnace hotspot afterwards was done at 800℃. The temperature was ramped up and down at a rate of 200℃ /hr. Samples were then removed and mounted to reveal the same face up. Samples were mounted by laying the original face down on a piece of double-sided tape, pouring epoxy over it in a small mold, then inverting and removing the tape. All crystals then needed to be very carefully polished to remove only the top few microns of material. Polishing was required both to remove pitting and any possible boundary diffusion along the surface of the crystal or vapor phase transport. They were then once more chemically characterized. One sample was reheated a second time for ten days (Figure 3.1).

3.3.4 Experimental Materials

In performing relatively long-duration experiments at high temperatures, we faced the well-known challenge of containing a silicate mineral in a suitably refractory, non-reactive material (Basaltic Volcanism Study project, 1981; First & Hammer, 2016; Grove et al., 2013; Krawczynski & Grove, 2012; Stolper & McSween, 1979). Common metals for holding materials at high temperatures, like rhenium and molybdenum, were tested. However, wraps of both metals became unstable and entirely disappeared during the ten-day run, causing the experiment to auto-quench. We then attempted putting olivine in crucibles made with San Carlos olivine (SCO). Crystals would become thoroughly annealed to the SCO crucibles, making the removal of the crystals from the crucible difficult. The crystal in Figure 3.1 was successfully retrieved from an olivine crucible experiment, though it was cracked in half during extraction. Alumina crucibles completely destroyed any olivine they were in contact with due to their mutual reaction to form spinel. This left Pt as the best material that could remain at these conditions for ten days, but we needed to address the diffusive loss of Fe from olivine to the Pt wires. These experiments require minimal change in the major composition during dwell periods, as the effect of olivine composition on P diffusivity in olivine is unknown. Pure Pt wire diffusively accepts Fe from silicate glasses (Stolper & McSween, 1979; Wagner & Grove, 1997). Pt also accepts Fe from olivine to a degree that olivine near Pt wire in one of the SCO crucibles was several Fo units above the rest of the crystal (Figure B-1).

Adding Fe to Pt allowed us to control diffusive loss/gain of Fe in olivine by modifying the Fe % in the metal to attempt to reach equilibrium. These alloys are stable in the furnaces and do not degrade over multiple ten-day experiments. Alloys were made via electroplating of Fe onto Pt wire following methods similar to Izaki (2010) and First & Hammer (2016), followed by annealing in a 1-atmosphere gas mixing furnace. Electroplating was done in a bath of 25 g of $FeSO_4 \cdot 7H_2O$ in 100 ml of H_2O at room temperature. Fe foil was used as an anode, and coils of Pt wire were used as a cathode. An average current of 50 mA was then used to electroplate the Fe onto the Pt until the mass reflected a gain of Fe at approximately the desired percent. Due to the poor conductivity of the pre-annealed electroplated material, it sometimes took two rounds of annealing and electroplating to reach the desired chemical composition. Annealing was completed in a 1 atmosphere CO_2-H_2 gas mixing furnace with an *ƒ*O2 corresponding to half a log unit below the IW (iron-wüstite) buffer at 1500℃.

The Fe-Pt alloy composition that minimized reaction with SCO was determined through iterative trials over a range in Fe content from 0- 60 wt% Fe. At very high wt% Fe, a variety of oxides form around the olivine (Figure B-2). In contrast, at very low wt% Fe, the Pt wire bore up to half a mm into the olivine crystal (Figure B-3) and modified the bulk composition of the underlying olivine (Figure B-1), though no secondary phases formed. EMPA revealed that a composition of 11.5 wt% Fe minimizes the diffusive exchange of Fe with the slightly more magnesian San Carlos olivine.

3.3.5 Diffusion Modeling

Diffusive relaxation of chemical heterogeneities was modeled through iterative midpoint numerical solutions of Fick’s second law. Modeling was completed in Matlab R2022b. For Fe-Mg interdiffusion in the Pu’u’ō’ō crystal, we use the diffusivity calculated by Dohmen & Chakraborty (2007). Isothermal conditions were assumed in all models, as the DDE are constant temperature (excluding ramping periods, which are short compared to the ten-day run). For CDM, we compare P with other diffusive systems rather than trying to extract an absolute diffusive timescale. For DDE, initial phosphorus distributions are the initial P_2O_5 quantitative map. Initial maps are then modeled to simulate ten/twenty days of diffusive relaxation at 1400℃. CDM models use hand-drawn initial conditions with a maximum lamellae thickness of no more than 1 um wide and use T=1225℃ to match Shea et al. (2015).

3.3.6 Comparing Lamellae in DDE

Artifacts resulting from sectioning affected all crystals to some degree during the DDEs. Some grains fractured when they were extracted from their mounts, which imparted large distortions to P heterogeneities. However, all crystals had to be polished to remove surface diffusion, which also removed the uppermost parts of the grains, which could impart similar geometric effects to P heterogeneities. Therefore, it was necessary to determine the average lamella thickness and adjust for sectioning effects that distort the apparent lamella thickness and spacing. A comparatively straightforward way of approaching this problem is by applying a method of analysis used in remote sensing, where pixels along a linear feature of interest are averaged (Telbisz et al., 2013) to produce a “swath topographic profile”. Swath profiles are created using a rectangular swath over a region on a digital elevation model (DEM), which are averaged perpendicular to a line of interest. In olivine, P heterogeneities are highly linear (Figures 3.1, 3.2, 3.3). The linearity of these heterogeneities allows swath profile analysis to be applied to a quantitative P X-ray map. This method (swath topography) provides a way to resolve high-resolution characterizations of individual linear phosphorus enrichments with higher signal-to-noise ratios (Figure 3.1).

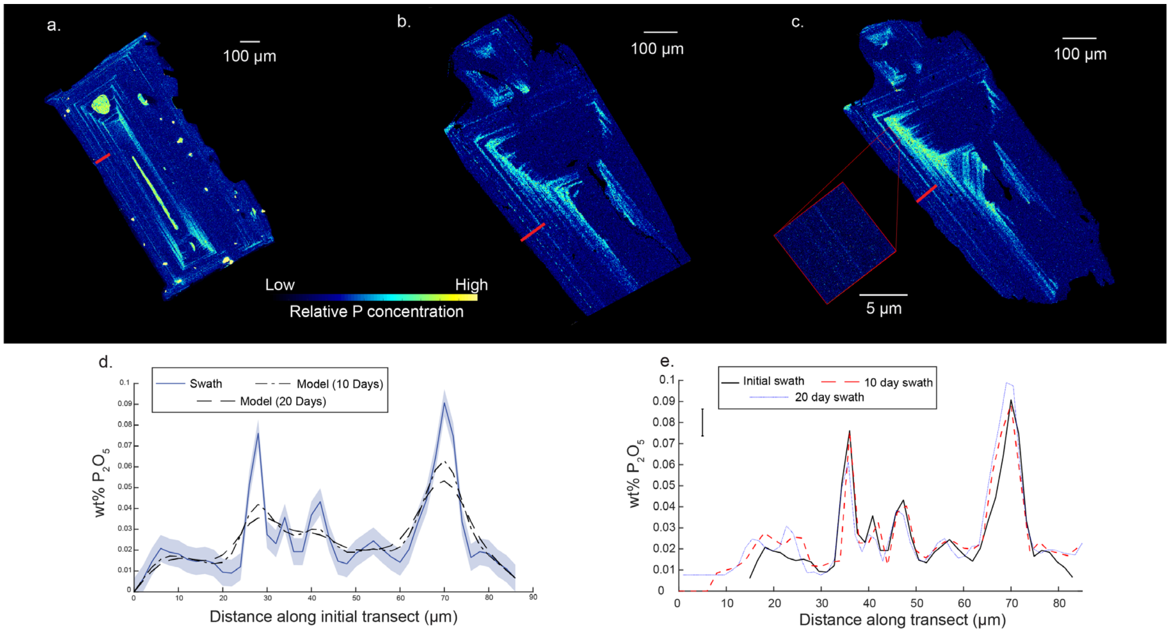

Figure 3.1: Phosphorus heterogeneities in Kīlauea olivine prior to and after reheating for a total of twenty days at 1400 °C. **a.** Phosphorus X-ray intensity map of the grain prior to heating. **b.** X-ray intensity map of the same grain after dwelling ten days at 1400 °C. Note that the grain was partially destroyed due to sintering with the olivine crucible, which prevented re-mapping of the same surface without sectioning effects. **c.** the same grain after an additional ten days of heating. The inset map reveals the persistence of lamellae <0.5 μm in width. **d.** Swath topographic analysis of initial grain. The blue region is the analytical error envelope for the quantitative analysis. Dashed lines show the expected diffusive relaxation of lamellae after ten and twenty days of heating at 1400 °C. **e.** Swath profiles of the same lamellae in all three datasets are superimposed. Note that no diffusive relaxation was detected. The error bar in upper left is representative for all analyses shown.

Once swath profiles of phosphorus heterogeneities were acquired before and after an experiment, several steps were taken to acquire swaths and compare datasets.

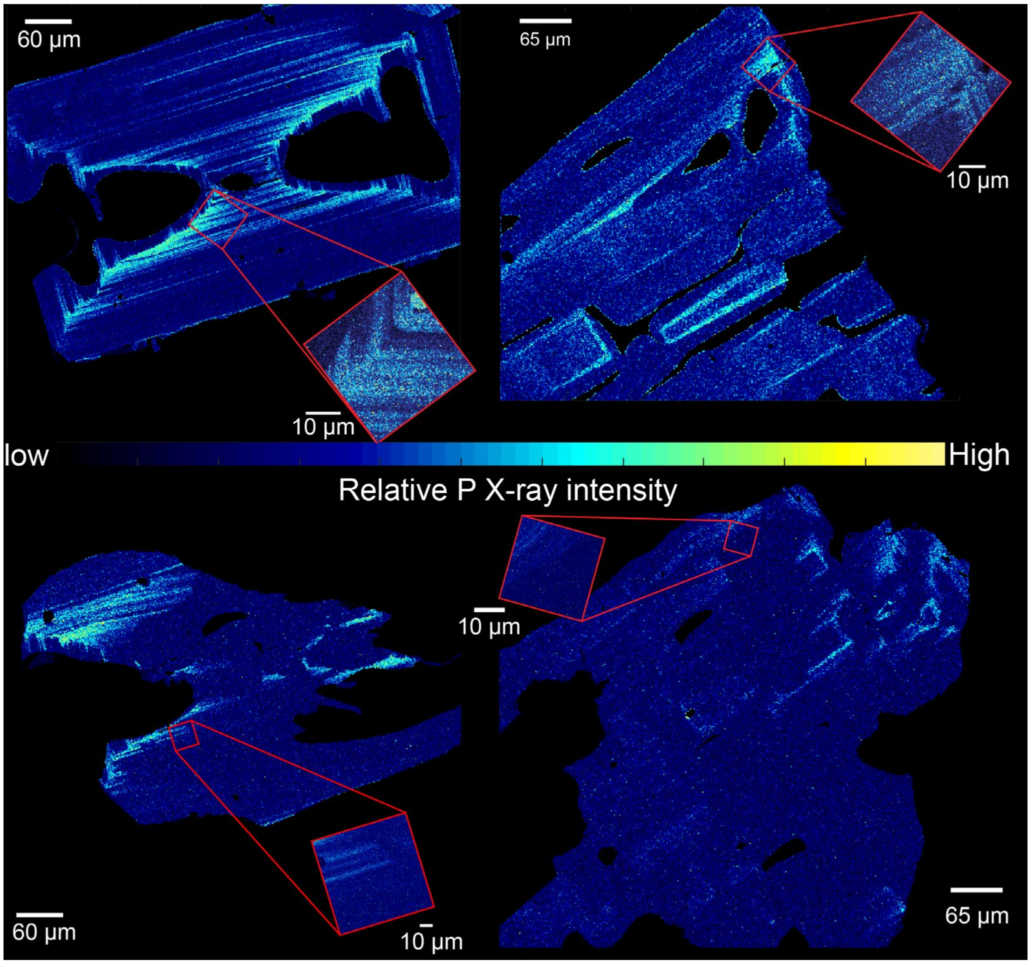

Figure 3.2: X-ray intensity maps of two other Kīlauea crystals that were reheated to 1400 °C for 10 days. Note in the crystal on the left, both insets record evidence of <0.5 μm lamellae of P. The crystal on the right underwent significant pitting, so the original face was polished through and due to the clustered nature of this crystal, it is difficult to correlate any lamellae. However, the lamellae remained sharp to the resolution of our microprobe after reheating.

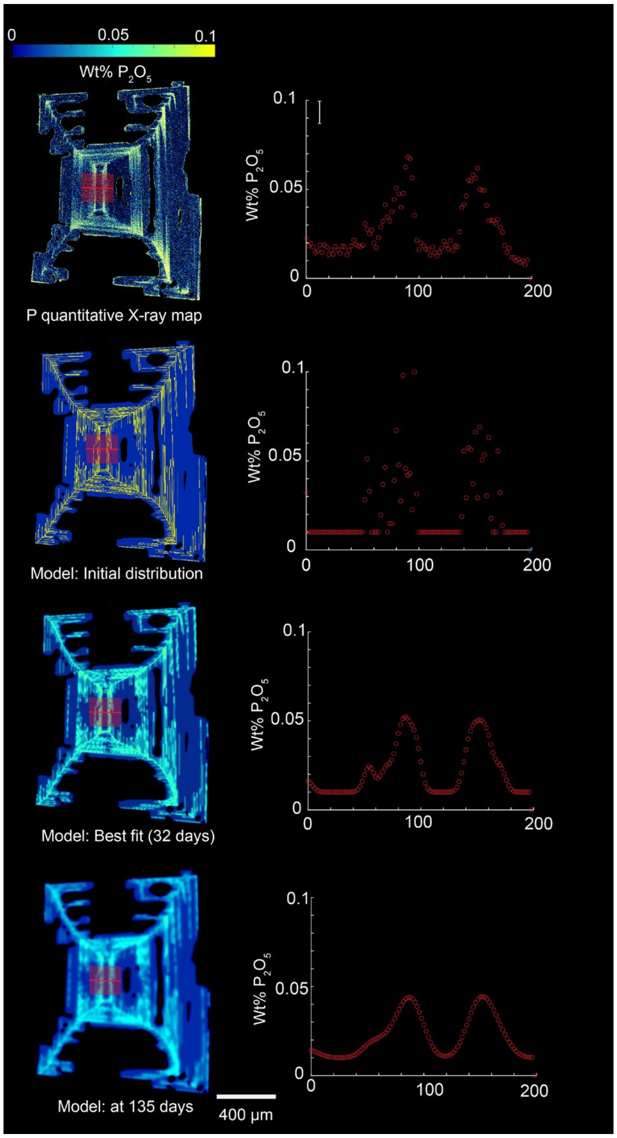

Figure 3.3: Modeling results for the Pu'u'ō'ō olivine. The model best matches the quantitative EPMA map (Left) after only 63 days of diffusive relaxation. When the model is run for 135 days (timescale obtained from Fe-Mg diffusion), the lamellae are far more diffuse than in the X-ray intensity map of the natural crystal.

First, qualitative x-ray maps were calibrated independently to quantify relative x-ray intensity into wt% P_2O_5 (See section 3.3.2.2) and imported into ArcMap 10.6.1. Then, one lamella was traced in both the before and after experiment P maps. Using the editing tool, a second line was drawn orthogonally to the first. Swath topography was then run using a custom ArcMap tool. The results were then exported to a spreadsheet, where they could be plotted and compared. In any usable profile, there were multiple identifiable peaks. These peaks were corrected for sectioning effects by choosing two peaks and stretching one profile to fit the other using the two-point equation for a line. Other peaks were used to ensure that a good fit was obtained (Figure 3.1).

3.4 Results

3.4.1 Comparative Diffusion Model

The crystal from the Pu'u'ō'ō eruption of Kīlauea (Shea et al., 2015), provides an independent way to evaluate the diffusive relaxation of P heterogeneities. Shea et al. (2015) used zoning in Mg-Fe composition within this crystal and determined a diffusion timescale of 135 days at a temperature of 1225℃. This crystal also has skeletal P enrichments that experienced, at minimum, a similar period of diffusive relaxation. P diffusion chronometry yields a timescale of only 28 ± 1 days, which is far too short to be explained through error and differences in known diffusive behaviors between the two systems. After 135 days, the heterogeneities are expected to be far more diffuse, to a degree incompatible with the distribution of P within the grain (Figure 3.3).

4.4.2 Diffusion Dwell Experiments

In all three experimentally heated crystals, thin lamellar heterogeneities in phosphorus content were characterized by EPMA. Within the resolution afforded by

EPMA, no diffusive relaxation was detected in any experiment (Figures 3.1, 3.2). We used swath topography on a lamella before and after the experiment to test for very small degrees of diffusive relaxation. We then compared them to profiles predicted by diffusion models using the diffusivity coefficient of P in olivine determined by Watson et al. (2015) (Figure 3.1). Models showed that significant, easily detectible relaxation should have occurred (Figure 3.1). This applies to all three grains of olivine, with single lamellae thinner than the 0.5 μm resolution of the microprobe still present in all three grains (Figures 3.1, 3.2, section 3.5.2). For all three experiments, the maximum diffusivity consistent with the absence of observable diffusive relaxation is $3.43 \cdot 10^{-7}$ $\mu m^2/s$ at 1400 °C. The calculated diffusivity for P at 1400℃ is $6.18 \cdot 10^{-6}$ $\mu m^2/s$ using the expression of Watson et al. (2015), at least an order of magnitude faster than our experiments suggests at this temperature.

3.5 Discussion

3.5.1 Diffusivity of P in Olivine

We find no evidence of diffusive relaxation of phosphorus in olivine, and our models reveal that diffusive timescales of P in olivine are incompatible with the Mg-Fe interdiffusive timescale in the same crystal. Our results shed light on the unanticipated presence of P heterogeneities in slowly cooled, plutonic rocks from Earth (Welsch et al., 2014; Xing et al., 2017) and the Moon (Nelson et al. 2021). In the latter study, Nelson et al. (2021) model diffusive timescales from lunar troctolite 76535 using P in olivine and report timescales many orders of magnitudes shorter than independent determinations of the rocks cooling history from Na-Ca diffusion timescales (Nelson et al. 2021) and multipoint radiothermometry (Borg et al., 2017). Diffusion chronometry applied to olivine crystals using the diffusive coefficients determined by surface powder source (Watson et al., 2015) consistently underestimates diffusive timescales.

Our results do not imply that the diffusivity of P in olivine defined by Watson et al. (2015) is incorrect. There is still much to be learned about how P is incorporated into the structure of olivine and the exact reactions involved in its diffusive migration. It is possible that P has multiple diffusion pathways in olivine and that Watson et al. (2015) may have resolved the fastest. Our results suggest that internal skeletal heterogeneities of phosphorus may need to be treated differently than P diffusing inwards from an adjacent P-rich phase, a situation that is more comparable to an $AlPO_4$ powder coating as used in Watson et al. (2015).

We consider the effects of crystal chemistry and site occupancy on P partitioning and diffusion to better explain the discrepancies between our results. There is evidence that P is tetrahedrally coordinated with oxygen in olivine (Boesenberg & Hewins, 2010; Buseck & Clark, 1984). The abundances and behaviors of point defects in the tetrahedral site of olivine have yet to be fully characterized, making it difficult to determine possible relationships between all the possible variables such as P, *f*O2, major element concentration, etc. and the diffusivity of phosphorus.

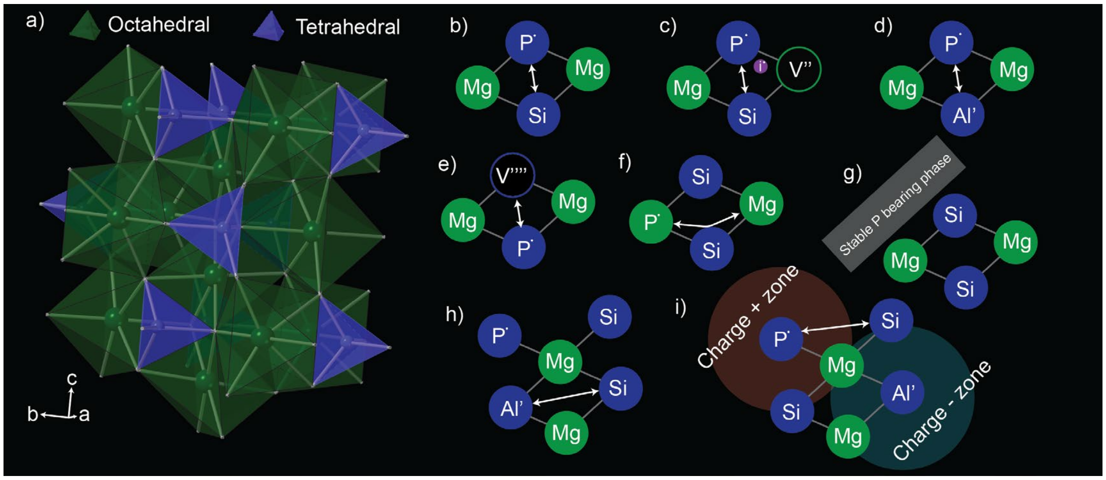

Figure 3.4: Olivine’s structure, and how phosphorus may behave in it. a) Stick-and-ball model of olivine’s structure, simplifying the structure into only octahedral and tetrahedral sites. b) Zoom in of four sites, representing interdiffusion of phosphorus and silicon atoms through a direct tetrahedral site to tetrahedral site jump. Note that this situation is not charge balanced, as the P atom in the tetrahedral site provides a +1-charge defect, as represented by the dot, following Kröger-Vink notation. c) A possible way to charge balance the reaction in (b). An interstitial ion such as Li, Na, or H provides an additional +1 charge, which is then balanced by a vacancy in the octahedral site, provide a -2 charge. d) a charge balancing reaction where an Al substitution on the tetrahedral site provides a -1 charge. e) An occasional vacancy in the tetrahedral site (at a rate of 1 vacancy per 4 P defects) could also provide a charge balancing mechanism (similarly 1 octahedral site vacancy per 2 P defects would work). f) Scenario where P3+ occupies the octahedral site in olivine’s lattice. This will likely diffuse more rapidly, like other octahedral site cations in olivine, given it is charge balanced. g) A stable phase which doesn’t chemically interact with the rest of olivine’s structure in any significant way. h,i) If P incorporation in olivine is reliant on other trace elements in olivine (such as in c or d) which diffuse faster than P, charge instability could provide a driving force to increase the transfer of P through the lattice.

Several diffusive mechanisms could exist for P to diffusively travel through the lattice of olivine (Figure 3.4a). In Figure 3.4a, we remove the oxygen sites for visibility, as none of these mechanisms will utilize them. Cations occupy either octahedral (oct) sites, (e.g. Mg,Fe^{2+}), or tetrahedral (tet) sites (mainly Si^{4+}).

We assume that phosphorus typically occupies the tetrahedral site in olivine due to its 5+ charge state, making it unsuitable for the octahedral site, and the fact that the atom is too large to travel interstitially in olivine's structure (Condit, 1985). One possibility is that the migration of P has an interdiffusive relationship with Si (Figure 3.4 b), with a diffusivity closer to the diffusivity of silicon. The diffusivity of silicon in olivine (Houlier et al., 1990) is several orders of magnitude lower than the value determined by Watson et al. (2015) for phosphorus. A diffusivity closer to that of silicon in olivine is consistent with the lack of observable diffusive relaxation throughout our experiments. How exactly this reaction is charge balanced remains to be seen: perhaps with interstitial H, Li, or Na atoms increasing the charge imbalance to +2, and a vacancy in the M site (-2) bringing the net charge to neutral (Figure 3.4 c, Eqn 3.1 a, Lynn et al., 2020). Another possibility would be coupled substitution of P^{5+} and Al^{3+} in the t site (Figure 3.4 d, Eqn 3.1 b, Shea et al., 2019). Should Al, H, Li, or Na atoms in olivine assist in providing charge neutrality, as they all diffuse through olivine's structure faster than P, this could provide a driving force to enhance diffusion, temporarily leaving stationary P atoms in invalid charge states, while providing nearby electrically suitable sites for the atoms to rest (Figure 3.4 h,i). Note that Watson et al. (2015) used an $AlPO_4$

source, so Al would be abundant to assist in this reaction, perhaps increasing apparent diffusivity.

a) $Mg_{oct}^{x} + \square_{oct}'' + X_{i}^{\bullet} + P_{tet}^{\bullet}$ b) $P_{tet}^{\bullet} + Al_{tet}'$

c) $4P_{tet}^{\bullet} + \square_{tet}''''$ d) $2P_{tet}^{\bullet} + \square_{oct}''$

Equation 3.1: Kröger-Vink notation of charge balance mechanisms. a) Interstitial charge balance with X= Li, Na, or H. This communicates that a magnesium atom exists in the octahedral site of the crystal, giving no charge defects, a vacancy exists in another octahedral site, giving a -2 charge defect, there is an interstitial lithium ion providing a +1 charge defect, and a phosphorus atom in the tetrahedral site giving a +1 charge defect. b) Charge balance using coupled Al/P substitution. C) charge balancing through tetrahedral site vacancies. D) Charge balancing through octahedral site vacancies.

Given the diversity of diffusive mechanisms, it is easy to see how our observed diffusivity (or lack thereof) could differ from the powder source method of Watson et al. (2015). In the powder source method, a 60:40 wt mixture of San Carlos olivine and $AlPO_4$ powder is heat treated, ground, and applied to the surface. This means there is an ample supply of olivine bearing Al near the surface (which was intended to ensure the P entered the olivine lattice), potentially speeding up diffusive relaxation (Figure 3.4 h,i). A related cause of more rapid diffusivity has to do with vacancy generation. The more vacancies that exist on a site, the faster elements can diffuse through that site. Given the presence of $AlPO_4$ near olivine at high temperature, vacancies could be produced by some balance of Al entering the octahedral site and tetrahedral site vacancies. The diffusivity of P could be related to local phosphorus content due to distortion of the lattice (Shea et al., 2019). Watson et al. (2015) find concentrations as high as 3 wt% P_2O_5, which would exasperate this difference. Another possibility has to do with diffusive domains. Diffusive regimes refer to regions where the Arrhenius slope in T/D space remains constant (Chakraborty, 2010). For diffusion in the octahedral site of olivine, three major diffusive mechanisms change over T, compositional, and fO2 space: intrinsic, extrinsic, and transition metal extrinsic domain (TaMED) (Chakraborty, 2010; Dohmen & Chakraborty, 2007). Intrinsic diffusion is only expected to occur at high temperatures (>1500℃) and high crystal purity, which is probably not relevant here. The extrinsic domain is dominant at <800℃, which is relevant to the experiments of Watson et al. (2015). The TaMED domain is dominant at intermediate temperatures and in low purity samples, most relevant to our experiments. If these domains behave similarly in tetrahedral sites as octahedral sites in olivine, our experiment likely spans a different diffusive domain than Watson et al. (2015) which could contribute to the observed offset. Finally, natural phosphorus lamellae could represent a stable phase in olivine, where this stable phosphoran olivine phase, akin to clinohumite lamellae in olivine (Wirth et al., 2001), exists at equilibrium with the surrounding olivine. In this case, no diffusion would occur in the natural sample but could proceed in the powder-source experiments.

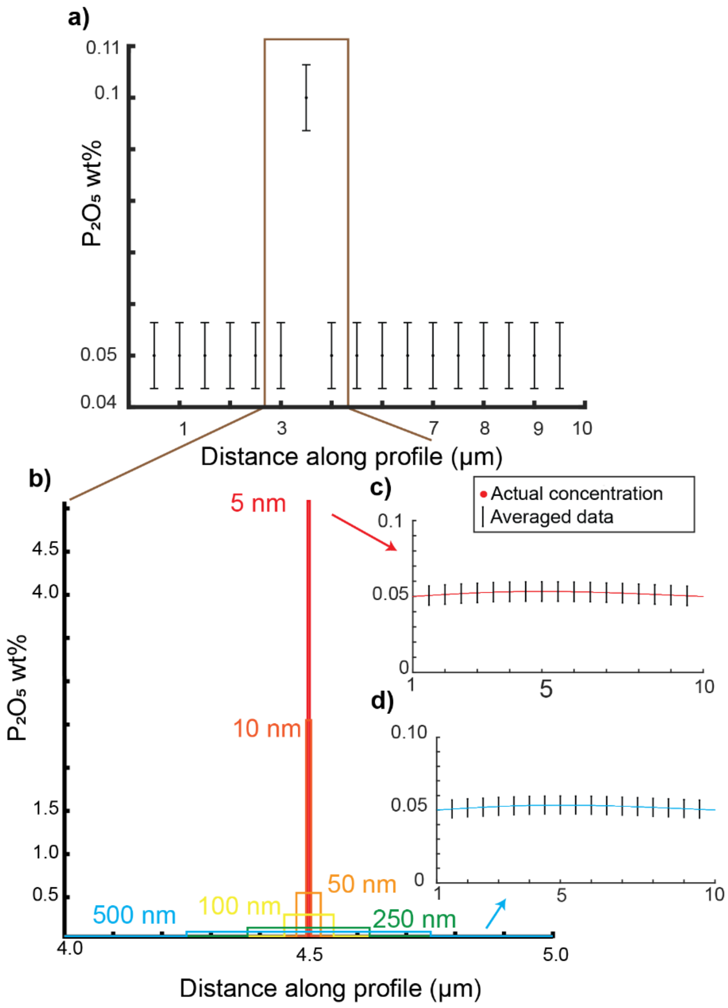

Figure 3.5: Nanometer scale (5-500 nm) diffusion models for P in olivine. a) A theoretical profile, where a single 0.5 µm phosphorus enrichment of 0.1 wt% P2O5 in an olivine grain is surrounded by olivine with 0.05 wt% P2O5. b) The variety of phosphorus enrichments that could occur in these 0.5 µm that the microprobe would still measure as (a) given its spatial resolution. c) Model showing a 5 nm phosphorus enrichment undergoing diffusive relaxation for ten days at 1400 °C. d) A 500 nm phosphorus enrichment undergoing modelled diffusive relaxation for ten days at 1400 °C. These models indicate that any P lamellae 5 nm to 0.5 µm in size would homogenize within those timescales if current P diffusivity values were adopted.

3.5.2 Ultrafine Phosphorus Lamellae: Implications for Diffusion Models

We also explore the implications of P enrichments that are very fine in scale (e.g., a few nm), and that their diffusive relaxation is therefore poorly resolved by even high spatial resolution instruments like the FEG-EPMA. If these lamellae are <5 nm wide (Chapter 4), is it possible that diffusive relaxation has taken place (i.e., within one pixel of an EPMA map)?

To test the effects of analytical resolution on our capacity to detect diffusion, we carried out a diffusion model that simultaneously modeled diffusion on the nm scale while simulating the 0.5 μm beam width of an electron microprobe analyzing the sample. First, we modeled nm scale P diffusion and then averaged the data in 0.5 μm sized bins to simulate the microprobe's beam size. A variety of heterogeneities between 5 nm and 0.5 μm in thickness were tested. The concentrations of these lamellae were stipulated to vary relative to their thickness such that the averaged concentration over the 0.5 μm length of the beam remains constant. For example, a single 200 nm wide P heterogeneity would need to have a concentration of 0.175 wt% P_2O_5 for the average P_2O_5 content across the 0.5 μm bin to be 0.1 wt%, while a single 10 nm wide lamella would have a concentration of 2.55 wt% P_2O_5. In all scenarios, heterogeneities were diffusively homogenized after ten days at 1400℃ (Figure 3.5). These results show that no lamellae on the order of 0.5 μm can survive ten days at 1400℃ if current diffusion coefficients (Watson et al., 2015) are used. Our DDE and CDM results are compatible with phosphorus-rich lamellae being either nm or μm-scale.

3.5.3 Implications for chapter 2, and diffusion chronometry

The results of this chapter bring into question the results of chapter 2 as well as all other studies that utilize phosphorus in olivine as a diffusive chronometer. Any studies with conditions similar to ours that utilized the diffusivities provided by Watson et al. (2015) have under-reported diffusive timescales. This includes the D_P results in chapter 2. However, in chapter 2 we used a much smaller diffusivity, which may still be consistent with these results. Further, the more conservative max cooling timescales from plagioclase were leveraged as the primary argument for rapid cooling through high temperatures in 76535.

Assuming that phosphorus is stable in olivine, that does not mean this phase is useless for diffusion chronometry. A primary concern in diffusion chronometry is accounting for diffusion vs growth (Shea et al., 2015). This is typically done using heterogeneities of an element with low diffusivities to create initial conditions in modeling (Shea et al., 2015; Mutch et al. 2019; Chapter 5). We posit that our results would suggest P is the most high-fidelity indicator of initial olivine distribution in olivine and can be used to determine what gradients are caused by growth, or diffusion.

3.6. Conclusions

Skeletal P enrichments in olivine provide a unique record of the earliest moments of olivine crystallization. These enrichments have been used in diffusion chronometry to retrieve quantitative residence timescales in a diverse variety of rocks (e.g. de Maisonneuve et al., 2016; Manzini et al., 2017; Xing et al., 2017; Bradshaw et al., 2018; Baziotis et al., 2019; Albert et al., 2020; Konzett et al., 2020; Lynn et al., 2020; McCarthy et al., 2020; Zhou et al., 2021; Nelson et al., 2021). We have evaluated this potential tool, and our results show that diffusion chronometry using phosphorus in olivine is unsuitable in isolation to determine residence timescales until the diffusive behavior of phosphorus in olivine is better understood. In particular, we show that skeletal phosphorus heterogeneities show no evidence of diffusive relaxation, and our results suggest they may be totally unsuitable for diffusion chronometry studies. Whether diffusive relaxation of these heterogeneities occurs at all awaits advanced nanoscale analysis.

Chapter 4: Nanoscale characterization of phosphorus in olivine

In preparation as: Nelson W., Hammer J., Ishii H., Parman S., Shea T., Akey A., Ohtaki K., Hellebrand E., and Bradley J. *Nanoscale Characterization of Phosphorus in Olivine: Taking apart olivine's skeleton*

4.1 Abstract

Lamellar enrichments of the element phosphorus preserve otherwise obscured information about magmatic conditions in the early stages of crystal growth. Despite intense study and documentation of the lamellae in a wide variety of rock types, there is still much to learn about how these chemical heterogeneities form and how they can be used to understand the crystals within which they reside. Here, we investigate phosphorus-rich lamellae in olivine crystals using electron probe microanalysis, transmission electron microscopy, and atom probe tomography to investigate the length scale, absolute P concentration, and elemental covariation of the lamellae. We find lamellae are significantly thinner, as thin as 5 nm in both extrusive and plutonic olivine. We also find a consistent anticorrelation in the concentration of P with Mg and Si, pointing towards a charge-balancing mechanism involving vacancies in the octahedral site compensating for phosphorus in the tetrahedral site.

4.2 Introduction

Olivine is one of the most common minerals in igneous rocks of the solar system (Basaltic Volcanism Study project, 1981; McSween, 1999) and usually the liquidus phase of mafic magmas (Basaltic Volcanism Study project, 1981; Bowen, 1956; Rapp & Draper, 2018). The early appearance of olivine in a crystallization sequence means that it records environmental details (Thermal, compositional, and other details) from the onset of crystallization and a large temperature range of stability. Olivine crystals continue to grow and preserve information for the majority of the subliquidus history of mafic igneous rocks.

Intragrain chemical heterogeneities can be vital to understanding the history of an olivine grain. The distribution of chemical heterogeneities can record crystallization and dissolution events through disruptions to the expected zoning behaviors within a grain (Chapters 2, 5; Giuliani, 2018; Libourel & Portail, 2018; Mourey et al., 2023). The chemical contents of a heterogeneity can record the state of the surroundings of the olivine. This can include evolution of the surrounding liquid's composition (Dana & Ford, 1932; de Maisonneuve et al., 2016), the oxygen fugacity (Dodd, 1981; Krot et al., 2014; McSween, 1999),approximately how quickly the crystal grew (de Maisonneuve et al., 2016; Milman-Barris et al., 2008; Welsch et al., 2014), and temperature (Putirka, 2008). Importantly for the studies in this dissertation, the degree of diffusive relaxation of initially sharp heterogeneities reflects the time temperature cooling history of a magma. Thus, time scales can be retrieved through the application of diffusion chronometry (Costa et al., 2003, 2020) given adequate knowledge about the diffusive mobility and spatial distribution of the element in olivine.

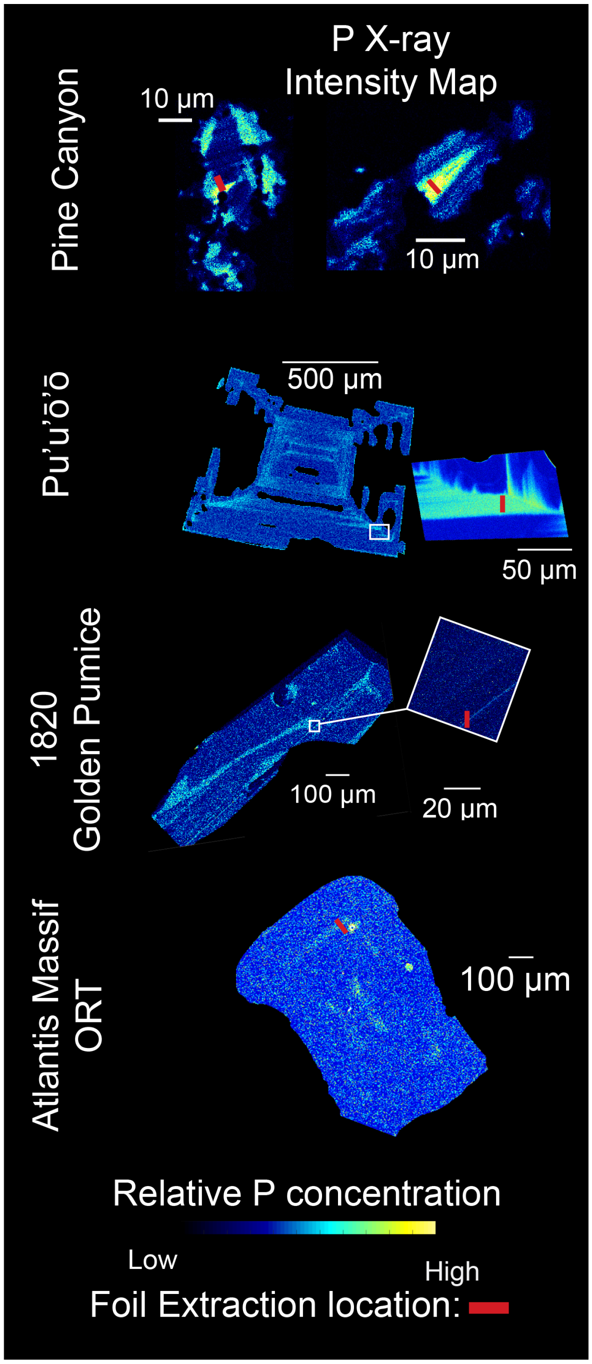

Figure 4.1: Materials analyzed with TEM and APT.

The chemical composition of olivine can vary within a grain in several ways. As discussed in Chapter 1, olivine is made up of a lattice of octahedrally and tetrahedrally coordinated cations bonded to oxygen atoms. The octahedrally coordinated cations have received the most study when it comes to spatial variations in elemental concentration within a single grain, here referred to as “heterogeneities”. The most common heterogeneities involve covariation of Mg and Fe^{2+}, defining the forsterite-fayalite solid solution (Dana & Ford, 1932; Chapter 1). Other elements Ca, Cr, Al, Ni, and Mn can also substitute on the octahedral site. Cations like H^+, Li^+, and Na^+ can be occupied interstitially in olivine’s lattice. Small ionic radius, high valence elements like Fe^{3+}, Al, P, and Ti can substitute for Si on the tetrahedral site (Berry et al., 2007; Evans et al., 2008; Hartman, 1969). Chemical heterogeneities of elements that exist in the tetrahedral site provide an important tool for diffusion chronometry, as their generally low mobilities can be used to gauge whether a gradient is due to diffusive relaxation or crystal growth from a changing liquid composition (Shea et al., 2015). Phosphorus is often treated similarly to Al, as it is often the sharpest (and even the last detectable) heterogeneity in many samples (Ersoy et al., 2019; Milman-Barris et al., 2008; Nelson et al., 2021). It has been suggested that P, like Ti, may occupy the tetrahedral site in olivine, as is assumed in previous chapters (Buseck & Clark, 1984). However, phosphorus most often takes a 5+ charge state in relevant systems (Bindi et al., 2023). So, it remains unclear how phosphorus would occupy this site while maintaining charge balance in the crystal. A clear understanding of how P is accommodated in olivine would constitute a valuable tool for understanding the mechanism of diffusion of this element in olivine.

Phosphorus heterogeneities in olivine typically present as a complex series of lamellar enrichments (Milman-Barris et al., 2008) (Figure 4.1). These lamellar enrichments record the very first moments of rapid dendritic crystallization of olivine (Welsch et al., 2014). Therefore, these heterogeneities of P could provide a rare look into the earliest moments of crystallization. However, these lamellae are often thin relative to the beam size and interaction volumes of EPMA, which is around 0.5 microns

(Chapters 2 and 3). The fine scale nature of these lamellae can make it difficult to apply diffusion chronometry to this system, as it makes the vital step of determining initial conditions of the system impossible (e.g., de Maisonneuve et al., 2016; Manzini et al., 2017; Xing et al., 2017; Bradshaw et al., 2018; Baziotis et al., 2019; Albert et al., 2020; Konzett et al., 2020; Lynn et al., 2020; McCarthy et al., 2020; Zhou et al., 2021; Nelson et al., 2021). A major requirement in understanding this system is to constrain how thin these lamellae can be.

The questions of how P is incorporated into olivine, and the dimensions of these phosphorus heterogeneities can be addressed using transmission electron microscopy (TEM) and atom probe tomography (APT). TEM can investigate the structure of a crystalline lattice through the diffraction of electrons transmitted through an ultra-fine foil of material. In contrast, APT allows for the nanoscale 3D characterization of elements within a material by ionizing small amounts of a 200 nm thick needle of a material and analyzing the composition of ions using a time-of-flight mass spectrometer. This creates a 3D map of each ion in the needle, providing atom-scale spatial resolution (Reddy et al., 2020). With APT, we should be able to determine how P is incorporated into olivine by checking for correlations between elements, and directly imaging lamellae to measure their thickness. Though P has been measured on grain boundaries in olivine using APT (Cukjati et al., 2019; Tacchetto et al., 2021), there has been little research on intragrain heterogeneities with this instrument. Therefore, an independent goal of this chapter is to show that APT is suitable for the study of intragrain heterogeneities within a single olivine crystal.

4.3 Materials and Methods

4.3.1 Materials

Olivine crystals containing a variety of concentrations and spatial distribution of phosphorus enrichments were analyzed. Foils were extracted from seven different olivine crystals, all hosting P heterogeneities.

A phosphoran olivine sample was analyzed first, as the high overall P concentration increases the chance of achieving a clear signal. We used a sample from Pine Canyon in Piute county, Utah (Figure 4.1). This sample has previously been reported to contain up to 6.1 wt% P_2O_5 in its olivine (Agrell et al., 1998), meaning it should be relatively easy to characterize P with EPMA, TEM, and APT. However, the heterogeneities in this sample are not skeletal (Figure 4.1), as in many igneous olivine crystals (Milman-Barris et al., 2008; Welsch et al., 2014). Further, this sample may have been formed hydrothermally (Agrell et al., 1998). Thus, any observations of P including size, distribution, or concentration in this sample may not be generalizable or relevant to igneous olivine.

Two crystals from Kīlauea volcano were selected to represent volcanic olivine grains. These crystals were selected from the same samples examined in Chapter 3. The first olivine is from the 1983 Pu'u'ō'ō eruption of Kīlauea studied by Shea et al. (2015) was used in the CDM. The other is from the 1820 golden pumice used in the DDE. Specifically, a fractured portion of crystal 2 from Chapter 3 (Figure 3.1, 4.1) was analyzed to study a lamella after 10 days of high temperature dwell.

Finally, we used an olivine rich troctolite previously studied by Welsch et al. (2014). This sample is a coarse grained and well annealed troctolite collected from the Atlantis Massif seamount, recovered from hole U1309D, IODP expedition 304/305 (Suhr et al., 2008). It is a slowly cooled plutonic sample that still has phosphorus heterogeneities mapped and referenced in Chapter 2 (Figure A-4). Its lamellae appear diffuse in EPMA (Figure 4.1) and serves as a study of diffusively relaxed P heterogeneities.

4.3.2 Electron Probe Microanalysis (EPMA)

Secondary electron images and x-ray intensity maps were acquired using the JEOL JXA-8500F at the University of Hawai'i at Mānoa. High-resolution x-ray maps were acquired using a beam scan operating with a 5 kV accelerating voltage, a 1000 msec dwell time, and a 20 nA beam current to guide material extraction. The low current and long dwell times allowed us to accurately map at a resolution of ~0.25 μm per pixel, as beam diameter decreases at low current (Section 1.2). Further, three WDS spectrometers simultaneously analyzed phosphorus, and their intensities were aggregated.

A large collection of quantitative chemical analyses from profiles on the Pine canyon olivine, the 1820 golden pumice olivine, the 1983 Pu’u’ō’ō olivine, and olivine from the Kīlauea iki lava lake were compiled. P, Mg, Fe, Si, and Al data were each normalized to 100% within each sample to highlight local variations in composition.

4.3.3 Atom Probe Tomography (APT)

X-ray intensity maps were used to guide the extraction of foils at Harvard University Center for Nanoscale Systems (CNS) using a Zeiss Crossbeam Focused Ion Beam Scanning Electron Microscope (FIB-SEM). Cuts were made using a 7 nA 60 nC/μm^2 Ga$^+$ beam using the triangular prism method (Reddy et al., 2020). After the foil was extracted, it was welded onto posts and cut into approximately 200 nm wide rods. These were then cut into sharp needles suitable for APT analysis (Figure C.1).

Needles were analyzed using a Cameca 3D Local Electrode Atom Probe (3D-LEAP) 4000X HR at CNS. Operating conditions involved an 80-100 pJ pulse energy with a 355 nm laser, at a frequency of 100 kHz, at a base temperature of 40-50 K. The resulting spectra were reconstructed in Cameca IVAS 3.8.10. SEI images of each needle were used to reconstruct tip shape during reconstruction. The peaks were then identified by mass/charge ratio. For compositional analysis, peaks of overlapping mass/charge ratio were deconvolved using the built-in decomposition of peaks tool.

4.3.4 Transmission Electron Microscopy (TEM)

Foils for TEM were extracted from the samples using a Helios NanoLab 660 Dual Beam FIB at the University of Hawai'i at Mānoa. Cuts were generally made using the same method as for APT (Section 4.3.2), but then thinned and placed onto appropriate TEM grids, rather than cut into needles. Some experiments were made on the dependence of foil thickness leading to the tri-foil sample in Figure C.1.

TEM foils were analyzed with the FEI Titan 3 G2 60-300 dual aberration-corrected TEM at the University of Hawai'i at Mānoa. Samples were analyzed with EDS to characterize regions of P heterogeneities and observe relative variations in other elements. Bright-field imaging using an objective aperture combined with nanobeam diffraction (NBD) allowed for the analysis of lattice properties. Finally, high-resolution transmission electron microscopy (HRTEM) images of boundaries were collected to characterize any defects in the lattice.

4.3.5 Statistical Analysis

Primary statistical analysis of APT data was completed using proximity histograms (called "proxigrams"; Hellman et al., 2000) made from isosurfaces of constant P concentration. Proxigrams essentially measure average concentration as a function of distance from the isosurface edge, akin to the pair correlation function for spatial point processes (Weeks et al., 2007). These were then compared between all other elements to determine the possibility of a correlation relation (Figure 4.3). This was all done using the built in isosurfaces and proxigram functions on IVAS 6.3.

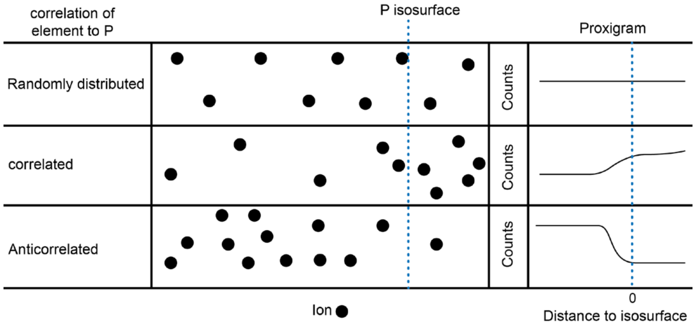

Figure 4.2: Proxigram demonstration, and how to interpret proxigrams. Proxigrams on right are heavily simplified. Ion can refer to ANY ion in the material, so long as it is referenced to isosurfaces (surfaces of constant concentration) of P. Note that inside isosurface, counting statistics get small, so error will increase.

To fully understand how phosphorus behaves within the structure of olivine, we must know its autocorrelation behavior. A point process is positively autocorrelated if points tend to exist near each other (in “clumps”), and negatively autocorrelated (or anticorrelated) if points are spaced out from each other. This can be used to determine if the charge balancing mechanism for P requires multiple units of P in a local area. Autocorrelation for P was calculated using both Moran’s I (Moran, 1954) (eq. 4.1) and Geary’s C (Geary, 1954) (eq. 4.2) in Matlab using a script that converts positional data into quadrat (here akin to a voxel) of 1 nm by 1 nm, and then applies the relevant statistical tests on each quadrat. The script creates a two-dimensional weight matrix (w) relating each cell (i) to each other cell (j), where w(ij)=1 if i is adjacent to j, and w(ij)=0 in all other cases (the rooks neighbors case). To avoid excessive memory use, the weight matrix was constructed cell by cell during calculation, determining all adjacent quadrats only when relevant. I, C values were then converted directly to a z-score to test for the statistical significance (p)

$$I = \frac{N}{W}\left(\frac{\left(\sum_{i=1}^{N}\sum_{j=1}^{N} w_{ij}(x_i - \bar{x})\left(x_j - \bar{x}\right)\right)}{\sum_{i=1}^{N}(x_i - \bar{x})^2}\right)$$

Equation 4.1: Calculation for Moran's I coefficient.

$$C = \frac{(N-1)\sum_{i=1}^{N}\sum_{j=1}^{N} w_{ij}(x_i - x_j)\text{^}2)}{2W\sum_{i=1}^{N}(x_i - \bar{x})^2}$$

Equation 4.2: Calculation for Geary's C coefficient

4.4.3 EPMA Results

Data points from 5 different rock samples and 303 separate points (primarily in profiles) were compiled. Elements were then plotted against each other to tease out correlation relationships. Each profile was stretched to show relative deviation in the elements within each crystal (Figure 4.3). Regressions show that the only universal correlation is with Si content. However, most of these points were taken from transects, in which case zoning is expected in Mg and Fe. Zoning may overprint the subtle

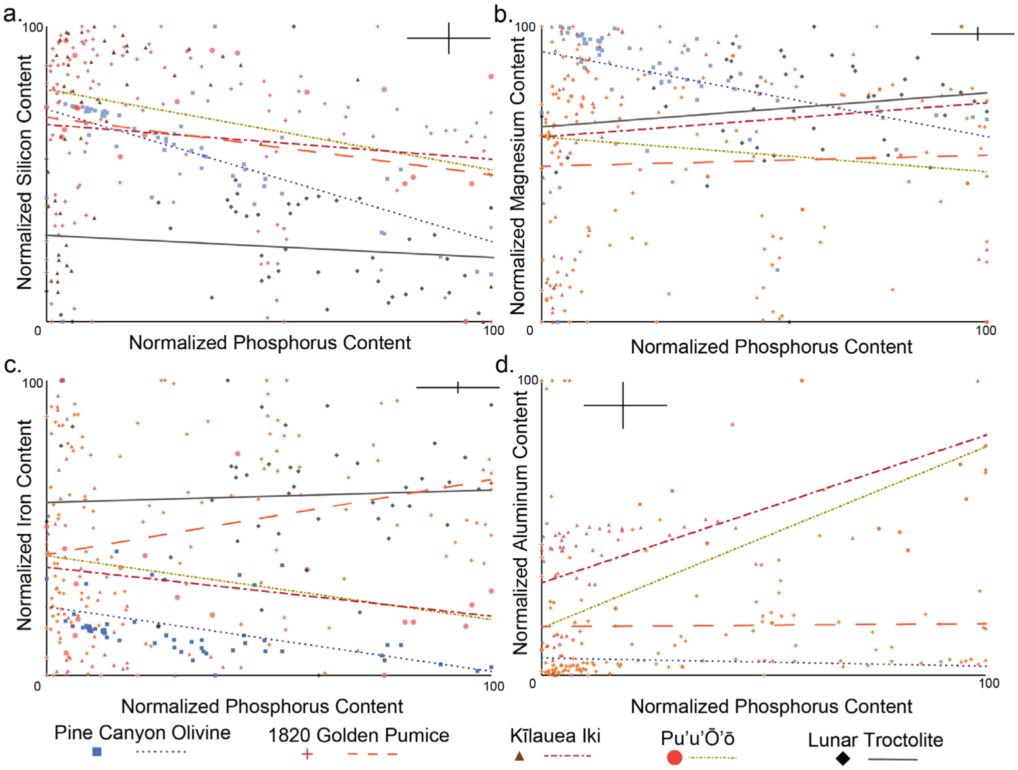

Figure 4.3: Compilation of EPMA data, normalized to highlight variations in each crystal separately. Linear regression trendlines are shown to highlight overall correlation relationships. Error crosses represent 2σ standard deviation. There exists a consistent anticorrelation in Si (a) in all samples. No other consistent correlation is present in EPMA data.

variations due to P heterogeneities. The EPMA approach is not capable of evaluating atomic-scale element substitutions. Much higher resolution analysis is required to avoid this problem.

4.4.2 TEM Results

EDS was able to characterize P enrichments in TEM foils from Pine Canyon (Figure 4.4). These lamellae can be <0.2 um in width. High-angle annular dark-field imaging (HAADF) intensity is roughly anti-correlated with this heterogeneity. This can imply a lower average atomic number in the region (Williams & Carter, 1996). P and Si are strongly anticorrelated (Figure 4.4 a,b) on

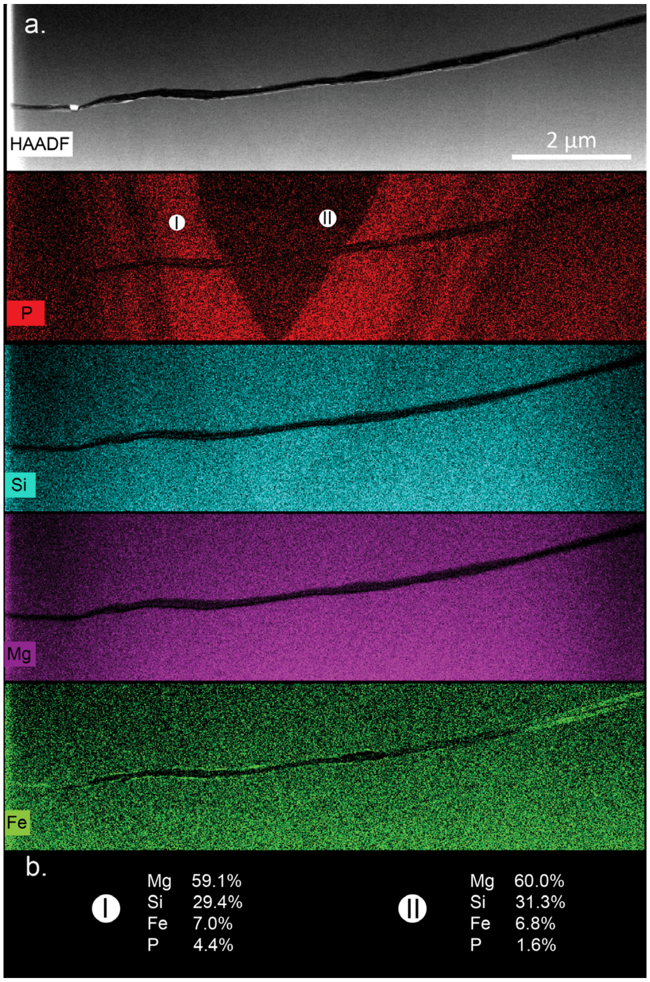

Figure 4.4 TEM EDS analysis of Pine Canyon olivine (Figure 4.1). Crystal is oriented along the a axis. a) HAADF image, and X-ray intensity maps of P, Si, Mg, and Fe. Note the anticorrelation of P with Si. This is emphasized in b) where two quantified points (marked in the P EDS map) are shown. Mg and Si decrease in P-rich zones.

the order of ~2 wt% Si. Note that these numbers are considerably more approximate (in fact they are normalized intensities) than the EPMA data and are most useful in analyzing relative variations of these elements.

TEM bright field imaging of the Pine Canyon olivine reveals a diffraction contrast along the boundary between P-rich and P-poor regions (Figure 4.5 b). However, no significant changes exist in diffraction patterns across the boundaries (Figure 4.5 c). HRTEM images show a brightness contrast, but the lattice itself is continuous between regions. Analysis of the Pu'u'ō'ō olivine also revealed no consistent change in diffraction patterns between P-rich and P-poor regions.

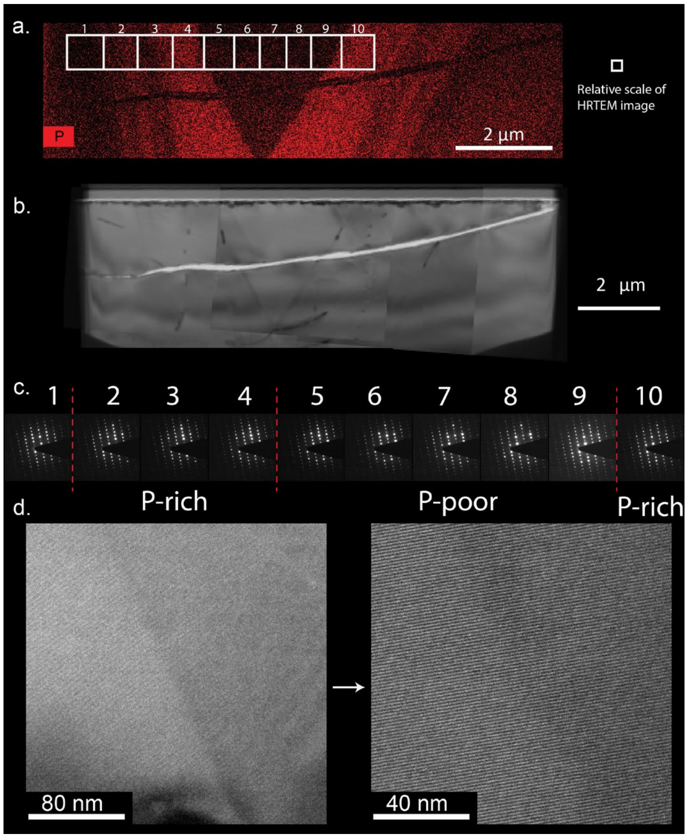

Figure 4.5: TEM imaging of Pine Canyon olivine. a) P EDS X-ray intensity map showing locations of lamellae. b) Bright field TEM image with objective aperture, shows contrast along the boundary of P rich zone. C) Diffraction patterns in zones marked in (a). No significant changes in diffraction patterns exist along boundaries between regions. d) HRTEM images of the boundary shows contrast but the lattice is continuous.

4.4.3 APT Results

4.4.2.1 Phosphorus characterization and lamella thickness

Phosphorus was above the APT detection limits in every sample. Even in samples without phosphorus enrichments, phosphorus was positively autocorrelated in every sample according to Moran's I and Geary's C (Table 4.1). One phosphorus-rich zone in the Pine Canyon olivine had unusual chemical characteristics and does not appear to be stoichiometric olivine (Figure 4.6). No lamellae were found in the olivine from Pu'u'ō'ō olivine. Given that this crystal was oriented on the b axis, it is possible the sample needles did not intercept lamella. However, lamellae on the order of 5-9 nm thick were present and abundant in olivine from both the Atlantis Massif olivine rich troctolite (Figure 4.6) and 1820 golden pumice (Figure 4.8).

	PCO	Pu'u'ō'ō	1820 GP	ORT
I	0.83	0.53	0.67	0.20
c	0.20	0.51	0.35	0.81
p	>0.99	>0.99	>0.99	>0.99

Table 4.1: Results of Moran's I and Geary's C autocorrelation tests. I is positive, and c is lower than one for all samples, meaning both show a positive autocorrelation. p is the significance of the test, where a p=0 means they are not significantly autocorrelated, and a p=1 means they are certainly autocorrelated.

4.4.2.2 Nanoscale Diffusion Dwell test

Golden Pumice olivine after 10 days dwell at 1400 °C was successfully characterized, with one needle intercepting two P heterogeneities. Lamellar P enrichments were ~ 5nm in width.

A sub nm scale version of the diffusion models in section 3.3.6 was made to evaluate the survivability of such fine-scale lamella with time. If a one atom thick 100% wt% P lamella is held at 1400 °C for 10 days, it should homogenize over the length of the needle beyond the detection limit of APT (Max P in lamella – min P in lamella < 1 σ standard deviation) at 1400 °C in << 1 hour using the diffusivity of P and 5 hours using the diffusivity of silicon.

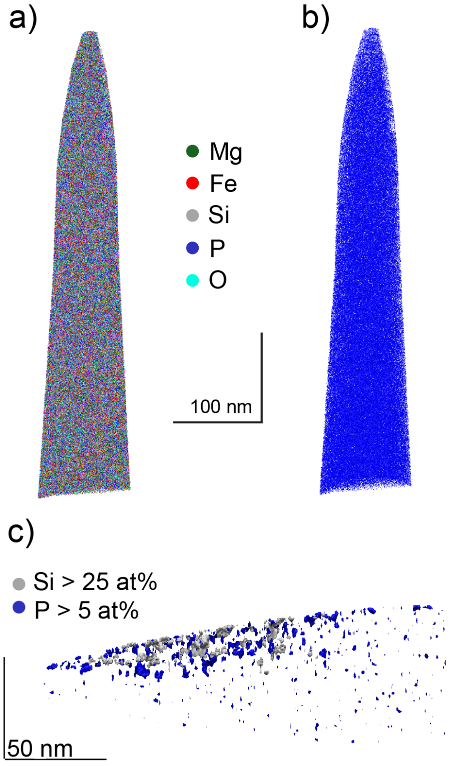

Figure 4.6: APT analysis of the Pine Canyon Olivine. a) APT point cloud of all ions. b) Point cloud of only P ions. c) Isosurfaces (Surfaces of constant concentration) of P and Si at the tip of the needle showing an unusual high-Si phase.

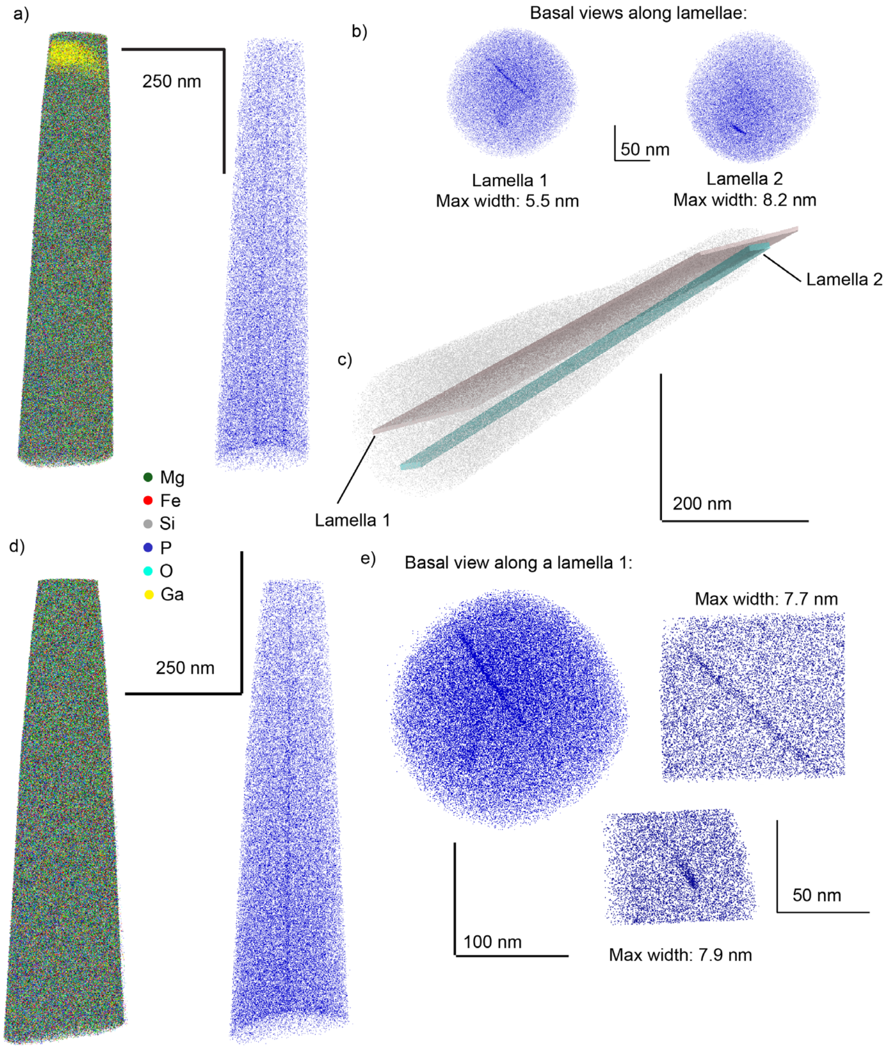

Figure 4.7: APT analysis of the Atlantis Massif olivine rich troctolite. a) Ion point clouds of the first needle. Yellow streak is implanted gallium from the FIB. Note two lamellae of P in P Ion point cloud. b) Basal projections (ion point cloud rotated to view down the long axis of the lamella) of P Ion point clouds from (a). c) Lamellae from (b) highlighted by boxes overlaid on ionic point cloud of Si ions. Neither lamella is parallel with the axis of the needle. They are also slightly subparallel to each other. d) Ion point clouds of the second needle. e) Basal view of the ion cloud, accompanied by insets to highlight them.

4.4.2.3 Elemental correlations

Proxigrams (section 4.3.5) were made on decomposed ions using all needles. In every single needle, P is anticorrelated with both Si and Mg (Figure 4.9). The effect is

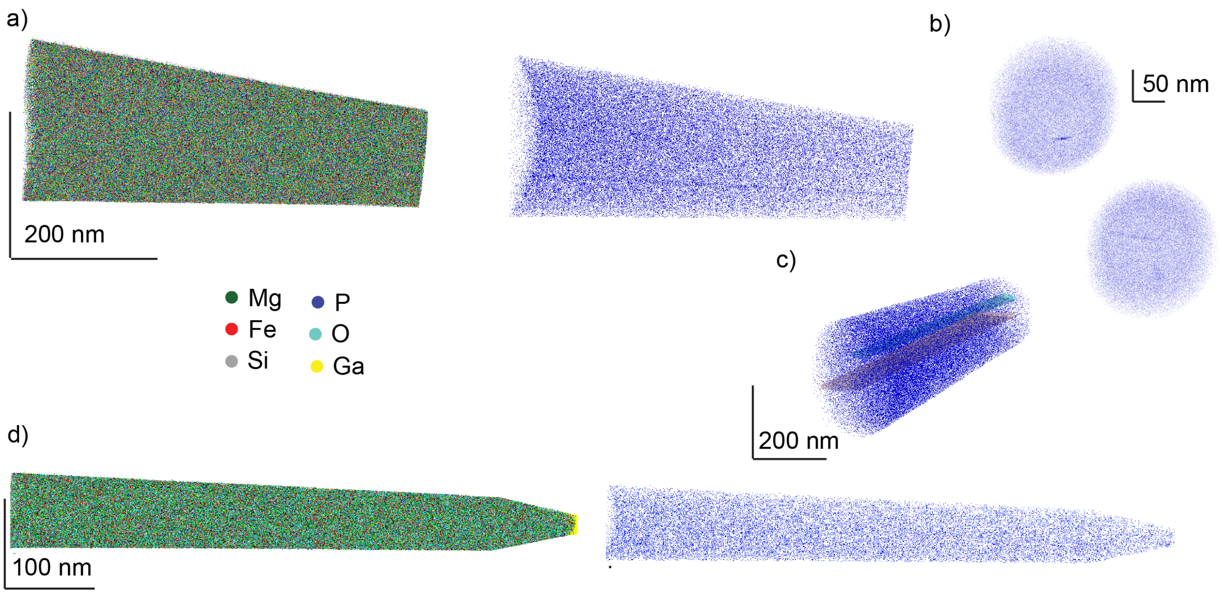

Figure 4.8: Golden Pumice APT data. a) Ion point clouds for the first needle, showing two lamellae. b) Basal views along each lamella. Top lamella is 7.54 nm thick, and bottom lamella is 7.53 nm thick. C) Highlighted lamellae over point cloud. Though they are more parallel than the ORT, two lamellae are subparallel planes.

local to edges of the high phosphorus regions. No other elements show universal correlation relationships with phosphorus in all samples. Fe sometimes shows anticorrelation behaviors with P, but not universally, and to a lesser extent than Mg. In no sample was a correlation between Li or Al found with P. No other universal correlation behavior was found (Figure C-3).

4.5 Discussion

4.5.1 Implications of Ultrathin Lamellae

Lamellar enrichments of phosphorus that are thinner than 10 nm were discovered in both the experimentally reheated 1820 golden pumice olivine and the Atlantis Massif olivine rich troctolite (Figures 4.7, 4.8). Heterogeneities of this length

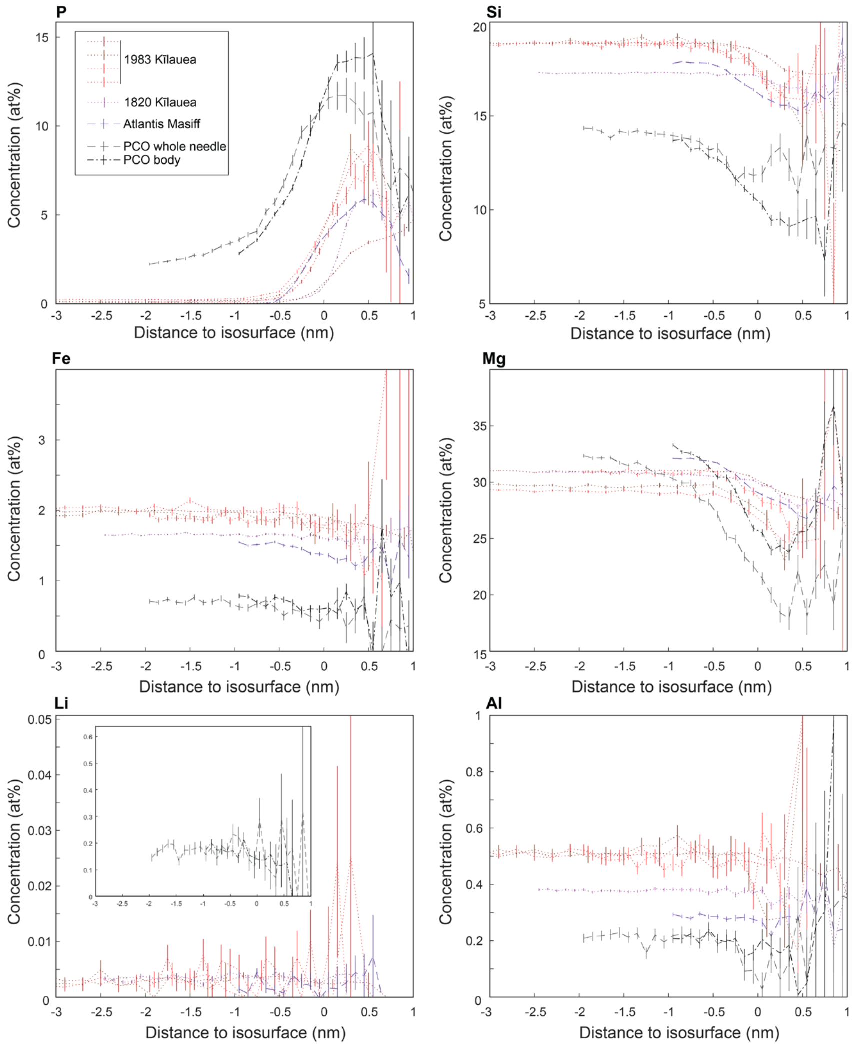

Figure 4.9: Proxigram analysis of APT samples. Concentration is plotted relative to distance to surface of constant P content (isosurface), with positive numbers inside the isosurface, negative numbers outside of the surface. Error bars are 2σ, but should be considered only relative error, as this doesn't take into account error introduced from ranging the data.

scale were not anticipated. Atlantis Massif olivine was chosen specifically to study how diffuse phosphorus enrichments present at the nanoscale. However, this "diffusively relaxed" phosphorus-enriched area are, in fact, a series of tightly packed nm scale lamellae distributed through the crystal. Diffusion modeling shows that even a one-atom thick phosphorus lamella, the enrichment would diffusively homogenize (and not be detectable with APT) if P were as mobile as other tetrahedrally site elements (Dohmen, 2002; Watson et al., 2015). Combined with the results of Chapter 3, this suggests lamellar phosphorus enrichments are effectively immobile in olivine.

These features could be explained by three hypotheses:

1. The lamellae are actually subgrain boundaries enriched in P
2. The lamellae are intergrowths of a phase similar to olivine, but able to carry high concentrations of P
3. These lamellar P enrichments are continuous with the surrounding olivine lattice, but these P enrichments are immobile.

Hypothesis 1 is supported by similar length-scales of P enrichments along olivine-olivine grain boundaries in olivine (Cukjati et al., 2019). Subgrain boundaries could accept incompatible elements, such as P from olivine's structure. Welsch et al. (2013) suggests that subgrain boundaries could be produced during rapid dendritic crystallization of olivine. This could also explain the lack of diffusive relaxation of these lamellae (Chapter 3) as well as slow diffusion of Li when associated with P (Lynn et al. 2020). However, there is a lack of any other element showing any relation to these zones in any data set (Figure C.3). This is at odds with other studies, which present a wide array of elemental heterogeneities associated with olivine-olivine grain boundaries (Cukjati et al., 2019; Tacchetto et al., 2021). Also, there exists no evidence of diffraction patterns varying near P rich areas (Figure 4.5), or variation in EBSD patterns around P rich zones (Figure A-7).

Hypothesis 2 would posit an entirely separate phase existing inside olivine crystals. This would be analogous to nm scale clinohumite lamellae in olivine (Wirth et al., 2001). If phosphorus was significantly more compatible in the included phase, the equilibrium concentration could enforce a sharp boundary. However, HRTEM images lack evidence of lattice distortions or mismatches, and as with hypothesis 1, there is no change in diffraction patterns. So, this phase would have to have an extremely similar structure to olivine, and its composition would have to be approximately the same, making it difficult to distinguish from a chemical heterogeneity in olivine.

Hypothesis 3 is therefore the most consistent with our observations. This hypothesis posits that P is directly incorporated into the lattice of olivine. P incorporation into the lattice of olivine requires an appropriate charge balancing mechanism for P in olivine that leaves no vacancies in the tetrahedral site to be consistent with our findings. Given a sufficiently small number of tetrahedral vacancies, diffusive relaxation would slow to a standstill, as diffusivity is largely controlled by the number of available site vacancies (Chakraborty, 2008; Nakamura & Schmalzried, 1983). Thus, removing all vacancies would increase the activation energy of diffusion to a degree that diffusion effectively stops.

4.5.2 Phosphorus incorporation in olivine

The accommodation mechanism for phosphorus in olivine has been the focus of debate, as it has direct implications on the diffusive behavior of the element (Section 3.5.1). As in chapter 3, we assume that P must be incorporated into the tetrahedral (tet) site in olivine. This is also enforced by the results of this study; these lamellae are sharp to a degree that is incompatible with the relatively rapid diffusion typical of the octahedral (oct) sites. The data presented here allows us to significantly narrow down the list of possible accommodation mechanisms for olivine (Figure 3.4, Equation 4.3).

a) $2Mg_{oct}^{x} + Si_{tet}^{x} + 4O_{O}^{x}=$

b) $Mg_{oct}^{x} + \square_{oct}^{\prime\prime} + X_{i}^{\bullet} + P_{tet}^{\bullet} + 4O_{O}^{x}$

c) $2Mg_{oct}^{x} + X_{i}^{\prime} + P_{tet}^{\bullet} + 4O_{O}^{x}$

d) $4Mg_{oct}^{x} + X_{tet}^{\prime} + P_{tet}^{\bullet} + 8O_{O}^{x}$

e) $Mg_{oct}^{x} + X_{oct}^{\prime} + P_{tet}^{\bullet} + 4O_{O}^{x}$

f) $10Mg_{oct}^{x} + 4P_{tet}^{\bullet} + \square_{tet}^{\prime\prime\prime\prime} + 20O_{O}^{x}$

g) $3Mg_{oct}^{x} + \square_{oct}^{\prime\prime} + 2P_{tet}^{\bullet} + 8O_{o}^{x}$

Equation 4.3: Charge balancing mechanisms for P in olivine using Kröger-Vink (KV) notation (Section 1.4; ● is a +1 charge defect, and ′ is a -1 charge defect). X can stand for a variety of elements that would provide the appropriate charge defect in the site indicated. (a) A normal unit of olivine, all substitutions must maintain charge balance with this.

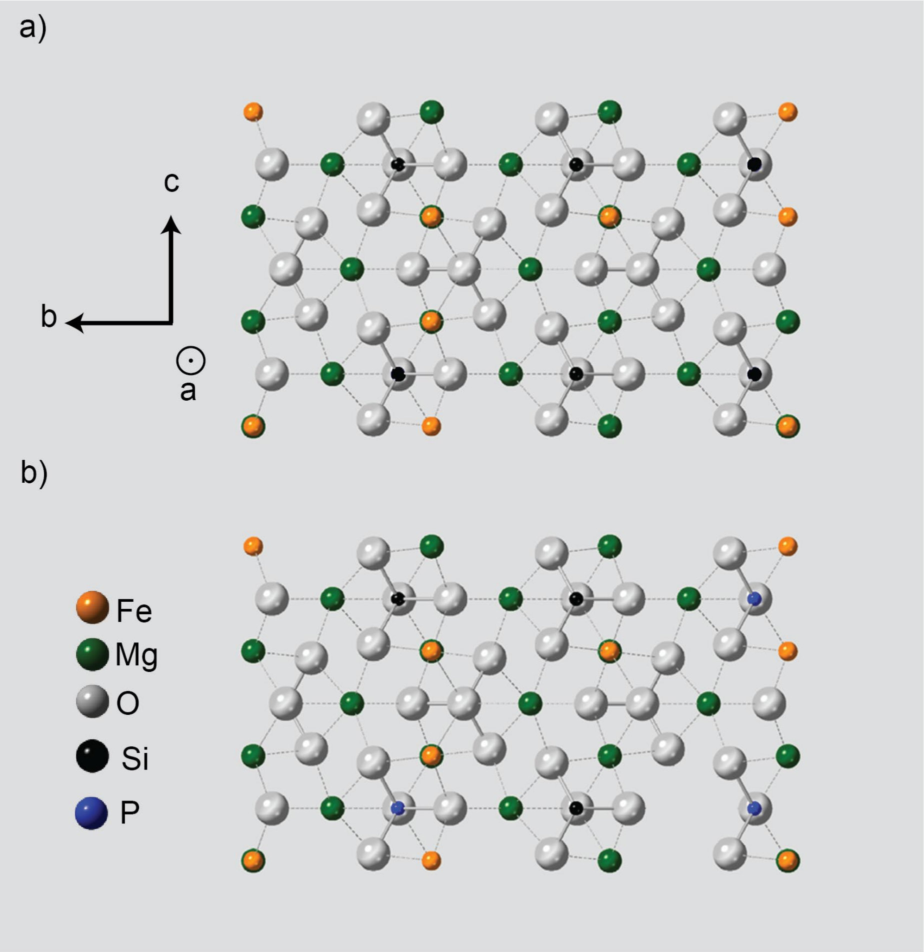

Figure 4.10: Our proposal for charge balancing P in olivine a) Fo 75 olivine, b) Fo 75 olivine with 10% phosphorus, with 1 Mg vacancy per 2 phosphorus atoms.

Although any of these charge mechanisms (and similar ones) undoubtedly occur in specific cases (Grützner et al., 2017; Lynn et al., 2020; Moreau et al., 2010; Shea et al., 2019; Walker et al., 2003), a general mechanism for charge balancing P in olivine is desirable, if it exists. Our EPMA, TEM and APT data all agree that the only consistent correlation relationships with phosphorus in olivine across all samples is with Si and Mg. This means that mechanisms b,c,d and e from Equation 4.3 are unlikely, as if these were true, there would exist a 1:1 molar ratio of X (consisting of H, Li, Na, Al, or Fe) to

P, and be detectable by all three instruments. Further, P showed strong autocorrelation (Table 4.1, Figure 4.9) in all samples, even away from lamellae. This would be most consistent with mechanisms f or g, as both mechanisms require multiple units of P local to eachother for charge balancing (Equation 4.3). Finally, the sharpness of the lamellae and lack of observable diffusive relaxation of these lamellae (Chapter 3) imply that the mechanism should not provide or create tetrahedral vacancies (Chakraborty, 2008; Nakamura & Schmalzried, 1983). Also, mechanism f does not explain the anticorrelation of Mg with P. So, we posit that the general mechanism for phosphorus incorporation in olivine is via octahedral site vacancies (Equation 4.3 g, Figure 4.10).

4.6 Conclusions

Olivine from a diverse array of materials have been studied to understand the length scale of P-rich lamellae and how P is incorporated. This was done using EPMA, TEM, and APT. APT analysis of intragrain chemical heterogeneities (especially of trace elements) has not been conducted before, and we demonstrate that APT is suitable for fine scaled heterogeneities such as this. We found that P-rich lamellae can be extremely fine scale – down to 5 nm wide. These lamellae show no consistent structural change from the bulk olivine. We find that phosphorus is universally autocorrelated and tends to be anticorrelated with Mg and Si. We therefore posit that these lamellae are enrichments of P occupying the tetrahedral sites hosted by octahedral site vacancies, and an absence of tetrahedral site vacancies prohibits diffusive relaxation on these samples.

Chapter 5: Relative cooling histories of Type I PO and BO chondrules

In preparation as: Nelson W., Hammer J., Libourel G., and Shea T. *Relative cooling timescales of type I porphyritic and barred chondrules using trace element diffusion chronometry*

5.1 Abstract

Chondrules comprise one of the few records we possess of the protoplanetary disk. Two of the most common textural types of chondrules, barred and porphyritic olivine chondrules, are chemically identical but have very different morphologies. Hypotheses that explain these textural differences invoke either chemical supersaturation driven by interactions with the protoplanetary disk gas or variable degrees of undercooling causing homogeneous nucleation, and thus rapid crystallization textures. Here, we evaluate these hypotheses by finding relative cooling timescales between these two classes of chondrules using diffusion chronometry. We find that barred and porphyritic chondrules underwent similar degrees of diffusive relaxation, implying that they have experienced similar thermal histories. Therefore, we argue that type I chondrule textural variety is largely controlled by interactions with the protoplanetary disk gases rather than cooling rate or timescales.

5.2 Introduction

Chondrules are among our first records of solar system materials. They are sub cm spherules of silicates, metals and sulfides that make up a primary component of chondritic meteorites. Chondrules are classified using a dual textural and compositional scheme. Texturally, the most common chondrules are porphyritic olivine (PO), porphyritic olivine plus pyroxene (POP), porphyritic pyroxene (PP), and barred olivine (BO). Compositionally, chondrules are split into two broad categories: reduced (type I), and oxidized (type II). These are typically identified by tracking Fo (Chapter 1.1) and En ($=Mg/(Mg+Fe^{2+}+Ca)*100$) in olivine and pyroxene respectively. Type II chondrules have Fo and En between 10 and 90%, and type I have Fo and En >90% (typically closer to 100%). These types can then be further split into categories A (Si undersaturated, ol-rich) and B (Si saturated, pyx-rich; Russell et al., 2018; Connolly and Jones, 2016).

These classes are observational rather than genetic. As such, there is disagreement over the causes of these textural and chemical distinctions. For example, the cause of the BO vs PO textural divide is still under debate, despite the ubiquity of these chondrules. Barred olivine is generally considered to result from rapid crystallization (Donaldson, 1976; Faure et al., 2003). Crystallization rates varying to this degree in chemically similar parts of the protoplanetary disk requires an explanation.

The first and most obvious explanation is that the BO chondrules experienced a more rapid cooling history than the PO chondrules. However, experiments fail to reproduce barred olivine textures by modifying the cooling rate alone (Auxerre et al., 2022). Also, there are strong limits on just how slowly PO chondrules could cool without a loss of their volatile elements (Hewins et al., 2005; Connolly and Jones, 2016).

The second explanation utilizes another way to accelerate crystallization rates in BO chondrules. In the absence of abundant nucleation sites, crystallization can be suppressed until lower temperatures are reached. The temperature difference between a mineral-in temperature and the temperature conditions imposed during crystallization is called "undercooling" (Faure et al., 2003), and is the driving force for crystallization. It has been shown experimentally that identical silicate melts can produce PO and BO textures given the presence or absence of preexisting substrates for nucleation (Tsuchiyama et al., 2004). To accomplish this in chondrules, it is commonly thought that the solid precursors to chondrules could be heated to variable degrees, resulting in some droplets that are entirely molten, and some that have remnant grains serving as growth substrates. The droplets lacking growth substrates form BO chondrules (Lofgren and Lanier, 1990), and ones with ample nuclei crystallize more slowly, forming PO chondrules (Hewins, 1983, Figure 5.1 a). This hypothesis also typically invokes differing cooling rates, as this leads to the most accurate recreation of chondrule textures (Tsuchiyama et al, 2004; Connolly and Jones, 2016; Russell et al., 2018 ;Libourel & Portail, 2018).

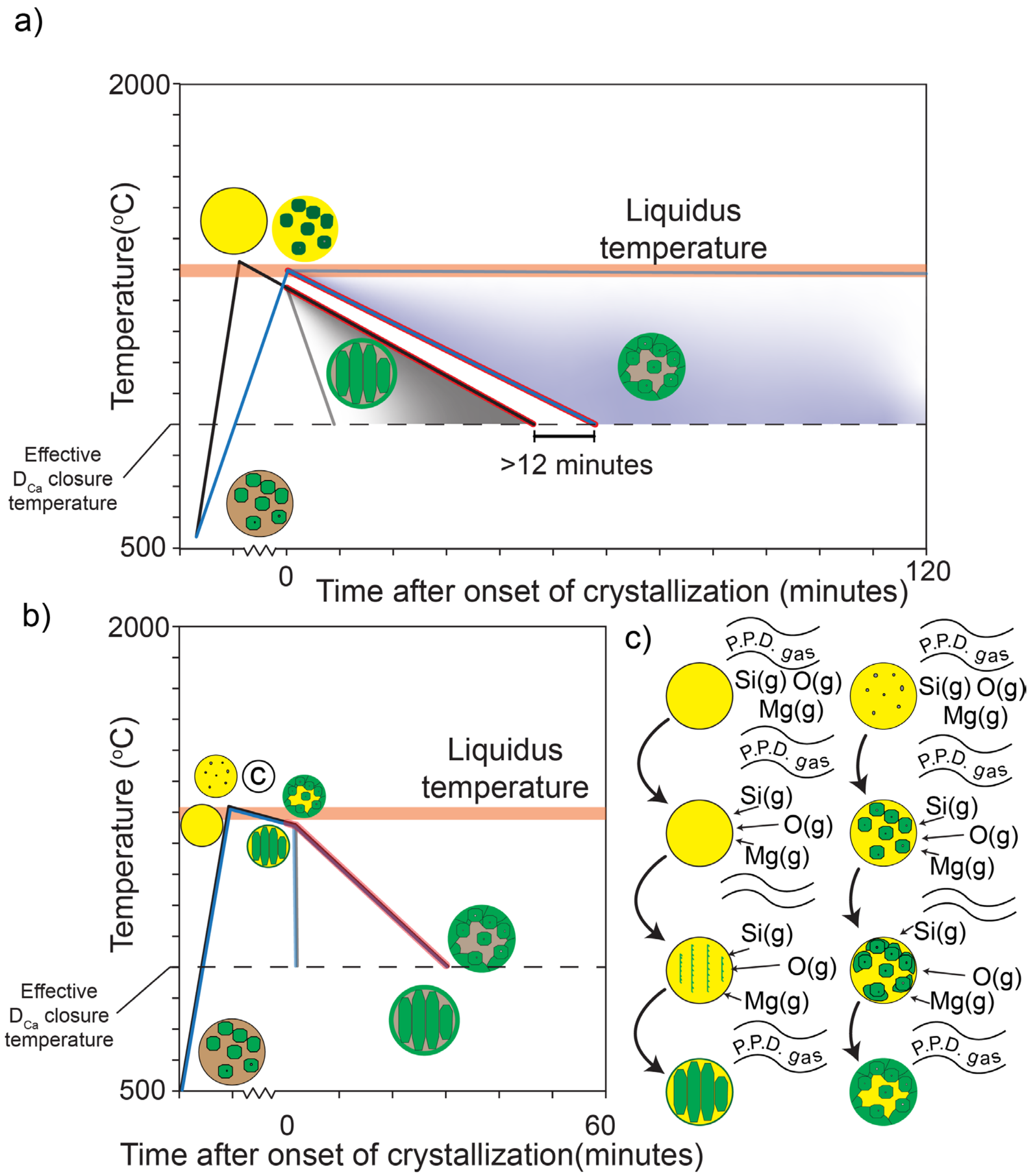

Figure 5.1: Possible thermal histories of PO and BO chondrules. a) thermal model path. Shaded regions show the range of formation times. Time = 0 is set to be at the onset of crystallization. b) Saturation model path. Red highlight marks regions that would be recorded by olivine. Faint lines show the fastest proposed timescale. c) Cartoon demonstrating how the saturation model works. c takes place during the short portion of the high T path highlighted in b, where Si, O, and Mg is ingassed from the protoplanetary disk (P.P.D.) gas.

Finally, a third explanation uses not thermal, but chemical changes to control nucleation style. This hypothesis proposes that an initially refractory melt composition that receives Mg, Si and O from the surrounding gas. In this case, BO and PO chondrules have nearly identical thermal histories, but the presence of nucleation sites in PO chondrules means that nucleation can take place at a lower degree of olivine supersaturation (Libourel & Portail, 2018). Homogeneous nucleation will only take place after a high degree of olivine supersaturation, forming BO chondrules (Figure 5.1 c).

These hypotheses vary in one key way: their thermal histories (Red highlighted portions of Figure 5.1 a,b). In the example in 5.1a, we assume a liquidus temperature of 1400 °C, and 50 °C undercooling to form barred olivine morphologies (Faure et al., 2003). Choosing the fastest cooling rate proposed for PO chondrules, and the slowest cooling rate proposed for BO chondrules, there still exists a 12-minute gap in time, which only gets longer with more moderate choices of slope (shaded regions). Though small, a difference of 12 minutes can lead to a large shift in degrees of diffusive relaxation at high temperature. If we can determine relative high temperature cooling timescales through analysis of samples and application of diffusion chronometry, this conflict will be resolved. Therefore, we propose a null hypothesis to be tested:

H_0: BO and PO chondrules have different ($\Delta t>10$ minutes) thermal histories.

If undercooling is responsible for the textural difference, we should be able to accept the null hypothesis, while if olivine supersaturation is responsible, we will reject the null hypothesis. This postulate assumes that it is possible to characterize the thermal histories of PO and BO chondrules. PO and BO chondrules only have three phases: Glass, olivine, and metal, meaning that most petrological methods for determining thermal histories are obscured (Putirka, 2008). Further, the timescales of chondrule formation are proposed to be less than a day, implying the relevant cooling history is highly nonlinear.

However, a variety of highly consistent intragrain chemical heterogeneities have been documented in both PO and BO olivine (Libourel & Portail, 2018; Marrocchi et al., 2019; Piralla et al., 2021). These have been interpreted to reflect interactions with gases from the protoplanetary disk (Libourel & Portail, 2018). These heterogeneities can be used to evaluate high temperature thermal histories using the method of diffusion chronometry (Section 1.3). Should one class of chondrules have experienced a longer thermal history, we expect heterogeneities in the chondrule to have diffusively relaxed to a greater extent.

The relative degrees of diffusive relaxation in PO and BO chondrules can be quantified using diffusion chronometry. A numerical model of diffusive relaxation applied to several PO and BO chondrules can address the null hypothesis.

5.3 Methods

5.3.1 Materials

For diffusion modeling to accurately reflect only the primary crystallization history, we had to significantly restrict what chondrites from which we could use chondrules. We wish to avoid hydrothermal alteration or reheating of chondritic material. So, we limit chondrites of interest to types 2-4 (minimally hydrothermally altered and minimally metamorphosed). Each chondrite slide must also have both a PO and a BO chondrule. Of these, we analyzed three meteorites: 1) Acfer 094, an 82 g type 2 CO – CM carbonaceous chondrite found in Algeria (Wlotzka, 1991); 2) Semarkona, a 691 g type 3.0 LL ordinary chondrite fall from India (Grossman & Brearley, 2005); 3) Yamato 81020, a 270 g type 3.0 CO carbonaceous chondrite found in Antarctica (Graham, 1985). One PO and one Bo chondrule was selected from each chondrite and analyzed.

5.3.2 Analytical methods

Chondrule characterization was carried out with the JEOL JXA-8500F field emission electron microprobe at the University of Hawai'i at Mānoa. Our analysis involved the initial characterization of chondrules with x-ray intensity maps, which guided analytical profiles.

X-ray intensity maps were acquired using nearly the same conditions as described in Chapter 4. Some Ti, Cr, and Mn maps were collected at 15 kV, but due to the small scale of BO chondrules, a 5 kV accelerating voltage was required for most grains. Therefore, all grains were mapped for Al, Ca, and Mg.

Quantitative transects of Mg, Fe, Si, Al, Cr, Mn, Fe, and Ti were collected using a 15 kV accelerating voltage, a 300 nA beam current, and a focused beam. An on-peak time of 280 ms was used for Al and Ca; 200 ms for Mn; 150 ms for Mn, Fe, and Ti; and 30 ms for Mg and Si. The background was modeled using an exponential fit. Due to the extremely forsteritic (> Fo 99) composition of these olivine crystals, a synthetic Caltech Mg olivine was used as a Mg and Si standard. A synthetic Mn olivine from the same block was used to standardize Mn. Springwater olivine (USNM 2566) was used for Fe. Plagioclase from Lake County (USNM 115900) was the standard used for Ca and Al. A chromite (USNM 117075) was used to standardize Cr. A99 glass and San Carlos olivine standards were analyzed as unknowns to track any drift and evaluate analytical accuracy.

5.3.3 Diffusion chronometry

Diffusive relaxation of chemical heterogeneities was modeled through a numerical solution of Fick’s second law using midpoint finite differences (Section 1.3.2). Modeling was completed in Matlab R2022b.

5.3.2.1 Diffusion coefficients

For Ca, the modified diffusion coefficients for extremely forsteritic compositions were used (Coogan et al., 2005). For Cr, the diffusion coefficients reported by Ito & Ganguly (2006) were applied. Finally, Mn was modeled using the interdiffusivity of Mg-Fe (Dohmen & Chakraborty, 2007). This was done because previous studies have found that Mn diffuses at a similar rate to Mg-Fe interdiffusion (Petry et al., 2004), and Mn occupies vacancies in the same sites as Mg/Fe (Chakraborty, 2008, 2010). Calculated diffusivities in this chapter depend on additional variables. This includes pressure, for which we used P= 50 ± 50 Pa (Galy et al., 2000). Oxygen fugacity has been calculated from CPX+melilite pairs found in inclusions to be log (fO2 (atm)) = -19.8±0.9 assuming similar temperatures assumed in this study(Grossman et al., 2008).

Getting an appropriate temperature term, which dominates the diffusivity, is difficult in this scenario. Use of any previously proposed thermal paths will bias the results. Here, we take advantage of our statement of the null hypothesis. Rejecting it does not require that we constrain an absolute time. Given the large uncertainties in pressure and oxygen fugacity, the problem is simplified by not pursuing absolute timescales, instead focusing on relative timescales. Therefore, we choose a simple isothermal (1600 °C/1873 K) modeling condition, though the temperature is arbitrary, we choose this temperature as the approximate mean of the liquidus temperatures discussed in Libourel and Portain (2018). So long as all diffusivity variables are held constant between the PO and BO chondrules, the high diffusivity this isothermal model creates does not affect our desired output variable: relative timescales.

5.3.2.2 Initial conditions

Incomplete knowledge of the initial conditions remains one of the principal sources of error in diffusion chronometry, as determining the spatial distributions and concentrations of each heterogeneity at the moment of crystallization is complex. The problem is especially acute here, as there appears to be complex layering of dissolution and recrystallization in these samples (Libourel & Portail, 2018). Therefore, it is particularly important to establish whether gradients are from crystal growth or diffusive relaxation.

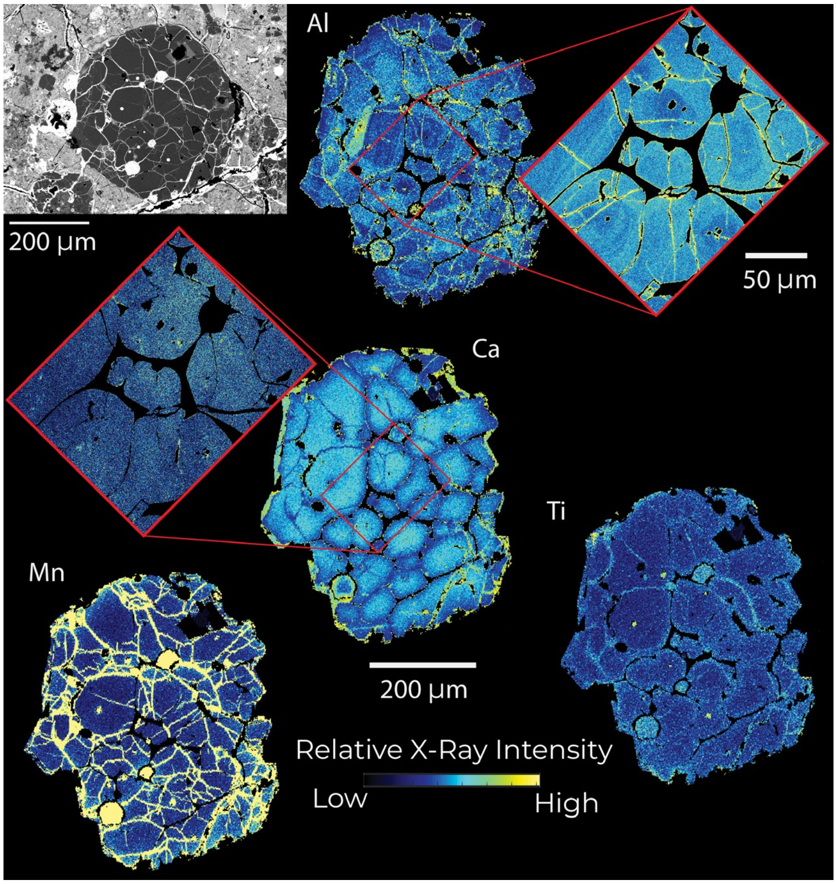

Figure 5.2: EPMA X-ray maps of PO chondrule in Acfer 094. BSE context image in the top left.

There is a consistent behavior between all compositional heterogeneities: Al and Ti are arrayed in sharp oscillatory enrichments that are coincident with CL brightness (Libourel & Portail, 2018, Figure 5.2, 5.3). Ca, Mn, and Cr are more diffuse (Figure 5.2, 5.3). Given the relatively low diffusivities of Al and Ti, we interpret Al and Ti enrichments as comparatively well-preserved signatures of crystal growth. Therefore, if we obtain initial conditions for modeling based on Al profiles, we should only be testing diffusive relaxation of chemical heterogeneities (Shea et al., 2015). Al profiles are stretched by subtracting the minimum aluminum content on the profile from each point, adding the minimum of the Ca (or Mn or Cr for those models) content, and then multiplying by a scaling factor. We then iteratively run diffusion models changing the scaling factor to locate the minimum RMSD at completion of each model. This same tactic was used where possible on Mn and Cr profiles, but frequently, they could not be appropriately fit using a stretched or even inverted Al profile. In this case, marked changes in Al content were designated as crystallization boundaries, and initial conditions were only modified along these boundaries.

5.4 Results

Diffusive timescales were calculated in 1D for Ca, Mn, and Cr in PO and BO chondrules from sections from Acfer 094, Semarkona, and Yamato 81020. We report only relative timescales, as there are large uncertainties related to diffusivities of all elements in these samples, as well as recent uncertainties in overall diffusivity behaviors (Chapter 3; Shea et al., 2023). Ca timescales were consistently the shortest, always less than an hour, while Mn and Cr timescales were often longer, on the scale of 1-3 hours, but were in good agreement with each other. Relative timescales are universally small <5 minutes (Tables 5.1, 5.2, 5.3). In all cases, PO timescales were longer than BO timescales.

Ca	Acfer 094	Semarkona	Yamato 81020
Δt (Minutes)	3.3	3.8	2.1
σ (Minutes)	3.5	4.4	10.1

Table 5.1: Results of Ca diffusion chronometry. Δt = the difference between diffusive timescales of PO and BO chondrules. The error only includes terms that are relevant to relative diffusive timescales. Absolute timescales will have orders of magnitude more error due to uncertainties in P, T and fO2. Note that the high error on Yamato 81020 is due to the low number of points for the diffusion model due to the extremely small size of the BO crystals.

Mn	Acfer 094	Semarkona	Yamato 81020
Δt (Minutes)	2.5	2.0	0.2
σ (Minutes)	0.8	0.5	10.5

Table 5.2: Results of Mn diffusion chronometry.

Cr	Acfer 094	Semarkona	Yamato 81020
Δt (Minutes)	2.0	2.7	0.2
σ (Minutes)	0.9	1.5	10.5

Table 5.3: Results of Cr diffusion chronometry.

5.5 Discussion

Consistently, while Ca initial conditions could be reconstructed from Al heterogeneities, Mn and Cr frequently could not be. The relatively longer Mn and Cr timescales imply that Mn and Cr are less controlled for diffusion vs. growth than Ca and should be treated with more skepticism. This also brings up the question as to why Mn and Cr behave differently than Al, Ti, and Ca. Cr and Mn are many orders of magnitude more compatible in olivine than Ca, Al, and Ti (Colson et al., 1988; Dunn, 1987; Leeman & Scheidegger, 1977; Nikogosyan & Sobolev, 1997), meaning that Mn and Cr should not accumulate in the melt relative to Al, Ti and Ca. So, the puzzling dichotomy of heterogeneity distributions could occur due to two things: 1) Mn and Cr could, at relevant fO_2 conditions, preferably partition into metallic Fe in chondrules. Typically, Mn and Cr have lowest concentrations at the cores of grains (especially in barred chondrules), with much simpler profiles. This is consistent with this hypothesis, as early in the crystallization history, Mn and Cr partition into the metal bleb, but as the bleb is mantled by olivine, Mn and Cr would start to accumulate in the melt, roughly creating the profiles we observed. 2) The variation of Mn+Cr vs. Al+Ti+Ca could also occur at the gas/melt interface. If this is the case, it would imply the two elemental fluxes are untethered, and there is a relatively more stable, increasing flux of Mn, Cr across the melt boundary when compared to the fluctuation of Al, Ti and Ca.

We can, to a degree, reject the null hypothesis. Time differences are detectable, but universally less than five minutes. So chondrule formation mechanisms should explain BO and PO chondrules having relatively similar subliquidus thermal histories. The supersaturation theory is more consistent with these findings. The small difference in timescales could be because the supersaturation model has BO chondrules form after a delay relative to PO chondrules at high T to reach olivine supersaturation. Even small amounts of time at high temperature should have a relatively large effect on diffusive timescales, and we would expect PO olivine to yield longer timescales.

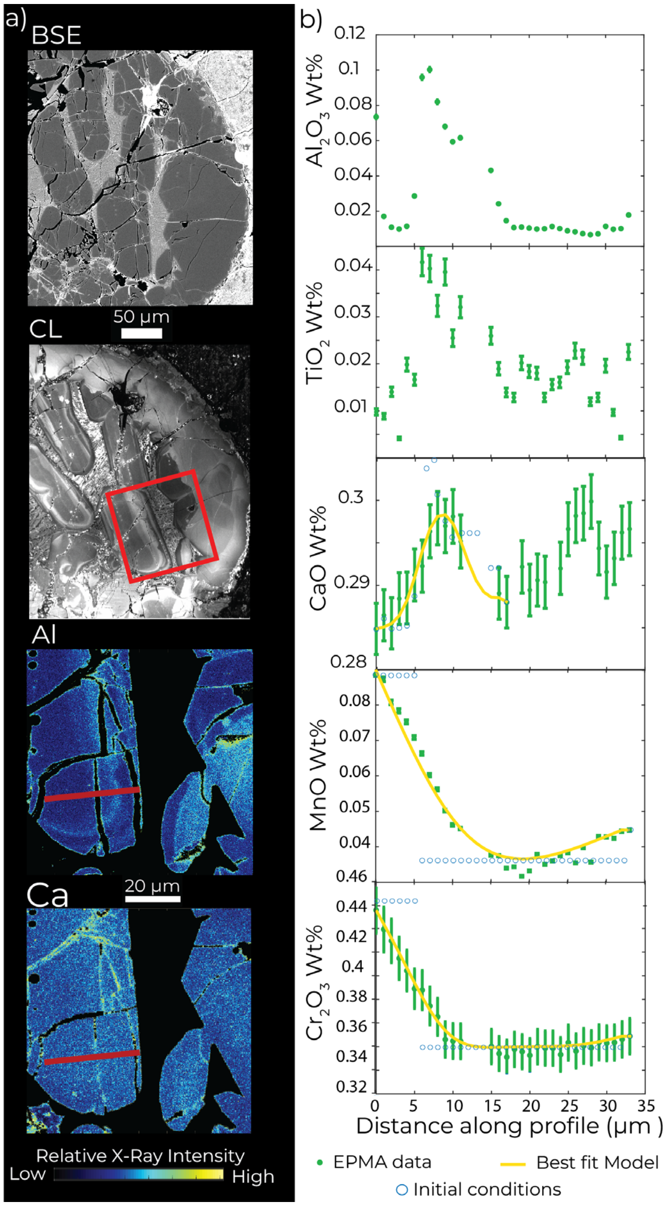

Figure 5.3: BO chondrule in Acfer 094. A) BSE images, cathodoluminescence data, and EPMA maps. B) Models and best fits line taken from profiles in (a).

A question that this method is less capable of addressing is what would serve as the growth substrates in PO chondrules. Marrocchi et al. (2019) suggest the cores of PO chondrules are relict grains of the original "dustballs" that melted to form chondrules. We observe a relatively chemically homogeneous core to many PO olivine grains, which would be consistent with this hypothesis. The main shortcoming of this hypothesis is explaining why some chondrules contain relict grains, and others don't given the similarity in recorded magmatic timescales. Libourel & Portail (2018) propose that this paradox could be reconciled by the presence of metal blebs serving as nucleation sites. The metal bleb theory is consistent with observations that PO chondrules typically have Fe metal blebs as inclusions, while BO chondrules do not (Figures 5.2, 5.3, Libourel & Portail, 2018). However, it has yet to be shown that a liquid metal: silicate liquid interface can serve as a nucleation site for olivine. Our results could be consistent with either hypothesis. Our results are most compatible with the metal bleb hypothesis, assuming that liquid metal can act as a nucleation site. Relict grains could also be consistent with our observations, given that their presence or absence isn't based on variable max heating temperatures or cooling rates. If relict olivine preservation is due to the melted dust balls having variable olivine saturation or superliquidus dwell times, this hypothesis is consistent with our results.

5.6 Conclusions

In this chapter, we demonstrated an application of diffusion chronometry that only relies on relative timescales, making it resistant to errors or uncertainties in the diffusivities of the elements in olivine. We explored the relative thermal histories of BO and PO chondrules using profiles of Ca, Mn, and Cr. We found that relative diffusive timescales were consistently shorter than in the traditional undercooling model of BO formation. Therefore, olivine supersaturation is likely responsible for the PO/BO morphological distinction.

Chapter 6: Conclusions

6.1 Summary

Chemical heterogeneities in olivine can be used as a powerful tool to uncover the high-temperature histories of olivine-bearing rocks. In the dissertation, we have explored the high-temperature history of a lunar sample, recognized a potential issue with a diffusive system in olivine, demonstrated the issue in laboratory conditions, addressed the cause, and demonstrated a simple way to analyze systems that is resistant to uncertainties with diffusivities, using multiple heterogeneities in the same sample to strengthen calculations.

Chapter 2 examines the cooling history of lunar troctolite 76535. This highlands sample has a few unique chemical and physical characteristics that are enigmatic and classifies it among a suite of lunar rocks called the Mg suite. Diffusion chronometry reveals relatively rapid cooling through high temperatures. Further, we find evidence for dissolution and recrystallization of olivine in this sample and use this as evidence for petrogenesis of this sample via reactive infiltration. We also note that the timescales reported by diffusion chronometry on phosphorus using the currently accepted diffusivity of phosphorus in olivine are unrealistically short.

In Chapter 3, we follow up on the discrepancies in P diffusion timescales found in Chapter 2. We do this in two ways: 1) We use models comparing timescales reported from two different heterogeneities in the same crystal. 2) We heat olivine grains with characterized heterogeneities in P content and characterize any diffusive relaxation of P. In the models comparing timescales, we demonstrate values from P diffusion chronometry significantly underreport diffusive timescales. The experiments reveal a complete lack of observable diffusive relaxation in the samples. These findings explain why we found unrealistically short timescales in Chapter 1 for P but create a new question: why do we not observe any diffusive relaxation?

Chapter 4 addresses this question using nanoscale analysis. Several diverse grains of olivine with heterogeneities in P content are characterized using transmission electron microscopy and atom probe tomography. We find nm scale heterogeneities in P content for even the slowest cooled samples that suggest that diffusive relaxation must be even more sluggish than Si, or not occur at all. We find P is anticorrelated to Mg and Si in all our olivine samples. These results lead us to suggest that phosphorus is accommodated in olivine on the tetrahedral site using vacancies in the octahedral site.

Chapter 5 looks at one way to apply diffusion chronometry to systems that is highly resistant to uncertainties in diffusivities. We apply diffusion chronometry to PO and BO chondrules using several trace elements. We find that these chondrules must have experienced relatively similar diffusive timescales to each other. Therefore, we recommend a petrogenesis of these chondrules that is more reliant on chemical supersaturation than undercooling.

6.2 Future research

Every chapter in this work highlights areas where additional research could benefit the field of igneous petrology. Chapter 1 highlights new features in the most intensely studied Apollo sample and cooling conditions that fundamentally challenge longstanding assumptions in the petrogenesis of the Mg suite. Therefore, lunar geology could benefit from having another look at the Mg suite using modern analytical techniques. Also, it must be shown that the textures observed in troctolite 76535 can be reproduced with reactive infiltration. Chapter 2 highlights novel methods to evaluate diffusivities of intragrain heterogeneities. These same methods could be applied to other systems in olivine, such as Al, or internal zoning of other elements. Given the recent finding that the presence of silicate melt can affect the diffusivities inside a crystal (Shea et al., 2023), methods like these could be utilized to reproduce conditions in natural diffusive relaxation more accurately. Chapter 3 provides a totally new way to analyze intragrain heterogeneities at the nanoscale in olivine. More than any other single chapter, this probably creates new opportunities for new research. Nearly every diffusive system in olivine (and arguably, any mineral) could undergo the same analysis to better understand how point defects are accommodated at the smallest scales. Finally, Chapter 5 demonstrates a new route for analysis of chondrule textural types, which could be applied to POP, radiating pyroxene, and all textural classes in type II chondrules. Further, the comparative diffusion analysis method could open up research studying diffusive timescales in systems with high degrees of uncertainty in their environments.

Appendix A: Chapter 2 Supplementary Material

Supplementary Figures:

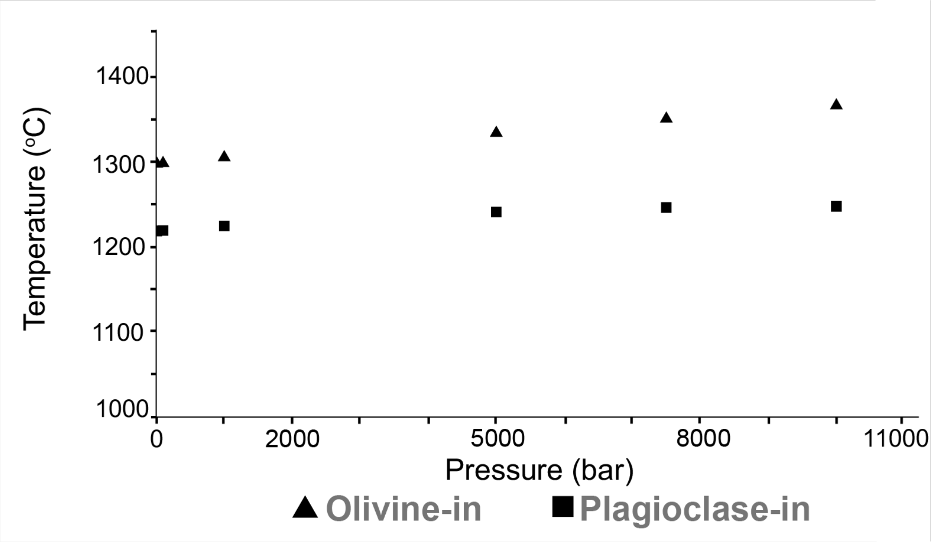

Figure A-1: Olivine and plagioclase in-temperatures for the composition shown used to define initial temperature for modelling (Methods, Table A1).

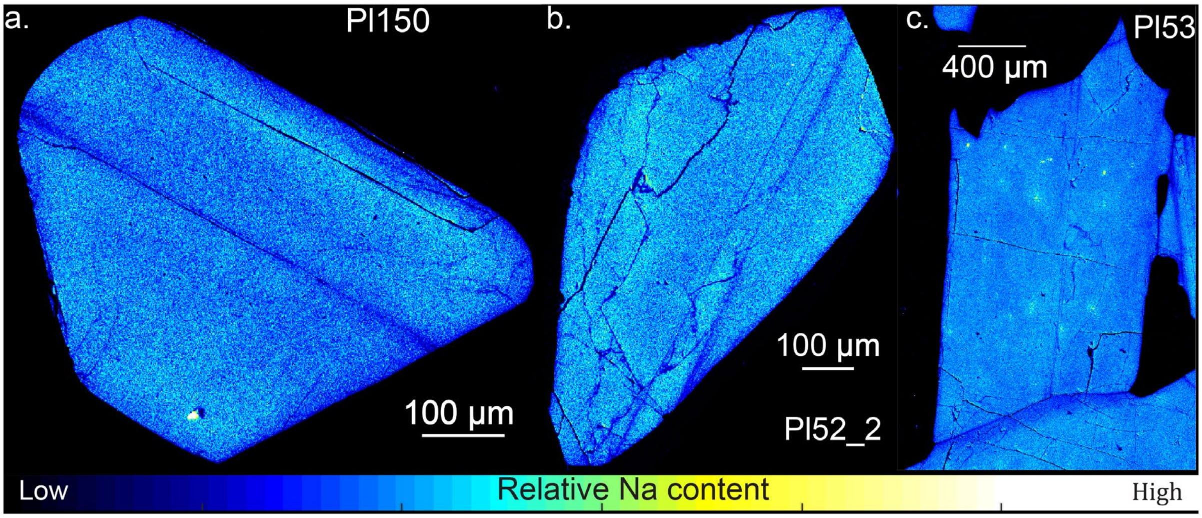

Figure A-2: X-ray intensity maps of plagioclase grains that were not selected for numerical modeling. a. Plagioclase grain in 150: This grain displays heterogeneities as well as igneous growth facets, but cracks render it unsuitable. b. Another plagioclase in slide ,52. This pervasively cracked grain contains spatially resolvable compositional variation (concentric zoning) that may have initially been coherent but cannot be analyzed numerically. c. This plagioclase grain in slide ,53 lacks detectable compositional zoning. Note the lower Na concentration near the neighboring plagioclase crystal, which suggests that intra-plagioclase boundaries are a pathway for Na migration.

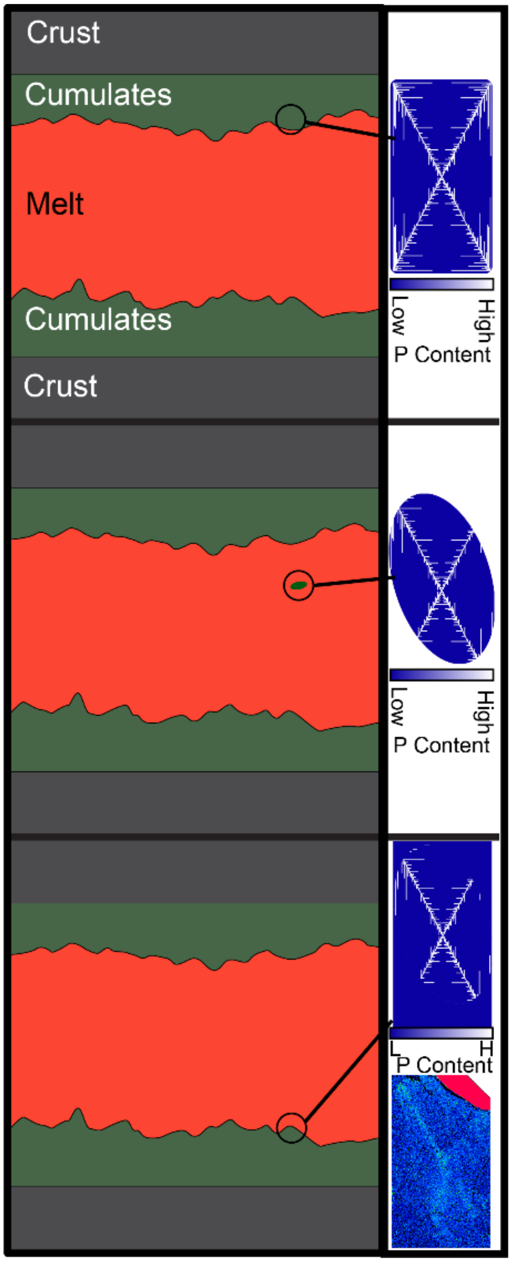

Figure A-3*:* Alternative model to generate P-rich lamellae and dissolution bounds. An olivine crystal grows rapidly on the roof of a magma chamber, preserving compositional heterogeneities. The crystal detaches and sinks through the melt-rich center of the chamber. Conditions at the center of the chamber are outside of the olivine stability field, and the crystal partially dissolves. The remaining portion of the grain settles to the bottom of the chamber, where olivine is again stable, and growth resumes. We argue this model is not a plausible explanation for the textural features and compositional variations within the samples we analyzed. The sharpness of the lamellae point to a more rapid cooling history than this scenario can realistically offer. Also, the model only explains the growth-dissolution-growth relationships for crystals that settled through the melt column, as illustrated. We infer that the olivine we observed is of general relevance, rather than a special case. This also points to a mechanism, such as reactive infiltration, that operates on a majority of olivine grains.

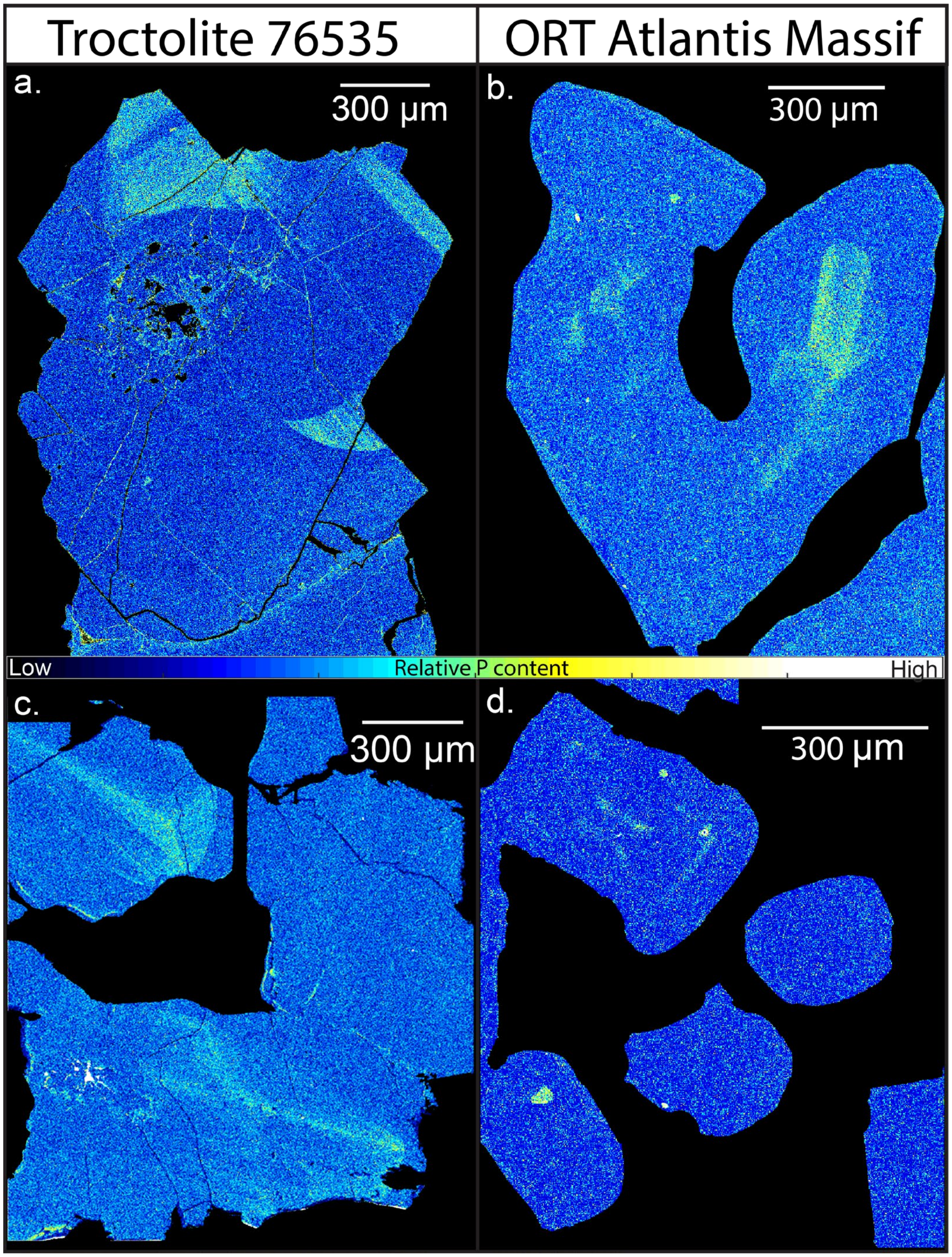

Figure A-4: Comparison of P rich zoning in troctolite 76535 (a,c) and olivine rich troctolites (b,d) from Atlantis Massif[24,33]. Maps only display relative intensity. Actual phosphorus content varies: the maximum P content found in ORT grains was 524 ppm[24]; the observed P contents in 76535 extend above 1000 ppm (Table A-7)

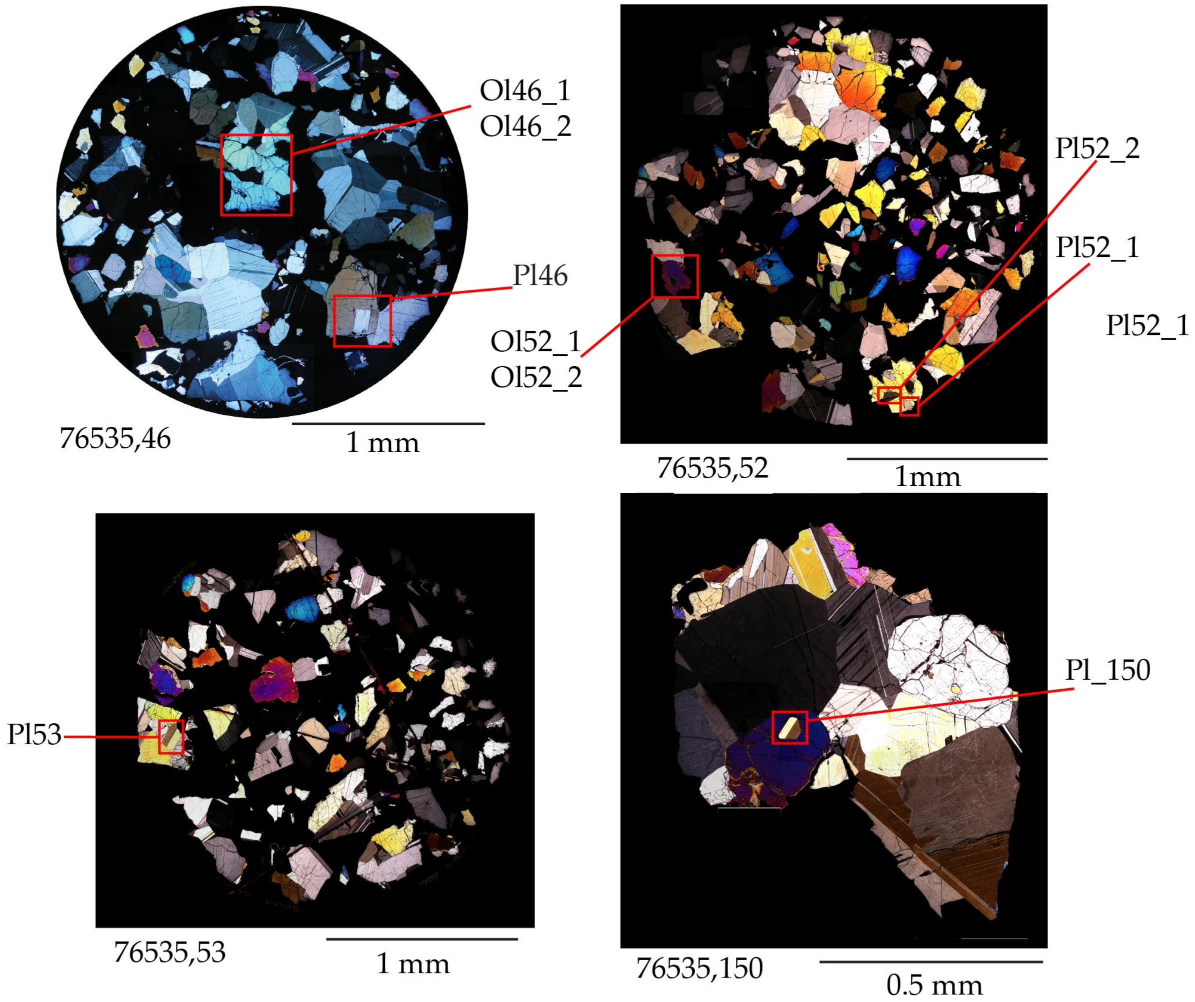

Figure A-5: Locations of all grains used in this study overlaid on crossed polarized light images of slides.

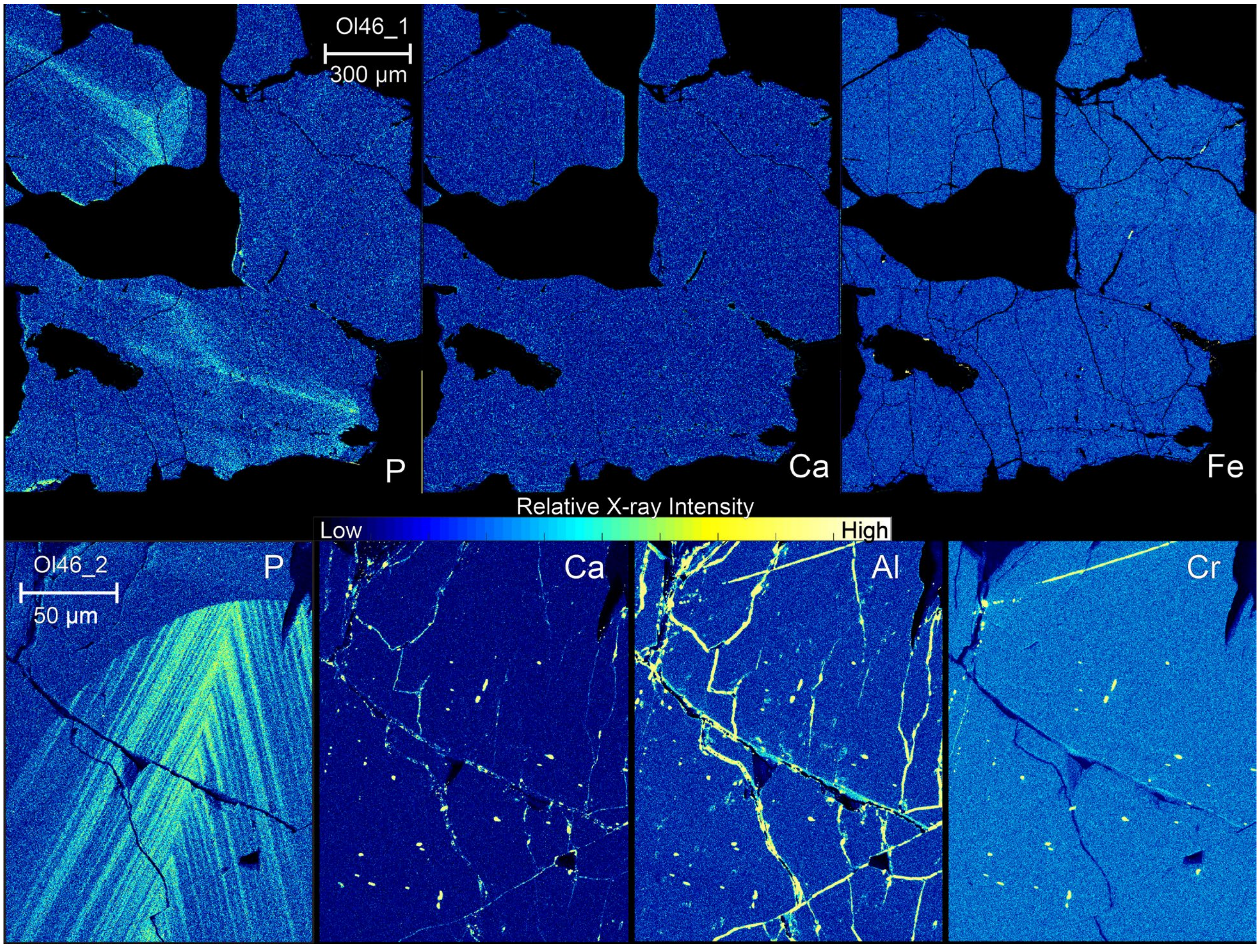

Figure A-6: X-ray compositional maps of olivine in slide , 46. Though sharp elemental truncation is observed in phosphorus, all other elements are relatively homogeneous within a given olivine grain.

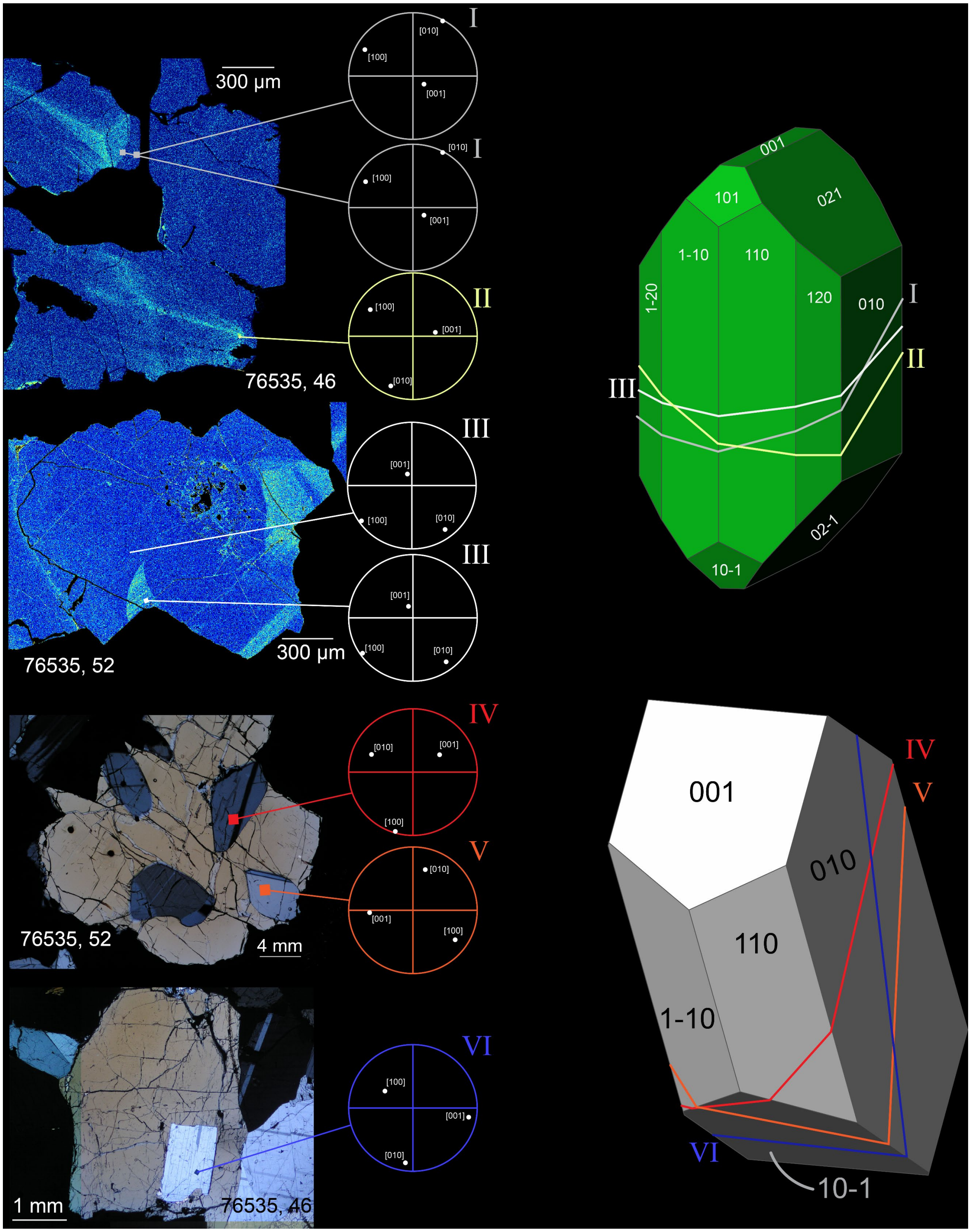

Figure A-7: Orientations of relevant grains as determined by EBSD. Note that orientations are constant on either side of the truncations in P lamellae. 3D models of each crystal produced in SHAPE v 7.4

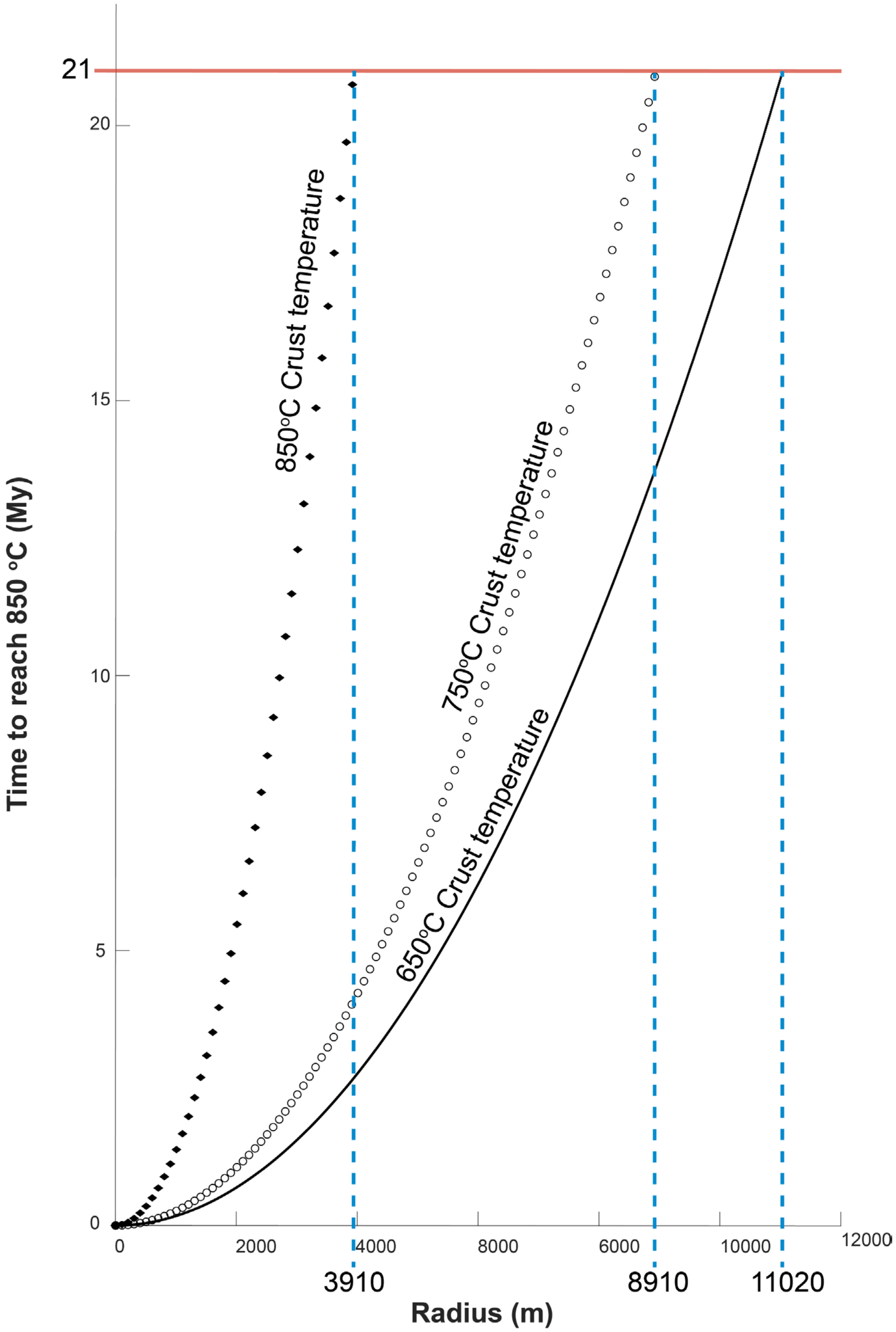

Figure A-8: Maximum magma chamber radius for a spherical body to cool to 850°C and still preserve all heterogeneities reported in this study. See the Methods section for details.

Supplementary Tables:

Table A-1: Parent melt composition used for troctolite 76535.

Oxide	SiO_2	TiO_2	Al_2O_3	Cr_2O_3	FeO_T	MnO	MgO	CaO	Na_2O	K_2O	P_2O	Total
O'Sullivan&Neal	46-52	--	19-22	--	8-10	--	10-13	10-12	--	--	--	93-109
Sonzogni&Treiman	57.92	0.39	17.52	0.06	2.89	0.06	10.08	10.70	0.29	0.07	0	99.98
This study	47.16	0.39	19.16	0.06	8.00	0.10	13.01	11.79	0.19	0.07	0.07	100.00

Table A-2: Standard analyses used for olivine measurements. bd= below detection (<30 ppm).

	A-99 Glass (NMNH 113498-1, n=6)					Springwater olivine (USNM 2566, n=6)				
Oxide	P_2O_5	SiO_2	MgO	FeO_T	Total	P_2O_5	SiO_2	MgO	FeO_t	Total
Mean (Wt %)	0.39	47.93	5.06	13.18	66.56	bd	38.97	44.31	16.62	99.89
Standard Deviation	0.00	0.17	0.02	0.06	0.26	-	0.11	0.09	0.03	0.22
Relative Deviation	0.01	0.00	0.00	0.00	0.02	-	0.00	0.00	0.00	
Published(Jarosewich et al., 1980) (Wt %)	0.38	50.94	5.08	13.49	69.89	-	38.95	43.58	16.62	99.15
Avg/Published	1.03	0.94	1.00	0.98	-	-	1.00	1.02	1.00	-

Table A-3: Standard analyses used for plagioclase measurements.

	Anorthite standard (NMNH 137041, n=17)							
Oxide	SiO_2	Al_2O_3	FeO_T	MgO	CaO	Na_2O	K_2O	Total
Mean (Wt %)	43.68	35.85	0.46	0.04	19.06	0.53	0.01	99.63
Standard Deviation	0.29	0.12	0.01	0.00	0.08	0.01	0.01	0.53
Relative Deviation	0.01	0.00	0.03	0.08	0.00	0.03	0.56	0.72
Published(Wt %)	44.00	36.03	0.62	0.02	19.09	0.53	0.03	100.32
Avg/Published	0.99	1.00	0.75	1.95	1.00	0.99	0.30	-

Table A-4: Profile from Pl46 (Figure 2.2)

Distance(um)	SiO2	Al_2O_3	Cr_2O_3	FeO_T	NiO	MgO	CaO	Na_2O	K_2O	total
0.00	40.22	0.60	0.04	11.71	0.00	46.82	0.27	0.00	0.00	99.66
15.18	44.20	36.21	0.01	0.13	0.01	0.09	19.47	0.41	0.06	100.59
30.64	44.14	35.93	0.00	0.10	0.00	0.10	19.43	0.44	0.07	100.20
46.03	44.30	36.07	0.00	0.08	0.00	0.09	19.47	0.46	0.07	100.53
61.30	44.38	36.11	0.00	0.07	0.00	0.09	19.53	0.43	0.07	100.67
76.79	44.24	36.04	0.00	0.08	0.01	0.15	19.49	0.46	0.07	100.54
92.33	44.22	36.02	0.00	0.05	0.01	0.08	19.42	0.45	0.07	100.31
107.51	44.32	36.12	0.01	0.05	0.00	0.08	19.51	0.44	0.07	100.60
123.09	44.30	36.20	0.00	0.05	0.01	0.09	19.55	0.44	0.07	100.70
138.31	44.25	36.01	0.01	0.06	0.00	0.13	19.56	0.43	0.06	100.52
153.62	44.19	36.16	0.01	0.05	0.01	0.08	19.57	0.40	0.06	100.54
169.16	44.13	36.15	0.00	0.05	0.00	0.07	19.50	0.43	0.06	100.39
184.47	44.08	36.18	0.00	0.05	0.01	0.09	19.56	0.43	0.07	100.45

199.74	44.07	35.88	0.00	0.19	0.00	0.57	19.35	0.42	0.06	100.54
215.19	44.05	36.24	0.00	0.06	0.00	0.11	19.53	0.42	0.06	100.47
230.46	44.11	36.27	0.00	0.03	0.01	0.06	19.60	0.42	0.07	100.57
245.86	44.11	36.08	0.01	0.06	0.00	0.22	19.59	0.42	0.06	100.57
261.48	44.09	36.18	0.00	0.10	0.01	0.29	19.60	0.40	0.06	100.72
276.66	44.00	36.27	0.01	0.04	0.01	0.06	19.64	0.42	0.06	100.52
292.24	43.98	36.22	0.00	0.08	0.01	0.22	19.52	0.41	0.06	100.50
307.51	43.90	36.24	0.00	0.07	0.01	0.19	19.54	0.42	0.06	100.44
322.78	43.93	36.30	0.01	0.05	0.01	0.08	19.56	0.41	0.06	100.39
338.32	43.88	36.31	0.00	0.04	0.02	0.06	19.63	0.41	0.06	100.41
353.63	43.86	36.10	0.01	0.08	0.00	0.25	19.55	0.41	0.06	100.32
368.94	43.83	36.06	0.01	0.05	0.00	0.19	19.68	0.39	0.06	100.27
384.34	43.91	36.28	0.00	0.03	0.00	0.06	19.65	0.42	0.06	100.41
399.79	40.88	34.15	0.00	0.05	0.00	0.12	18.25	0.40	0.06	93.92
415.02	43.95	36.01	0.04	0.16	0.00	0.38	19.45	0.39	0.06	100.45
430.46	43.79	36.15	0.01	0.05	0.01	0.08	19.63	0.39	0.06	100.17
445.86	43.98	36.21	0.00	0.05	0.00	0.10	19.65	0.38	0.06	100.43
461.17	43.95	36.22	0.01	0.05	0.00	0.09	19.63	0.39	0.06	100.39
476.62	43.46	36.07	0.00	0.03	0.00	0.05	19.49	0.39	0.05	99.54
491.98	43.79	36.21	0.00	0.04	0.00	0.07	19.66	0.40	0.06	100.23
507.42	43.90	36.07	0.00	0.05	0.01	0.10	19.63	0.38	0.06	100.21
522.78	43.91	36.13	0.00	0.06	0.00	0.12	19.65	0.38	0.06	100.32
538.14	43.94	36.01	0.01	0.06	0.00	0.12	19.66	0.39	0.06	100.26
553.60	43.89	36.03	0.01	0.06	0.00	0.12	19.63	0.40	0.06	100.19
568.90	43.91	36.02	0.00	0.06	0.01	0.12	19.70	0.38	0.06	100.27
584.26	43.96	36.05	0.00	0.05	0.01	0.10	19.60	0.40	0.06	100.23
599.66	43.90	36.01	0.00	0.06	0.01	0.11	19.54	0.42	0.06	100.12
615.11	43.91	35.90	0.00	0.06	0.00	0.12	19.59	0.42	0.06	100.07
630.51	44.03	35.86	0.00	0.07	0.00	0.13	19.57	0.41	0.06	100.13
645.87	44.05	35.73	0.12	0.11	0.00	0.20	19.51	0.45	0.07	100.24

661.22	44.10	35.75	0.00	0.07	0.01	0.12	19.43	0.45	0.07	99.98
676.63	44.13	35.77	0.00	0.07	0.00	0.14	19.47	0.44	0.07	100.09
691.94	44.22	35.82	0.00	0.07	0.02	0.13	19.42	0.45	0.07	100.19
707.34	43.81	35.73	0.00	0.08	0.00	0.14	19.44	0.44	0.07	99.70
722.70	43.81	35.94	0.01	0.08	0.00	0.09	19.51	0.43	0.07	99.94
738.10	43.33	35.95	0.00	0.10	0.00	0.06	19.38	0.40	0.05	99.27

Table A-5: Profile from pl52_1 (Figure A-3).

Distance (um)	Na2O WT%	SiO2 WT%	Al2O3 WT%	CaO WT%	FeOT WT%	MgO WT%	K2O WT%	Total
0.00	0.33	43.15	35.93	19.51	0.03	0.06	0.05	99.05
5.63	0.35	43.44	36.04	19.40	0.04	0.06	0.05	99.39
11.11	0.36	43.94	36.08	19.49	0.04	0.07	0.04	100.02
16.71	0.37	43.38	36.09	19.41	0.03	0.06	0.04	99.39
22.28	0.36	43.56	36.14	19.42	0.05	0.07	0.05	99.65
27.76	0.35	43.58	35.36	19.42	0.04	0.23	0.05	99.03
33.16	0.24	45.03	30.19	20.54	0.32	3.14	0.03	99.50
38.78	0.20	47.03	24.58	21.48	0.64	6.01	0.03	99.96
44.27	0.34	43.56	36.08	19.47	0.04	0.07	0.04	99.61
49.75	0.37	43.47	36.12	19.43	0.03	0.06	0.04	99.53
55.31	0.37	43.43	36.09	19.38	0.04	0.07	0.04	99.40
61.00	0.37	43.47	35.90	19.43	0.05	0.08	0.04	99.34
66.40	0.37	43.40	36.00	19.49	0.03	0.08	0.04	99.43
71.88	0.36	43.36	36.00	19.41	0.04	0.08	0.05	99.31
77.56	0.35	43.35	35.95	19.40	0.04	0.09	0.04	99.22
83.12	0.35	43.12	35.95	19.46	0.03	0.09	0.04	99.04
88.61	0.35	43.26	35.90	19.38	0.05	0.10	0.05	99.08
94.21	0.34	43.49	35.92	19.45	0.06	0.11	0.05	99.41
99.63	0.33	43.22	35.89	19.47	0.05	0.10	0.04	99.10

105.18	0.34	43.06	35.88	19.52	0.03	0.10	0.04	98.98
110.66	0.34	43.09	35.88	19.40	0.04	0.11	0.04	98.90
116.27	0.34	43.24	35.80	19.35	0.04	0.11	0.05	98.92
121.83	0.34	43.19	35.80	19.39	0.04	0.11	0.04	98.91
127.37	0.34	42.75	35.79	19.35	0.05	0.10	0.03	98.41
133.00	0.35	43.02	35.68	19.33	0.03	0.10	0.05	98.56
138.40	0.33	42.73	35.82	19.44	0.05	0.11	0.04	98.51
144.02	0.35	43.62	36.30	19.34	0.06	0.11	0.04	99.81
149.38	0.34	42.57	35.40	19.21	0.05	0.10	0.04	97.72
154.98	0.33	42.89	35.75	19.38	0.05	0.12	0.03	98.55
160.56	0.33	32.93	32.20	15.48	0.20	0.17	0.11	81.42
166.11	0.34	42.19	35.48	19.25	0.05	0.12	0.05	97.48
171.65	0.35	42.82	35.72	19.41	0.04	0.12	0.04	98.50
177.19	0.33	43.04	35.79	19.36	0.05	0.11	0.05	98.72
182.67	0.33	42.92	35.94	19.42	0.04	0.12	0.05	98.82
188.24	0.36	43.19	35.76	19.45	0.04	0.12	0.04	98.96
193.78	0.33	43.29	35.89	19.36	0.04	0.12	0.05	99.07
199.40	0.32	43.46	36.02	19.32	0.05	0.12	0.04	99.32
204.87	0.33	43.25	35.92	19.38	0.04	0.11	0.04	99.08
210.51	0.35	43.40	36.02	19.42	0.05	0.11	0.05	99.40
215.99	0.35	42.87	35.83	19.31	0.05	0.12	0.04	98.56
221.46	0.34	43.32	35.92	19.41	0.04	0.12	0.04	99.19
227.00	0.34	43.42	35.91	19.39	0.05	0.11	0.04	99.26

Table A-6: Profile from Ol52

Distance (um)	P2O5 WT%	SiO2 WT%	MgO WT%	FeO$_T$ WT%	Total
0.00	0.03	40.27	48.44	12.09	100.82
4.96	0.02	40.32	48.40	12.13	100.87
10.13	0.02	40.37	48.44	12.07	100.89
15.11	0.04	40.38	48.47	12.08	100.97
20.07	0.04	40.38	48.46	12.12	100.99
25.12	0.04	40.38	48.54	12.03	100.99
30.20	0.03	40.39	48.51	12.15	101.07
35.09	0.03	40.37	48.49	12.19	101.08
40.25	0.03	40.34	48.34	12.20	100.92
45.05	0.03	40.38	48.36	12.29	101.05
50.10	0.03	40.37	48.40	12.21	101.00
55.15	0.06	40.36	48.40	12.27	101.08
60.21	0.05	40.31	48.30	12.23	100.89
65.12	0.03	40.35	48.40	12.16	100.93
70.18	0.03	40.35	48.46	12.21	101.05
75.03	0.03	40.36	48.49	12.21	101.08
80.00	0.03	40.35	48.48	12.21	101.07
85.18	0.04	40.37	48.49	12.22	101.13
90.25	0.03	40.41	48.45	12.20	101.10
95.12	0.03	40.72	48.03	12.19	100.98
100.20	0.02	40.18	48.27	12.18	100.66
105.27	0.04	40.24	48.47	12.21	100.97
110.12	0.03	40.28	48.50	12.25	101.06
115.20	0.05	40.26	48.44	12.16	100.92
120.28	0.04	40.26	48.42	12.18	100.91
125.24	0.05	40.30	48.45	12.18	100.97
130.21	0.06	40.23	48.43	12.22	100.93

135.19	0.05	40.20	48.49	12.20	100.94
140.25	0.05	40.19	48.42	12.19	100.86
145.22	0.06	40.15	48.41	12.19	100.82
150.18	0.05	40.19	48.39	12.20	100.83
155.17	0.05	40.21	48.42	12.17	100.85
160.21	0.04	40.23	48.37	12.17	100.80
165.21	0.03	40.22	48.33	12.26	100.84
170.16	0.03	40.23	48.32	12.15	100.74
175.15	0.03	40.22	48.31	12.21	100.78
180.29	0.05	40.18	48.32	12.18	100.73
185.38	0.05	40.17	48.35	12.15	100.71
190.16	0.04	40.16	48.33	12.27	100.79
195.22	0.01	40.14	48.32	12.25	100.70
200.27	0.00	40.15	48.29	12.23	100.67
205.14	0.00	40.20	48.39	12.16	100.75

Table A-7: Profile for Ol46 with all 5 spectrometers analyzing phosphorus. Analysis assumed 57.29 wt% MgO and 42.71 wt% SiO2

Distance (um)	P2O5 WT% Spectrometer 1	P2O5 WT% Spectrometer 2	P2O5 WT% Spectrometer 3	P2O5 WT% Spectrometer 4	P2O5 WT% Spectrometer 5	Average
0.000	0.012	0.003	0.007	0.006	0.010	0.007
1.475	0.013	0.008	0.005	0.008	0.010	0.009
2.905	0.004	0.005	0.008	0.008	0.005	0.006
4.471	0.006	0.011	0.008	0.011	0.007	0.008
5.996	0.007	0.008	0.011	0.005	0.006	0.007
7.474	0.007	0.010	0.008	0.008	0.008	0.008
8.959	0.020	0.021	0.027	0.020	0.022	0.022
10.623	0.026	0.024	0.025	0.016	0.016	0.022
12.012	0.048	0.053	0.051	0.055	0.061	0.054
13.533	0.053	0.053	0.051	0.049	0.044	0.050
15.011	0.020	0.027	0.027	0.025	0.025	0.025
16.539	0.025	0.024	0.023	0.028	0.023	0.025
18.155	0.027	0.021	0.024	0.023	0.019	0.023
19.585	0.028	0.023	0.031	0.030	0.026	0.028
22.231	0.049	0.048	0.052	0.049	0.053	0.050
24.011	0.026	0.034	0.023	0.027	0.032	0.028
25.538	0.030	0.023	0.030	0.030	0.039	0.031
26.876	0.056	0.054	0.059	0.058	0.051	0.056
28.667	0.042	0.039	0.035	0.037	0.038	0.038
30.055	0.026	0.024	0.028	0.019	0.025	0.024
31.541	0.025	0.023	0.027	0.021	0.025	0.024
33.068	0.015	0.016	0.024	0.023	0.018	0.019
34.681	0.023	0.024	0.021	0.023	0.017	0.021
36.076	0.026	0.019	0.025	0.023	0.021	0.023

37.600	0.020	0.028	0.022	0.025	0.018	0.023
39.124	0.024	0.018	0.024	0.021	0.021	0.022
40.512	0.028	0.027	0.025	0.030	0.023	0.027
42.190	0.057	0.059	0.054	0.054	0.057	0.056
43.631	0.072	0.077	0.076	0.084	0.079	0.077
45.109	0.023	0.024	0.021	0.024	0.024	0.023
46.724	0.027	0.029	0.022	0.026	0.028	0.027
48.199	0.036	0.038	0.042	0.036	0.033	0.037
49.677	0.079	0.081	0.084	0.084	0.080	0.081
51.243	0.092	0.085	0.091	0.090	0.079	0.088
52.767	0.055	0.051	0.053	0.053	0.056	0.054
54.067	0.037	0.039	0.043	0.046	0.046	0.042
55.633	0.050	0.058	0.051	0.049	0.054	0.053
57.249	0.062	0.063	0.059	0.066	0.065	0.063
58.552	0.025	0.030	0.022	0.027	0.025	0.026
60.340	0.065	0.068	0.058	0.058	0.068	0.063
61.773	0.063	0.064	0.066	0.073	0.065	0.066
63.114	0.089	0.085	0.085	0.082	0.086	0.085
64.635	0.096	0.095	0.090	0.094	0.088	0.093
66.163	0.084	0.071	0.064	0.082	0.074	0.075
67.687	0.088	0.092	0.084	0.093	0.087	0.089
69.208	0.085	0.071	0.072	0.075	0.063	0.073
70.736	0.097	0.091	0.093	0.089	0.091	0.092
72.128	0.105	0.103	0.109	0.099	0.107	0.104
73.744	0.069	0.072	0.069	0.074	0.069	0.070
75.306	0.040	0.035	0.041	0.027	0.035	0.036
76.559	0.088	0.084	0.084	0.080	0.080	0.083
78.271	0.045	0.045	0.047	0.049	0.048	0.047
79.656	0.059	0.057	0.057	0.057	0.058	0.058
81.269	0.058	0.064	0.059	0.060	0.061	0.060

82.747	0.034	0.024	0.029	0.026	0.025	0.028
84.363	0.044	0.041	0.043	0.051	0.039	0.044
85.703	0.080	0.071	0.065	0.075	0.070	0.072
87.316	0.037	0.039	0.045	0.038	0.041	0.040
88.711	0.089	0.080	0.083	0.081	0.076	0.082
90.236	0.075	0.080	0.082	0.082	0.081	0.080
91.891	0.034	0.031	0.023	0.031	0.028	0.030
93.232	0.069	0.066	0.066	0.066	0.059	0.065
94.798	0.080	0.075	0.077	0.083	0.085	0.080
96.320	0.068	0.075	0.068	0.076	0.076	0.073
97.711	0.049	0.041	0.042	0.046	0.040	0.043
99.052	0.054	0.050	0.055	0.052	0.049	0.052
100.704	0.070	0.069	0.073	0.070	0.079	0.072
102.407	0.051	0.050	0.056	0.048	0.056	0.052
103.707	0.089	0.090	0.090	0.086	0.084	0.088
105.362	0.102	0.106	0.106	0.100	0.109	0.105
106.802	0.099	0.105	0.099	0.105	0.101	0.102
108.146	0.109	0.111	0.102	0.116	0.120	0.111
109.855	0.108	0.103	0.103	0.102	0.101	0.104
111.299	0.081	0.075	0.078	0.075	0.078	0.077
112.820	0.084	0.084	0.085	0.086	0.095	0.087
114.344	0.072	0.077	0.075	0.075	0.071	0.074
115.869	0.066	0.075	0.073	0.070	0.076	0.072

Video A-1: Attached, or found online at: https://static-content.springer.com/esm/art%3A10.1038%2Fs41467-021-26841-4/MediaObjects/41467_2021_26841_MOESM4_ESM.gif

Appendix B: Chapter 3 Supplementary Material

Supplementary Figures:

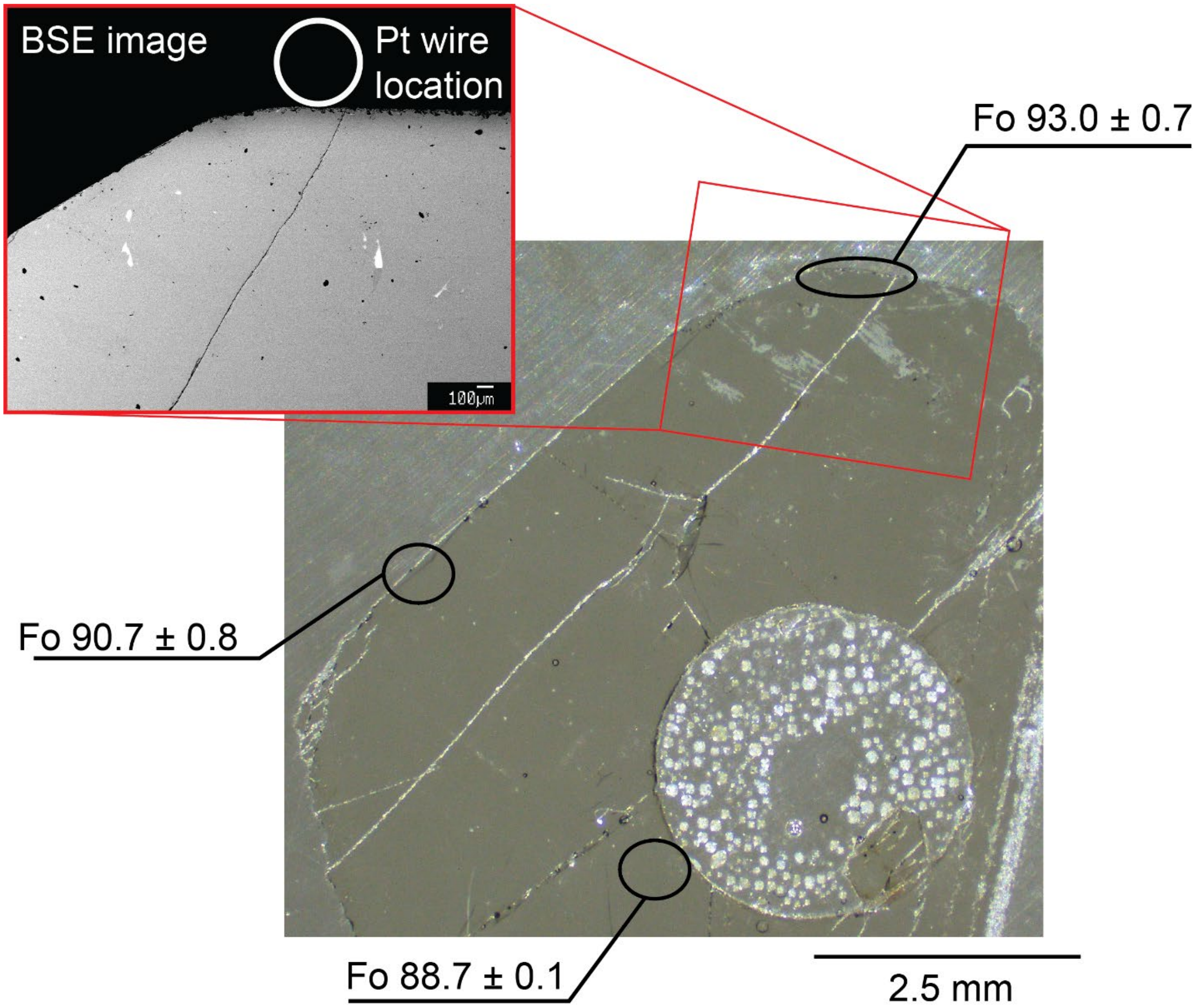

Figure B-1: SCO crucible after being held by pure Pt wire for 10 days at 1400 °C. Fe contents decrease near wire significantly, changing the Fo# relative to the interior of the grain. Though this effect is much more pronounced near the wire, surface diffusion increases Fo# even on distal parts of the grain. The crucible was initially homogenous and Fo 88.7. Fo contents were determined by the average of 5 EPMA points

Figure B-2: Pt wire with 59.8 wt% Fe after 10 days on SCO at 1400 °C. Notice a substantial amount of oxides have grown around the wire.

Figure B-3: Initially pure Pt wire after 10 days on SCO at 1400 °C. The wire has bore ~25 microns into the olivine here, and has become 11.5 wt% Fe.

Supplementary Tables:

Table B-1: Standard analyses used for olivine measurements. bd= below detection (<30 ppm).

	A-99 Glass (NMNH 113498-1, n=6)					Springwater olivine (USNM 2566, n=6)				
Oxide	P_2O_5	SiO_2	MgO	FeO_T	Total	P_2O_5	SiO_2	MgO	FeO_t	Total
Mean (Wt %)	0.45	50.45	4.94	13.1	68.94	0.002	39.3	43.71	16.53	99.54
Standard Deviation	0.01	0.53	0.07	0.2	-	0.003	0.3	0.22	0.18	-
Relative Deviation	0.02	0.01	0.01	0.01	-	1.6	0.001	0.005	0.01	-
Published(Jarosewich et al., 1980) (Wt %)	0.38	50.94	5.08	13.49	69.89	-	38.95	43.58	16.62	99.15
Avg/Published	1.2	0.99	0.97	0.97	-	-	1.0	1.0	0.99	-

Table B-2: Crystal 2 (Figure 3.1) initial compositional profile

Distance (um)	MgO Wt%	SiO_2 Wt%	FeO Wt%	P_2O_5 Wt%	CaO Wt%	Al_2O_3 Wt%	TOTAL
0.00	47.15	40.11	11.36	0.02	0.13	0.03	98.79
5.70	47.43	40.04	11.21	0.01	0.13	0.04	98.86
11.42	47.45	40.07	11.14	0.01	0.13	0.04	98.84
17.34	47.22	40.05	11.17	0.02	0.14	0.03	98.63
23.00	47.21	39.90	11.28	0.03	0.13	0.04	98.60

Table B-3: Crystal 2: Compositional profile after 10 days

Distance (um)	MgO WT%	SiO2 WT%	FeO WT%	P2O5 WT%	P2O5 WT%2	Al2O3 WT%	Cr2O3 WT%
0.00	48.39	41.19	10.96	0.02	0.02	0.03	0.04
2.14	48.23	41.13	10.98	0.03	0.03	0.04	0.03
3.96	48.18	41.13	10.92	0.03	0.03	0.03	0.04
5.81	48.21	41.17	10.96	0.01	0.01	0.03	0.04
8.02	48.24	41.16	11.03	0.01	0.01	0.03	0.04
9.96	48.11	41.12	10.99	0.01	0.01	0.03	0.03
12.08	48.20	41.10	10.99	0.01	0.00	0.03	0.03
14.14	47.89	40.83	11.06	0.10	0.11	0.04	0.04
15.99	48.21	41.13	11.01	0.01	0.01	0.03	0.04
17.99	48.22	41.09	11.08	0.02	0.02	0.03	0.04
20.18	48.13	41.03	10.99	0.05	0.05	0.03	0.04
21.89	48.15	41.08	11.09	0.01	0.01	0.03	0.03
24.00	48.16	41.04	11.04	0.05	0.05	0.03	0.04
26.15	48.11	41.03	11.09	0.05	0.05	0.03	0.04
28.20	48.13	41.06	11.05	0.01	0.02	0.03	0.04
30.00	48.09	41.01	11.06	0.01	0.01	0.03	0.03
32.14	48.11	41.01	11.06	0.02	0.02	0.03	0.04
34.16	48.08	41.02	11.11	0.02	0.02	0.03	0.04
36.00	48.06	41.02	11.11	0.02	0.02	0.03	0.04
38.12	48.03	41.02	11.07	0.02	0.01	0.03	0.03
40.07	47.95	40.99	11.06	0.02	0.01	0.03	0.04
41.98	47.99	41.00	11.13	0.02	0.02	0.03	0.04
44.01	47.99	40.91	11.12	0.08	0.09	0.04	0.04
46.25	47.91	40.85	11.09	0.12	0.12	0.04	0.04
48.10	48.01	40.93	11.08	0.12	0.12	0.04	0.04
50.02	48.01	40.97	11.05	0.09	0.09	0.04	0.04
52.04	48.01	40.99	11.11	0.01	0.01	0.03	0.03
53.95	47.98	40.99	11.14	0.03	0.03	0.03	0.04
55.99	48.03	40.99	11.08	0.02	0.02	0.03	0.04
58.03	47.95	40.93	11.07	0.02	0.02	0.03	0.05
60.09	48.00	40.94	11.07	0.02	0.02	0.03	0.04
62.01	48.01	40.96	11.11	0.02	0.01	0.03	0.05
64.04	47.96	40.95	11.07	0.07	0.07	0.03	0.05
66.08	47.96	40.83	11.10	0.11	0.11	0.04	0.05

67.98	48.00	40.93	11.11	0.05	0.05	0.03	0.03
70.12	47.97	40.84	11.07	0.12	0.13	0.04	0.05
72.24	47.92	40.94	11.14	0.04	0.04	0.03	0.05
74.06	47.95	40.90	11.11	0.07	0.07	0.03	0.05
75.97	47.91	40.92	11.08	0.06	0.07	0.03	0.05
78.06	47.88	40.83	11.07	0.14	0.15	0.04	0.05
79.98	47.93	40.80	11.14	0.16	0.17	0.04	0.05
82.02	47.94	40.81	11.13	0.17	0.17	0.04	0.05
84.16	47.90	40.79	11.14	0.12	0.13	0.04	0.05
85.99	47.92	40.79	11.12	0.16	0.16	0.04	0.06
88.05	47.92	40.78	11.09	0.14	0.15	0.04	0.04
90.27	47.90	40.77	11.10	0.17	0.18	0.04	0.05
92.08	47.84	40.73	11.10	0.19	0.20	0.04	0.05
94.14	47.90	40.77	11.14	0.15	0.16	0.04	0.05
96.15	47.91	40.83	11.14	0.12	0.13	0.04	0.04
97.96	47.95	40.76	11.10	0.16	0.16	0.04	0.06
100.12	47.93	40.78	11.13	0.16	0.17	0.04	0.05
102.13	47.85	40.69	11.13	0.19	0.19	0.04	0.05
104.04	47.92	40.78	11.14	0.15	0.15	0.05	0.05
105.91	47.91	40.85	11.12	0.07	0.07	0.04	0.05
108.03	47.81	40.83	11.11	0.05	0.04	0.04	0.04
110.17	47.91	40.88	11.10	0.02	0.02	0.03	0.05
112.13	47.97	40.97	11.09	0.02	0.02	0.03	0.05
114.06	47.98	40.94	11.13	0.02	0.02	0.03	0.05
116.08	47.96	40.94	11.13	0.03	0.03	0.03	0.05
118.12	47.98	40.90	11.15	0.03	0.04	0.04	0.05
119.93	47.92	40.87	11.08	0.04	0.04	0.04	0.05
122.15	47.90	40.82	11.10	0.05	0.05	0.04	0.05
123.90	47.92	40.87	11.12	0.03	0.03	0.04	0.05
125.92	47.94	40.86	11.07	0.03	0.02	0.03	0.05
128.04	47.97	40.90	11.09	0.02	0.02	0.03	0.04
130.06	47.95	40.88	11.05	0.01	0.01	0.03	0.05
131.99	47.97	40.89	11.09	0.01	0.01	0.03	0.04
134.12	47.91	40.90	11.08	0.01	0.01	0.03	0.04
135.95	47.91	40.92	11.09	0.01	0.01	0.03	0.05
137.94	47.98	40.91	11.09	0.00	0.01	0.03	0.05
140.07	47.99	40.89	11.06	0.00	0.00	0.03	0.05
142.08	48.04	40.92	11.09	0.00	0.01	0.03	0.04
144.04	47.98	40.90	11.06	0.00	0.00	0.04	0.05

146.16	47.96	40.92	11.09	0.00	0.00	0.03	0.04
148.17	48.00	40.88	11.10	0.00	0.00	0.03	0.05
150.01	48.04	40.91	11.05	0.00	0.00	0.03	0.04
152.03	48.01	40.91	11.08	0.00	0.00	0.03	0.04
154.04	47.96	40.93	11.07	0.01	0.00	0.03	0.04
156.09	48.10	40.93	11.12	0.00	0.00	0.03	0.04
158.15	47.98	40.87	11.10	0.00	0.00	0.03	0.04

Table B-4: Crystal 2 (Figure 3.1) compositional profile after 20 days.

Distance (um)	MgO WT%	SiO2 WT%	FeO WT%	P2O5 WT%	CaO WT%	Al2O3 WT%	MnO WT%	TOTAL
0.00	44.39	39.82	15.33	0.00	0.09	0.07	0.03	99.73
3.16	44.40	39.92	15.31	0.00	0.09	0.06	0.03	99.81
6.24	44.16	39.78	15.47	0.10	0.12	0.21	0.03	99.87
9.08	44.51	39.89	15.29	0.01	0.09	0.07	0.04	99.89
12.14	44.56	39.87	15.28	0.05	0.09	0.07	0.03	99.95
15.00	43.88	39.79	15.32	0.01	0.17	0.47	0.02	99.66
18.09	44.22	39.90	15.42	0.04	0.13	0.26	0.03	100.00
21.15	44.62	39.94	15.39	0.01	0.10	0.06	0.03	100.15
24.13	41.75	40.17	15.09	0.03	0.58	1.77	0.04	99.43
27.11	44.61	39.92	15.37	0.02	0.09	0.06	0.04	100.12
30.14	44.60	40.01	15.40	0.02	0.09	0.07	0.03	100.21
33.10	44.64	40.04	15.38	0.02	0.10	0.06	0.03	100.27
36.14	44.63	39.99	15.40	0.07	0.10	0.06	0.03	100.28
39.13	44.44	39.91	15.40	0.12	0.12	0.14	0.03	100.16
42.09	44.56	39.89	15.42	0.08	0.10	0.07	0.03	100.15
45.19	44.62	39.97	15.31	0.02	0.10	0.06	0.03	100.11
48.15	43.85	39.46	15.08	0.02	0.45	0.07	0.04	98.97
51.19	44.66	40.00	15.30	0.02	0.11	0.06	0.03	100.18
54.25	44.49	40.00	15.38	0.01	0.10	0.06	0.03	100.07
57.12	44.51	39.93	15.35	0.10	0.10	0.07	0.04	100.11
60.08	44.57	40.00	15.30	0.05	0.10	0.07	0.03	100.12
63.18	44.40	39.96	15.31	0.07	0.12	0.16	0.03	100.05
66.14	44.53	39.99	15.32	0.07	0.10	0.06	0.03	100.11
69.17	44.55	39.90	15.40	0.11	0.10	0.07	0.04	100.17

72.03	44.71	39.56	15.44	0.16	0.10	0.09	0.03	100.09
75.19	44.51	39.82	15.39	0.15	0.10	0.07	0.05	100.08
78.27	44.51	39.88	15.34	0.14	0.10	0.06	0.03	100.07
81.28	44.51	39.86	15.30	0.14	0.10	0.07	0.04	100.02
84.24	44.34	39.83	15.29	0.18	0.14	0.14	0.04	99.95
87.28	44.46	39.89	15.29	0.06	0.10	0.08	0.04	99.92
90.25	44.53	39.94	15.32	0.12	0.10	0.09	0.04	100.15
93.29	44.58	39.87	15.36	0.12	0.10	0.07	0.03	100.14
96.13	44.51	39.83	15.23	0.19	0.10	0.07	0.03	99.96
99.11	44.53	39.84	15.25	0.19	0.10	0.07	0.04	100.02
102.19	44.49	39.84	15.32	0.18	0.10	0.07	0.03	100.03
105.16	44.51	39.81	15.28	0.20	0.10	0.07	0.04	100.01
108.14	44.54	39.88	15.28	0.16	0.10	0.07	0.03	100.05
111.28	44.53	39.85	15.28	0.20	0.10	0.07	0.04	100.08
114.26	44.49	39.87	15.33	0.21	0.10	0.07	0.03	100.11
117.21	44.44	39.82	15.23	0.20	0.10	0.07	0.03	99.90
120.21	44.42	39.79	15.22	0.21	0.17	0.07	0.03	99.91
123.08	44.35	39.82	15.28	0.21	0.12	0.17	0.03	99.98

Table B-5: Crystal 8 (Figure 3.2) initial compositional profile

Distance (um)	MgO WT%	SiO2 WT%	FeO WT%	P2O5 WT%	P2O5 WT%2	Al2O3 WT%	Cr2O3 WT%	TOTAL
0.00	41.37	39.16	19.11	0.09	0.10	0.03	0.04	99.90
2.23	41.88	39.32	18.43	0.02	0.01	0.03	0.04	99.73
3.98	42.56	39.44	17.79	0.01	0.00	0.03	0.04	99.86
6.09	43.22	39.61	16.99	0.01	0.01	0.03	0.05	99.92
8.03	43.78	39.74	16.38	0.01	0.01	0.03	0.05	100.00
10.09	44.18	39.76	15.83	0.02	0.02	0.03	0.05	99.90
12.00	44.53	39.86	15.37	0.02	0.02	0.03	0.06	99.89
14.16	44.84	39.85	15.10	0.02	0.01	0.03	0.05	99.90
16.20	44.98	40.06	14.76	0.01	0.01	0.03	0.05	99.91
18.15	45.12	40.05	14.62	0.01	0.01	0.03	0.05	99.89
20.07	45.11	40.04	14.58	0.02	0.01	0.03	0.06	99.85
22.20	45.13	40.02	14.46	0.01	0.01	0.03	0.06	99.72
24.05	45.22	40.08	14.49	0.01	0.01	0.03	0.06	99.90
26.27	45.27	40.02	14.44	0.01	0.01	0.03	0.05	99.82
28.09	45.30	40.07	14.43	0.01	0.00	0.02	0.05	99.89
30.15	45.32	40.12	14.46	0.01	0.00	0.03	0.05	99.98

32.08	45.33	40.02	14.46	0.01	0.00	0.02	0.04	99.89
34.22	45.33	40.08	14.39	0.00	0.01	0.03	0.05	99.89
36.14	45.35	39.95	14.42	0.00	0.00	0.03	0.05	99.81
38.20	45.38	39.98	14.42	0.01	0.01	0.02	0.05	99.87
40.14	45.27	40.00	14.41	0.01	0.00	0.02	0.05	99.76
42.26	45.34	39.95	14.44	0.00	0.01	0.03	0.05	99.81
44.11	45.36	40.05	14.40	0.01	0.00	0.03	0.05	99.89
46.24	45.40	40.07	14.41	0.01	0.00	0.03	0.05	99.97
48.18	45.41	40.11	14.36	0.01	0.00	0.02	0.05	99.97
50.21	45.39	40.14	14.38	0.01	0.00	0.03	0.05	99.99
52.16	45.39	40.07	14.32	0.01	0.01	0.03	0.05	99.87
54.29	45.39	40.12	14.32	0.01	0.01	0.03	0.04	99.91
56.21	45.43	40.12	14.32	0.01	0.01	0.02	0.04	99.97
58.25	45.42	40.08	14.31	0.02	0.01	0.03	0.06	99.92
60.19	45.45	40.16	14.33	0.02	0.01	0.03	0.05	100.04
62.14	45.39	40.12	14.26	0.01	0.01	0.03	0.05	99.88
64.27	45.44	40.04	14.28	0.01	0.01	0.03	0.05	99.87
66.29	45.37	40.09	14.24	0.01	0.01	0.03	0.05	99.80
68.24	45.41	39.95	14.28	0.01	0.01	0.02	0.06	99.74
70.28	45.40	40.01	14.23	0.01	0.01	0.03	0.05	99.73
72.30	45.41	39.97	14.24	0.01	0.02	0.03	0.05	99.73
74.15	45.32	39.91	14.24	0.01	0.01	0.03	0.05	99.58
76.36	45.41	40.01	14.22	0.01	0.01	0.03	0.05	99.74
78.33	45.45	40.03	14.21	0.02	0.02	0.03	0.05	99.80
80.17	45.28	39.98	14.22	0.02	0.02	0.03	0.04	99.60
82.19	45.51	40.05	14.22	0.02	0.01	0.03	0.05	99.87
84.33	45.45	40.08	14.19	0.01	0.02	0.03	0.05	99.83
86.17	45.45	40.00	14.20	0.02	0.02	0.03	0.06	99.78
88.32	45.52	40.07	14.17	0.01	0.01	0.03	0.05	99.86
90.24	45.51	40.07	14.15	0.02	0.02	0.03	0.05	99.84
92.38	45.49	40.07	14.16	0.01	0.02	0.02	0.05	99.82
94.32	45.52	40.12	14.17	0.02	0.02	0.03	0.06	99.93
96.33	45.52	40.07	14.15	0.02	0.02	0.03	0.06	99.85
98.27	45.55	40.13	14.11	0.03	0.03	0.03	0.06	99.93
100.33	45.56	40.08	14.18	0.02	0.02	0.03	0.06	99.94
102.27	45.49	40.05	14.12	0.01	0.01	0.03	0.06	99.77
104.50	45.57	40.10	14.17	0.02	0.02	0.03	0.06	99.96
106.34	45.47	40.03	14.10	0.02	0.02	0.03	0.05	99.71
108.38	45.49	40.06	14.13	0.02	0.02	0.03	0.05	99.81
110.32	45.56	40.03	14.10	0.02	0.02	0.03	0.06	99.80
112.33	45.55	40.13	14.13	0.01	0.01	0.03	0.05	99.91
114.29	45.57	40.16	14.13	0.01	0.01	0.02	0.05	99.95
116.41	45.52	40.11	14.11	0.01	0.01	0.03	0.05	99.84

118.35	45.46	40.10	14.12	0.01	0.01	0.02	0.05	99.78
120.39	45.56	40.14	14.09	0.01	0.01	0.02	0.05	99.88
122.44	45.53	40.08	14.12	0.02	0.02	0.03	0.05	99.84
124.36	45.51	40.04	14.11	0.01	0.01	0.02	0.05	99.76
126.33	45.58	40.12	14.05	0.01	0.01	0.02	0.05	99.85
128.54	45.51	40.09	14.08	0.01	0.01	0.03	0.05	99.78
130.49	45.53	39.99	14.07	0.01	0.02	0.02	0.06	99.70
132.43	45.53	40.04	14.04	0.02	0.02	0.03	0.04	99.71
134.45	45.51	40.05	14.07	0.02	0.02	0.03	0.06	99.76
136.58	45.56	40.05	14.12	0.06	0.06	0.03	0.05	99.93
138.33	45.60	40.07	14.14	0.03	0.03	0.03	0.05	99.96
140.46	45.53	40.00	14.11	0.01	0.01	0.03	0.05	99.74
142.48	45.59	40.07	14.13	0.01	0.01	0.03	0.06	99.89
144.38	45.50	40.06	14.05	0.01	0.01	0.02	0.06	99.70
146.50	45.44	40.00	14.10	0.02	0.02	0.03	0.05	99.65
148.63	45.46	40.03	14.10	0.02	0.02	0.03	0.05	99.71
150.36	45.51	40.07	14.05	0.01	0.01	0.03	0.05	99.72
152.50	45.52	40.03	14.09	0.01	0.01	0.03	0.05	99.73
154.54	45.61	40.09	14.12	0.01	0.01	0.03	0.06	99.93
156.56	45.54	40.08	14.08	0.01	0.01	0.03	0.04	99.80
158.38	45.53	40.05	14.08	0.02	0.02	0.03	0.05	99.78
160.55	45.56	40.02	14.12	0.06	0.06	0.03	0.06	99.90
162.47	45.50	40.06	14.10	0.07	0.07	0.03	0.05	99.89
164.63	45.54	40.00	14.18	0.09	0.10	0.03	0.05	100.00
166.55	45.40	39.94	14.13	0.08	0.09	0.03	0.05	99.73
168.57	45.47	39.94	14.11	0.10	0.10	0.03	0.06	99.82
170.54	45.42	39.90	14.14	0.12	0.12	0.03	0.06	99.81
172.48	45.38	39.94	14.16	0.13	0.13	0.03	0.07	99.84
174.60	45.44	39.94	14.24	0.11	0.11	0.04	0.05	99.94
176.64	45.39	39.94	14.24	0.14	0.14	0.03	0.05	99.93
178.58	45.39	39.93	14.23	0.14	0.14	0.04	0.06	99.91
180.62	45.49	39.97	14.24	0.09	0.09	0.03	0.05	99.97
182.45	45.49	40.01	14.22	0.05	0.05	0.03	0.06	99.91
184.68	44.56	40.40	14.00	0.05	0.05	0.51	0.06	99.63
192.62	45.42	40.01	14.14	0.01	0.01	0.03	0.05	99.68
194.57	45.41	39.99	14.32	0.01	0.01	0.03	0.05	99.82
196.59	45.39	39.93	14.23	0.01	0.01	0.03	0.05	99.65
198.63	45.39	40.01	14.21	0.02	0.02	0.03	0.04	99.71
200.57	45.45	39.92	14.26	0.09	0.09	0.03	0.06	99.90
202.61	45.38	39.90	14.22	0.10	0.10	0.03	0.05	99.79
204.73	45.43	39.89	14.18	0.07	0.07	0.03	0.06	99.73
206.58	45.42	39.89	14.19	0.10	0.10	0.03	0.06	99.79
208.62	45.38	39.99	14.20	0.12	0.13	0.03	0.07	99.93

210.65	45.45	39.96	14.19	0.08	0.07	0.03	0.06	99.84
212.68	45.39	40.04	14.17	0.03	0.04	0.03	0.05	99.75
214.62	45.36	39.99	14.21	0.04	0.04	0.03	0.06	99.75
216.57	45.37	40.00	14.16	0.05	0.05	0.03	0.06	99.73
218.80	45.43	40.01	14.19	0.07	0.07	0.03	0.06	99.86
220.62	45.39	39.95	14.17	0.14	0.15	0.04	0.08	99.92
222.57	45.30	39.83	14.20	0.18	0.18	0.03	0.08	99.79
224.59	45.28	39.88	14.17	0.16	0.17	0.04	0.08	99.78
226.71	45.38	39.92	14.20	0.18	0.18	0.04	0.09	99.98
228.57	45.34	39.84	14.20	0.15	0.15	0.04	0.09	99.82
230.70	45.36	40.01	14.19	0.07	0.06	0.03	0.09	99.82
232.67	45.31	39.85	14.19	0.12	0.13	0.04	0.12	99.75
234.79	45.24	39.85	14.24	0.17	0.18	0.04	0.13	99.85
236.73	45.29	39.81	14.23	0.18	0.18	0.04	0.15	99.88
238.75	45.28	39.82	14.30	0.16	0.17	0.04	0.20	99.97
240.62	44.83	39.49	14.44	0.18	0.19	0.20	0.64	99.98
252.75	45.06	39.84	14.29	0.01	0.00	0.05	0.41	99.66
254.88	45.04	39.83	14.21	0.01	0.01	0.03	0.25	99.37

Table B-6: Crystal 8 (Figure 3.2) after 10 days of high T dwell

Distance (um)	MgO WT%	SiO2 WT%	FeO WT%	P2O5 WT%	Al2O3 WT%	MnO WT%	CaO WT%	TOTAL
0.00	43.17	39.25	15.92	0.01	0.07	0.04	0.14	98.59
2.40	43.08	39.21	15.85	0.00	0.08	0.03	0.14	98.39
4.40	43.16	39.15	15.91	0.00	0.07	0.04	0.14	98.47
6.41	43.21	39.23	15.99	0.01	0.06	0.04	0.13	98.67
8.41	43.22	39.26	15.98	0.01	0.05	0.05	0.13	98.71
10.31	43.22	39.24	15.93	0.01	0.06	0.04	0.13	98.63
12.42	43.24	39.32	15.90	0.00	0.06	0.04	0.13	98.70
14.42	43.31	39.26	15.96	0.00	0.06	0.03	0.14	98.74
16.43	43.19	39.25	15.90	0.02	0.06	0.04	0.13	98.60
18.43	43.34	39.31	16.01	0.02	0.06	0.04	0.13	98.91
20.43	43.40	39.37	16.00	0.02	0.06	0.04	0.13	99.02
22.46	43.31	39.28	15.93	0.01	0.06	0.04	0.14	98.77
24.46	43.43	39.40	15.98	0.02	0.05	0.04	0.14	99.06
26.36	43.36	39.42	15.92	0.03	0.05	0.03	0.14	98.94
28.48	43.39	39.39	15.83	0.03	0.06	0.04	0.13	98.88
30.48	43.39	39.34	15.88	0.08	0.06	0.03	0.13	98.91
32.47	43.32	39.24	15.89	0.08	0.06	0.04	0.13	98.76

34.48	43.43	39.32	15.88	0.10	0.07	0.03	0.13	98.96
36.49	43.38	39.24	15.97	0.15	0.07	0.04	0.13	98.99
38.39	43.38	39.35	15.84	0.10	0.07	0.04	0.13	98.90
40.49	44.17	39.38	16.13	0.04	0.07	0.04	0.13	99.96
42.50	43.37	39.40	15.86	0.04	0.06	0.04	0.13	98.90

Table B-7: Crystal 9 (Figure 3.2) initial profile

Distance (um)	MgO WT%	SiO2 WT%	FeO WT%	P2O5 WT%	Al2O3 WT%	MnO WT%	CaO WT%	TOTALS
6.04	44.78	40.24	15.07	0.00	0.10	0.02	0.08	100.29
9.01	44.88	40.31	15.01	0.01	0.06	0.03	0.08	100.38
12.06	44.92	40.33	14.96	0.01	0.06	0.03	0.09	100.39
15.00	44.93	40.39	15.03	0.01	0.05	0.03	0.09	100.53
18.05	45.00	40.36	15.10	0.00	0.06	0.03	0.09	100.64
21.09	44.89	40.30	15.17	0.02	0.07	0.04	0.09	100.59
24.01	44.91	40.31	15.25	0.04	0.07	0.03	0.09	100.70
26.83	44.87	40.32	15.19	0.05	0.07	0.03	0.09	100.62
30.03	44.78	40.38	15.26	0.02	0.07	0.03	0.10	100.63
33.11	44.91	40.29	15.22	0.02	0.06	0.03	0.10	100.63
36.18	44.82	40.35	15.38	0.03	0.07	0.02	0.10	100.78
39.01	44.80	40.25	15.37	0.03	0.07	0.03	0.10	100.65
42.14	44.84	40.29	15.47	0.07	0.07	0.03	0.10	100.87
44.97	44.73	40.20	15.40	0.06	0.07	0.03	0.10	100.59
47.88	44.77	40.29	15.43	0.07	0.07	0.03	0.11	100.77
51.08	44.79	40.40	15.46	0.05	0.07	0.03	0.11	100.92
54.12	44.71	40.28	15.47	0.01	0.07	0.03	0.11	100.69
57.08	44.69	40.28	15.55	0.00	0.08	0.03	0.11	100.74
60.05	44.61	40.25	15.55	0.00	0.09	0.02	0.11	100.63
62.99	44.59	40.25	15.60	0.00	0.09	0.02	0.12	100.68
66.17	44.58	40.22	15.57	0.00	0.09	0.03	0.11	100.60
69.11	44.62	40.28	15.57	0.00	0.06	0.04	0.11	100.68
72.07	44.58	40.27	15.64	0.02	0.06	0.04	0.11	100.72
75.11	44.55	40.22	15.56	0.04	0.06	0.04	0.12	100.58
78.12	44.59	40.28	15.60	0.05	0.06	0.03	0.12	100.73
81.07	44.54	40.24	15.65	0.04	0.07	0.03	0.12	100.70
84.14	44.54	40.19	15.57	0.03	0.07	0.03	0.12	100.55
87.10	44.59	40.23	15.62	0.03	0.07	0.03	0.12	100.69
90.10	44.54	40.18	15.52	0.04	0.08	0.03	0.11	100.51
93.21	44.57	40.20	15.59	0.00	0.15	0.03	0.12	100.66

96.09	44.54	40.19	15.57	0.00	0.15	0.04	0.11	100.61
99.13	44.57	40.22	15.47	0.03	0.08	0.03	0.11	100.52
102.09	44.67	40.25	15.44	0.04	0.07	0.04	0.11	100.62
105.10	44.63	40.20	15.49	0.04	0.07	0.02	0.11	100.55

Table B-8: Crystal 9 (Figure 3.9) profile after 10-day dwell at high T

Distance (um)	MgO WT%	SiO2 WT%	FeO WT%	P2O5 WT%	Al2O3 WT%	CaO WT%	TOTAL
34.74	45.01	38.91	14.02	0.02	0.04	0.26	98.25
41.78	45.00	38.81	14.02	0.02	0.05	0.25	98.15
48.81	45.01	38.64	14.03	0.01	0.04	0.25	97.99
55.73	44.98	38.77	13.93	0.01	0.04	0.25	97.98
62.65	44.98	38.90	14.02	0.00	0.04	0.25	98.19
69.67	45.06	38.98	13.99	0.01	0.04	0.25	98.34
76.79	45.32	39.15	13.98	0.02	0.04	0.25	98.75
83.82	45.01	39.03	13.97	0.01	0.04	0.24	98.30
90.74	44.73	38.68	13.94	0.01	0.04	0.24	97.64
97.87	45.07	39.04	13.90	0.02	0.04	0.24	98.31
104.89	45.11	38.94	13.85	0.06	0.05	0.24	98.24
140.01	45.12	38.71	13.84	0.07	0.06	0.24	98.04
146.72	45.11	38.73	13.83	0.04	0.06	0.24	98.02
153.95	45.21	39.25	13.87	0.02	0.05	0.25	98.65
161.08	45.09	38.86	13.91	0.04	0.06	0.25	98.20
167.80	45.12	38.80	13.88	0.04	0.06	0.24	98.14
174.83	45.12	38.85	13.93	0.03	0.05	0.24	98.22
181.85	45.16	38.88	13.90	0.03	0.05	0.24	98.27
188.88	45.05	38.81	13.88	0.03	0.06	0.24	98.07
195.90	45.17	38.78	13.93	0.03	0.05	0.24	98.20
202.73	45.20	38.79	13.87	0.03	0.06	0.24	98.19
209.86	45.21	38.86	13.91	0.04	0.05	0.24	98.31
216.98	45.11	38.93	13.89	0.04	0.06	0.24	98.27
223.80	45.09	38.94	13.88	0.03	0.06	0.24	98.23
230.63	41.63	39.79	13.88	0.07	1.35	1.35	98.06
237.85	45.00	38.79	13.92	0.02	0.05	0.24	98.02
251.90	45.07	38.95	13.95	0.03	0.05	0.24	98.29
258.71	45.03	39.05	14.04	0.03	0.05	0.25	98.45
265.75	44.97	39.00	13.98	0.03	0.05	0.26	98.29

Appendix C: Chapter 4 Supplementary Material

Supplementary Figures:

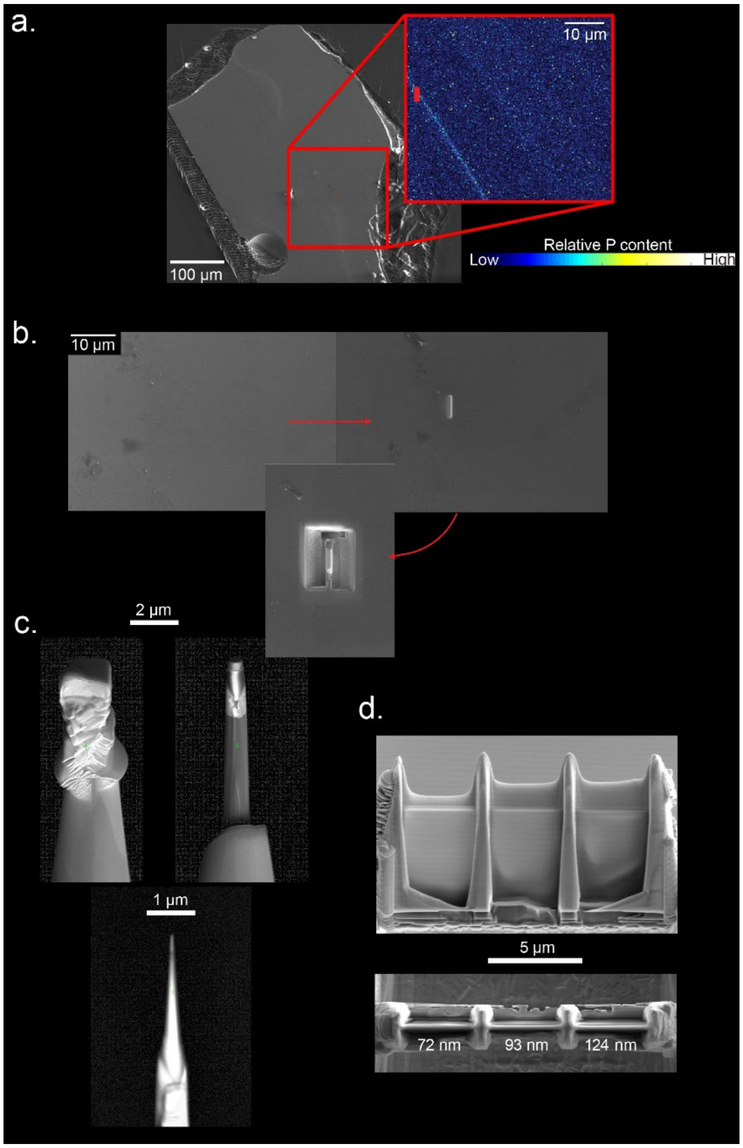

Figure C-1: Extraction of foils and needles. a. First, high resolution EPMA maps are made so it is possible to locate lamellae on FIB, and plan extraction location. b. Pt is deposited, first via electron beam, then Ga+ion bombardment. A foil is then carved out. c. for APT analysis, the foil is then attached with Pt to posts, and carved into the required needle shape. d. For TEM, the foil shape is maintained, but the foil is thinned. In this example, three different "windows" of varying thickness was made by K. Otahki.

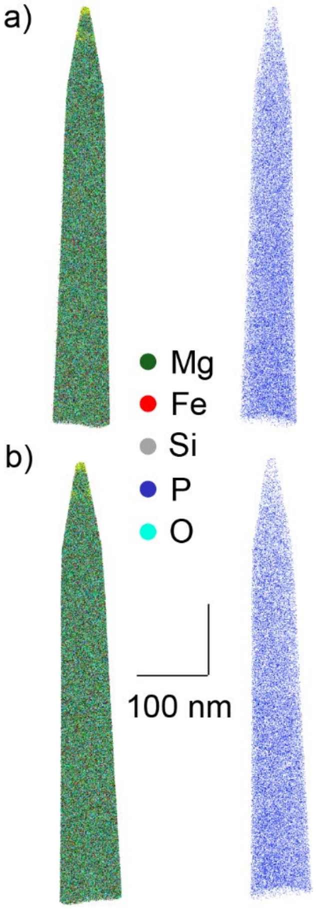

Figure C-2: Needles from the Pu’u’ō’ō sample.

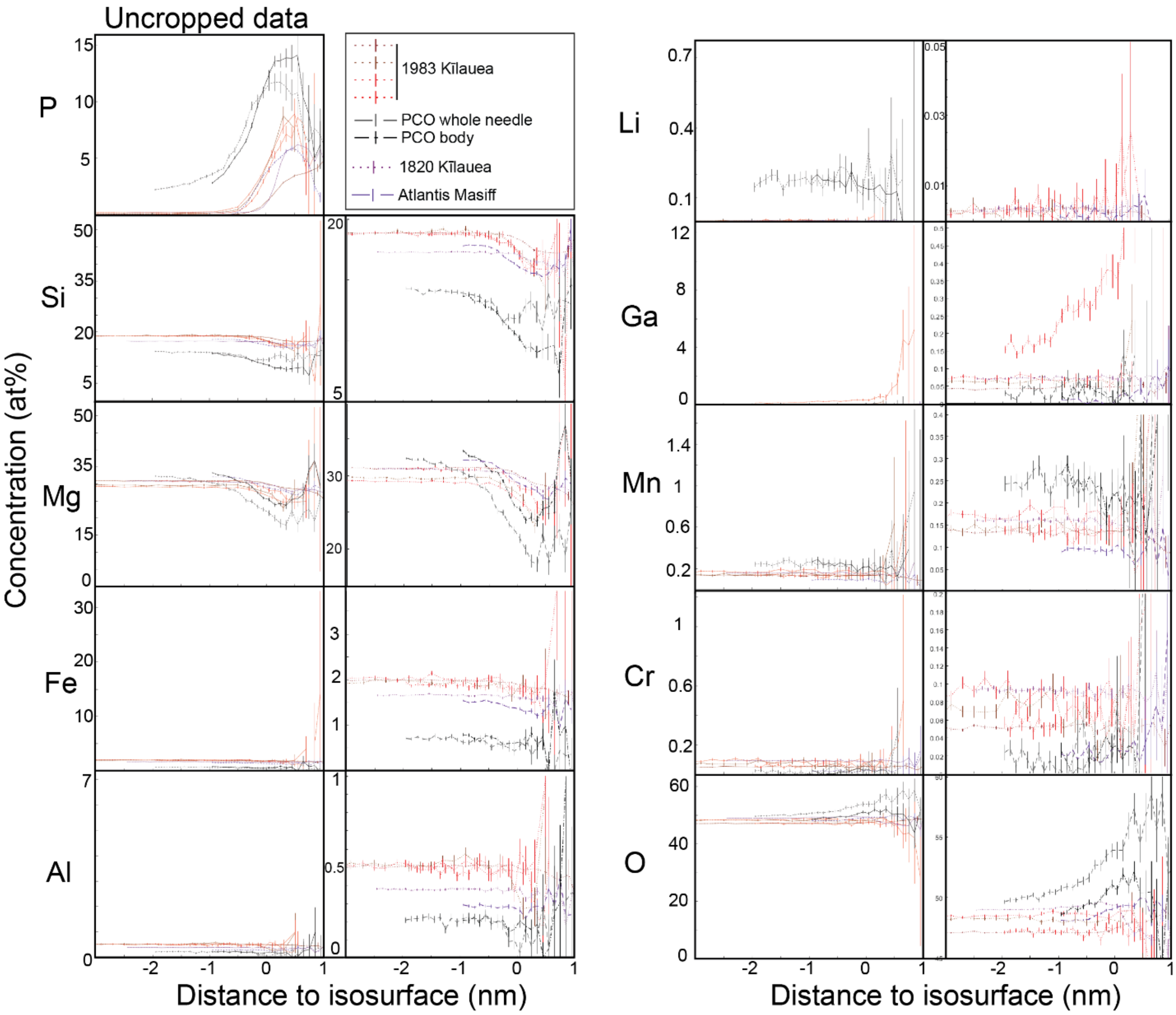

Figure C-3: Proxigrams for all (notable) elements detected. Note the general lack of significant correlation.

Supplementary Tables:

Table C-1: Compiled PCO EPMA data

P2O5	SiO2	MgO	FeO	Al2O3	Totals
1.13	39.35	49.57	8.94	0.18	99.16
0.97	39.81	50.34	8.69	0.05	99.87
0.87	39.88	50.37	8.63	0.04	99.79
0.96	39.83	50.23	8.59	0.03	99.63
1.13	39.68	50.17	8.59	0.03	99.59
1.17	39.69	50.09	8.59	0.03	99.56
1.09	39.81	50.16	8.57	0.03	99.66
1.14	39.77	50.20	8.57	0.04	99.72
1.25	39.71	50.08	8.56	0.06	99.66
1.17	39.73	50.00	8.57	0.06	99.52
1.19	39.75	49.99	8.54	0.05	99.53
1.35	39.67	50.05	8.55	0.05	99.66
1.75	39.21	49.88	8.62	0.07	99.52
2.13	38.62	49.54	8.97	0.12	99.39
3.08	37.65	48.95	9.01	0.23	98.92
3.28	37.13	47.79	8.93	0.76	97.89
3.14	38.23	49.91	8.51	0.17	99.96
2.60	38.68	50.09	8.40	0.05	99.83
1.55	39.58	50.33	8.47	0.03	99.96
1.39	39.65	50.11	8.49	0.03	99.67
1.37	39.69	50.05	8.53	0.03	99.66
1.36	39.61	50.03	8.55	0.03	99.58
1.36	39.62	50.03	8.53	0.03	99.57
1.34	39.60	49.86	8.54	0.03	99.37
1.34	39.55	49.88	8.55	0.03	99.36
1.36	39.56	49.72	8.55	0.03	99.22
1.36	39.62	49.88	8.55	0.04	99.45
1.40	39.64	49.83	8.60	0.07	99.54
1.52	38.72	48.94	9.21	0.46	98.84
2.05	38.96	49.44	8.58	0.09	99.12
3.16	38.08	49.30	8.44	0.06	99.04
3.41	37.82	49.22	8.38	0.08	98.91
3.00	37.91	49.14	8.38	0.44	98.87
1.17	39.03	49.44	8.55	1.00	99.18

0.63	37.31	48.41	8.98	2.83	98.15
3.63	38.08	44.82	9.09	5.25	100.87
5.14	37.82	47.57	8.43	1.58	100.54
4.97	37.91	48.29	8.43	1.47	101.07
0.83	33.89	43.64	10.64	9.67	98.68
1.97	37.31	47.54	9.02	2.70	98.54
2.60	38.12	48.70	8.47	0.66	98.56
2.66	38.44	49.02	8.35	0.13	98.60
2.63	38.46	49.12	8.37	0.05	98.63
2.25	38.78	49.12	8.47	0.05	98.67
2.15	38.93	49.12	8.51	0.05	98.76
2.15	38.86	49.09	8.51	0.05	98.65
3.40	37.63	48.84	8.47	0.05	98.38
4.90	36.35	48.54	8.34	0.06	98.17
6.11	35.27	48.31	8.21	0.05	97.96
6.29	35.20	48.26	8.24	0.06	98.05
5.65	35.69	48.35	8.26	0.06	98.01
4.93	36.32	48.44	8.30	0.06	98.04
3.63	37.42	48.69	8.37	0.06	98.17
2.47	38.60	49.16	8.45	0.05	98.74
2.00	39.09	49.32	8.44	0.05	98.90
2.25	39.07	49.31	8.41	0.05	99.09
2.34	39.27	49.41	8.37	0.05	99.45
2.49	40.19	49.84	8.30	0.06	100.89

Table C-2: Compiled Kilauea Iki EPMA data

P2O5	SiO2	MgO	FeO	Al2O3
0.01	38.53	37.19	24.51	0.00
0.01	38.07	36.78	24.31	0.00
0.01	38.13	36.88	24.17	0.00
0.01	38.10	36.94	24.13	0.01
0.01	38.15	37.08	24.01	0.01
0.01	38.17	37.16	23.93	0.01
0.01	38.11	37.22	23.83	0.01
0.01	38.14	37.30	23.66	0.01
0.01	38.21	37.49	23.50	0.01

0.01	38.18	37.51	23.36	0.01
0.20	37.99	37.47	23.36	0.04
0.20	38.09	37.58	23.20	0.03
0.02	38.29	37.79	23.12	0.02
0.01	38.30	37.93	22.99	0.02
0.00	38.32	38.09	22.77	0.02
0.01	38.34	38.21	22.66	0.02
0.00	38.43	38.37	22.54	0.02
0.00	38.47	38.48	22.42	0.02
0.01	38.52	38.66	22.24	0.02
0.02	38.52	38.75	22.09	0.02
0.03	38.57	38.81	21.99	0.02
0.10	38.51	38.87	21.92	0.02
0.03	38.63	38.97	21.79	0.02
0.02	38.63	39.07	21.70	0.02
0.03	38.64	39.18	21.69	0.02
0.04	38.68	39.25	21.61	0.02
0.01	38.67	39.33	21.51	0.02
0.01	38.74	39.34	21.46	0.02
0.02	38.66	39.49	21.35	0.02
0.02	38.75	39.56	21.33	0.02
0.03	38.77	39.63	21.27	0.02
0.02	38.85	39.67	21.22	0.02
0.01	38.81	39.76	21.20	0.02
0.05	38.79	39.78	21.13	0.02
0.14	38.69	39.72	21.04	0.02
0.08	38.68	39.72	20.95	0.02
0.07	38.78	39.82	20.99	0.02
0.03	38.81	39.80	20.98	0.02
0.01	38.83	39.88	20.96	0.02
0.02	38.83	39.94	20.91	0.02
0.01	38.83	39.95	20.92	0.02
0.08	38.76	39.85	20.82	0.02
0.03	38.77	39.94	20.85	0.02
0.04	38.79	39.96	20.88	0.02
0.09	38.74	39.92	20.82	0.02
0.06	38.71	39.86	20.72	0.02
0.04	38.82	40.00	20.80	0.02
0.04	38.78	39.97	20.81	0.02

0.01	38.81	39.98	20.74	0.02
0.01	38.76	40.01	20.77	0.02
0.01	38.77	40.02	20.77	0.02

Appendix D: Chapter 5 Supplementary Material

Supplementary Tables:

Table D-1: Acfer 094 chondrule 3

Distance (um)	Al2O3 WT%	MnO WT%	Cr2O3 WT%	Na2O WT%	SiO2 WT%	MgO WT%	FeO WT%	TiO2 WT%	NiO WT%	CaO WT%
5.07	0.07	0.09	0.46	0.00	43.01	56.77	0.83	0.01	0.01	0.28
5.88	0.02	0.09	0.44	0.00	42.80	56.60	0.72	0.01	0.00	0.29
6.87	0.01	0.08	0.43	0.00	42.79	56.70	0.70	0.01	0.01	0.29
7.87	0.01	0.08	0.41	0.00	42.79	56.62	0.70	0.00	0.01	0.29
8.94	0.01	0.08	0.40	0.00	42.85	56.79	0.69	0.02	0.00	0.29
10.07	0.03	0.07	0.39	0.00	42.80	56.66	0.67	0.02	0.01	0.29
10.96	0.10	0.07	0.39	0.00	42.78	56.61	0.66	0.04	0.01	0.29
11.96	0.10	0.06	0.37	0.00	42.69	56.60	0.63	0.04	0.01	0.30
12.96	0.08	0.06	0.37	0.00	42.76	56.66	0.62	0.03	0.00	0.30
13.96	0.07	0.05	0.35	0.00	42.84	56.79	0.62	0.04	0.00	0.30
15.16	0.06	0.05	0.34	0.00	42.83	56.73	0.61	0.03	0.01	0.30
16.17	0.06	0.05	0.34	0.00	42.64	56.53	0.62	0.03	0.01	0.30
17.09	nd	nd	nd	nd	nd	nd	nd	nd	nd	
18.11	nd	nd	nd	nd	nd	nd	nd	nd	nd	
19.13	nd	nd	nd	nd	nd	nd	nd	nd	nd	
20.04	0.04	0.04	0.34	0.00	43.03	57.00	0.59	0.03	0.01	
20.90	0.02	0.04	0.33	0.00	42.97	56.93	0.59	0.02	0.01	0.29
22.03	0.01	0.03	0.33	0.00	42.88	56.84	0.58	0.01	0.00	0.29
23.21	0.01	0.03	0.34	0.00	42.93	56.86	0.58	0.01	0.00	
24.09	0.01	0.03	0.34	0.00	42.82	56.84	0.58	0.02	0.01	0.29
25.02	0.01	0.03	0.33	0.00	42.92	56.97	0.57	0.02	0.00	0.29
25.94	0.01	0.04	0.34	0.00	42.97	56.99	0.58	0.02	0.00	0.29
27.01	0.01	0.04	0.34	0.00	42.86	56.77	0.58	0.01	0.01	0.29
28.21	0.01	0.04	0.34	0.00	42.83	56.82	0.58	0.02	0.01	
29.15	0.01	0.04	0.33	0.00	42.82	56.84	0.57	0.02	0.01	0.29
30.28	0.01	0.04	0.34	0.00	42.88	56.92	0.60	0.02	0.01	0.30
31.07	0.01	0.04	0.34	0.00	42.89	56.85	0.58	0.02	0.01	0.30
31.96	0.01	0.04	0.34	0.00	42.80	56.81	0.59	0.02	0.01	0.30
33.02	0.01	0.04	0.34	0.00	42.82	56.76	0.60	0.01	0.01	0.30
34.09	0.01	0.04	0.34	0.00	42.77	56.75	0.61	0.01	0.01	0.29
35.07	0.01	0.04	0.34	0.00	42.72	56.64	0.61	0.02	0.00	0.29
36.10	0.01	0.04	0.34	0.00	42.72	56.64	0.61	0.01	0.01	0.29

37.03	0.01	0.04	0.35	0.00	42.66	56.62	0.63	0.00	0.01	0.30
38.09	0.02	0.04	0.35	0.00	42.55	56.33	0.65	0.02	0.01	0.30

Table D-2: Acfer 094 chondrule 20

Distance (um)	Al2O3 WT%	MnO WT%	Cr2O3 WT%	SiO2 WT%	MgO WT%	Na2O WT%	FeO WT%	TiO2 WT%	CaO WT%
24.14	0.07	0.01	0.16	42.99	55.87	0.00	0.36	0.03	0.41
25.92	0.07	0.02	0.16	42.98	55.83	0.00	0.36	0.04	0.41
27.52	0.07	0.01	0.15	43.13	55.96	0.00	0.36	0.04	0.40
29.30	0.07	0.01	0.15	43.10	56.04	0.00	0.36	0.04	0.40
31.14	0.08	0.01	0.15	43.08	55.93	0.00	0.36	0.04	0.39
32.91	0.08	0.01	0.15	43.17	56.02	0.00	0.36	0.04	0.39
34.76	0.07	0.01	0.15	43.14	56.04	0.00	0.37	0.04	0.38
36.37	0.06	0.01	0.15	43.08	56.04	0.00	0.37	0.04	0.37
38.09	0.04	0.01	0.15	43.15	56.07	0.00	0.39	0.03	0.36
39.84	0.05	0.01	0.16	43.13	55.98	0.00	0.39	0.03	0.35
41.67	0.05	0.01	0.15	42.97	56.04	0.00	0.39	0.04	0.35
43.41	0.06	0.01	0.16	43.10	56.12	0.00	0.42	0.04	0.34
45.05	0.07	0.01	0.16	43.06	56.08	0.00	0.42	0.04	0.34
46.91	0.08	0.01	0.16	43.11	56.19	0.00	0.41	0.03	0.33
48.54	0.09	0.01	0.17	43.04	56.08	0.00	0.40	0.05	0.34
50.36	0.09	0.01	0.18	42.99	56.15	0.00	0.41	0.05	0.34
52.21	0.09	0.01	0.19	43.19	56.07	0.00	0.41	0.05	0.34
53.86	0.09	0.01	0.19	43.15	56.10	0.00	0.40	0.04	0.34
55.60	0.09	0.01	0.19	43.06	55.87	0.00	0.39	0.04	0.35
57.33	0.08	0.01	0.18	43.37	56.38	0.00	0.39	0.03	0.35
59.15	0.07	0.01	0.17	43.19	56.25	0.00	0.38	0.03	0.35
60.68	0.07	0.01	0.17	43.08	56.11	0.00	0.38	0.04	0.36
62.51	0.06	0.01	0.16	43.14	56.10	0.00	0.37	0.02	0.36
64.31	0.08	0.01	0.16	43.06	56.06	0.00	0.38	0.03	0.36
66.12	0.15	0.01	0.16	43.04	55.95	0.00	0.37	0.05	0.37
67.69	0.23	0.01	0.16	43.02	56.00	0.00	0.36	0.07	0.37
69.52	0.26	0.01	0.16	42.88	56.01	0.00	0.37	0.08	0.37
71.46	0.29	0.01	0.16	42.82	55.94	0.00	0.36	0.09	0.37
73.14	0.32	0.01	0.16	42.91	55.96	0.00	0.36	0.09	0.37
74.96	0.30	0.01	0.16	42.87	55.90	0.00	0.37	0.10	0.38
76.69	0.33	0.01	0.15	42.82	55.61	0.00	0.39	0.10	0.38
78.44	nd	nd	nd	nd	nd	nd	nd	nd	nd
80.06	0.29	0.01	0.15	42.55	55.41	0.00	0.56	0.09	0.39

81.81	0.27	0.01	0.15	43.01	55.89	0.00	0.41	0.08	0.39
83.54	0.12	0.01	0.14	43.03	55.97	0.00	0.42	0.04	0.38
85.31	0.12	0.01	0.13	42.63	55.26	0.00	0.45	0.05	0.38

Table D-3: Y81020 PO chondrule

Distance (um)	Al2O3 WT%	MnO WT%	Cr2O3 WT%	TiO2 WT%	CaO WT%
3.04	0.22	0.00	0.07	0.05	0.69
6.09	0.17	0.00	0.06	0.04	0.68
9.00	0.21	0.00	0.07	0.04	0.68
12.10	0.25	0.01	0.07	0.04	0.67
15.08	nd	nd	nd	nd	nd
18.28	0.22	0.00	0.07	0.05	0.54
21.02	0.23	0.00	0.08	0.04	0.40
24.11	0.07	0.00	0.07	0.01	0.28
27.10	0.03	0.01	0.07	0.00	0.28
30.21	0.03	0.01	0.07	0.02	0.32
33.08	0.19	0.01	0.08	0.05	0.43
36.17	0.25	0.00	0.09	0.04	0.56
39.12	0.20	0.01	0.09	0.04	0.60
42.16	0.18	0.01	0.10	0.03	0.61
45.11	0.21	0.02	0.13	0.05	0.59
48.20	0.21	0.03	0.20	0.06	0.48

Table D-4: Y81020 BO chondrule

Distance (um)	Al2O3 WT%	MnO WT%	Cr2O3 WT%	TiO2 WT%	CaO WT%
22.30	0.37	0.07	0.27	0.10	0.27
22.81	0.50	0.07	0.29	0.10	0.29
23.51	0.63	0.07	0.30	0.10	0.30
24.11	0.65	0.07	0.30	0.13	0.30
24.71	0.60	0.07	0.28	0.11	0.29

Table D-5: Semarkona PO chondrule

Distance (um)	Al2O3 WT%	MnO WT%	Cr2O3 WT%	SiO2 WT%	MgO WT%	FeO WT%	TiO2 WT%	CaO WT%
2.54	0.27	0.07	0.21	42.50	55.41	0.22	0.08	0.30
3.18	0.14	0.06	0.21	42.55	55.50	0.23	0.07	0.29
3.68	0.13	0.06	0.19	42.60	55.51	0.24	0.07	0.31
4.18	0.12	0.05	0.19	42.53	55.45	0.25	0.06	0.33
4.68	0.13	0.05	0.18	42.55	55.41	0.25	0.07	0.35
5.18	0.13	0.04	0.18	42.60	55.41	0.25	0.07	0.38
5.72	0.14	0.04	0.17	42.66	55.36	0.26	0.06	0.40
6.25	0.15	0.03	0.16	42.66	55.30	0.26	0.06	0.42
6.96	0.17	0.03	0.15	42.72	55.31	0.27	0.06	0.45
7.28	0.18	0.03	0.15	42.68	55.27	0.27	0.07	0.46
8.00	0.19	0.02	0.14	42.67	55.22	0.28	0.07	0.48
8.36	0.20	0.02	0.14	42.65	55.15	0.29	0.07	0.49
8.86	0.21	0.02	0.13	42.69	55.10	0.29	0.07	0.50
9.36	0.22	0.02	0.13	42.62	55.10	0.30	0.06	0.50
9.92	0.22	0.02	0.14	42.57	54.94	0.31	0.07	0.51
10.35	0.22	0.02	0.14	42.67	55.01	0.33	0.06	0.51
10.85	0.23	0.02	0.14	42.63	54.98	0.34	0.06	0.50
11.43	0.23	0.02	0.15	42.68	54.94	0.36	0.06	0.50
11.86	0.23	0.02	0.15	42.63	54.91	0.38	0.06	0.49
12.39	0.23	0.02	0.16	42.62	54.82	0.40	0.06	0.47
12.98	0.20	0.02	0.16	42.65	54.86	0.43	0.05	0.44
13.48	0.14	0.02	0.18	42.66	54.95	0.45	0.04	0.42
13.98	0.07	0.02	0.17	42.75	54.96	0.46	0.03	0.41
14.48	0.03	0.02	0.18	42.82	55.03	0.47	0.02	0.40
14.98	0.02	0.02	0.18	42.76	54.98	0.47	0.02	0.40
15.48	0.02	0.02	0.18	42.79	55.00	0.48	0.02	0.39
15.98	0.03	0.02	0.19	42.81	54.98	0.49	0.02	0.38
16.56	0.06	0.02	0.19	42.79	54.95	0.50	0.02	0.38
17.06	0.08	0.02	0.20	42.73	54.88	0.51	0.02	0.37
17.51	0.09	0.02	0.20	42.68	54.86	0.52	0.03	0.36
18.01	0.10	0.02	0.20	42.68	54.80	0.53	0.03	0.36
18.51	0.11	0.02	0.21	42.63	54.70	0.55	0.03	0.35
19.07	0.11	0.02	0.22	42.73	54.82	0.56	0.03	0.34
19.58	0.11	0.02	0.22	42.70	54.80	0.57	0.03	0.33
20.07	0.11	0.02	0.23	42.61	54.72	0.58	0.03	0.32
20.50	0.12	0.02	0.23	42.71	54.83	0.59	0.03	0.32
21.06	0.12	0.03	0.24	42.79	54.80	0.61	0.03	0.31
21.63	0.12	0.03	0.25	42.69	54.73	0.62	0.03	0.30

22.13	0.13	0.03	0.25	42.72	54.77	0.64	0.03	0.30
22.69	0.13	0.03	0.26	42.67	54.81	0.65	0.03	0.30
23.27	0.13	0.03	0.27	42.66	54.74	0.66	0.03	0.29
23.64	0.13	0.03	0.27	42.69	54.73	0.67	0.03	0.29

Table D-6: Semarkona BO chondrule

Distance (um)	Al2O3 WT%	MnO WT%	Cr2O3 WT%	SiO2 WT%	MgO WT%	FeO WT%	TiO2 WT%	CaO WT%
5.76	0.12	0.08	0.28	43.88	55.93	0.66	0.03	0.32
6.39	0.07	0.07	0.26	43.39	55.68	0.63	0.03	0.33
6.99	0.07	0.06	0.25	43.06	55.40	0.62	0.04	0.33
7.49	0.08	0.06	0.24	42.75	55.07	0.60	0.04	0.33
7.99	0.10	0.06	0.24	42.88	55.18	0.59	0.05	0.33
8.39	0.12	0.05	0.23	42.76	55.00	0.57	0.06	0.34
8.89	0.14	0.05	0.23	42.75	55.03	0.56	0.06	0.34
9.29	0.16	0.04	0.22	42.73	54.90	0.55	0.06	0.34
9.79	0.18	0.04	0.22	42.67	54.87	0.55	0.07	0.34
10.40	0.20	0.04	0.21	42.68	54.89	0.53	0.07	0.35
11.00	0.21	0.03	0.21	42.64	54.83	0.52	0.08	0.36
11.51	0.22	0.03	0.21	42.64	54.83	0.51	0.08	0.36
11.91	0.23	0.03	0.21	42.63	54.84	0.51	0.07	0.37
12.41	0.23	0.03	0.20	42.72	54.90	0.51	0.08	0.37
12.81	0.24	0.02	0.20	42.61	54.75	0.50	0.08	0.38
13.32	0.25	0.03	0.19	42.63	54.76	0.50	0.08	0.38
13.91	0.27	0.02	0.19	42.61	54.87	0.50	0.08	0.38
14.32	0.27	0.03	0.19	42.61	54.78	0.48	0.08	0.39
14.93	0.28	0.02	0.19	42.60	54.72	0.49	0.08	0.39
15.52	0.29	0.02	0.18	42.61	54.72	0.48	0.08	0.39
15.94	0.29	0.02	0.18	42.58	54.70	0.49	0.09	0.39
16.45	0.29	0.02	0.18	42.67	54.71	0.48	0.08	0.40
16.86	0.28	0.02	0.18	42.57	54.72	0.48	0.08	0.40
17.37	0.27	0.02	0.18	42.62	54.74	0.48	0.08	0.40
17.88	0.26	0.02	0.18	42.78	54.93	0.48	0.07	0.40
18.51	0.25	0.02	0.17	42.57	54.66	0.47	0.07	0.40
19.11	0.24	0.02	0.17	42.56	54.60	0.48	0.07	0.41
19.41	0.25	0.02	0.17	42.66	54.79	0.48	0.08	0.41
19.92	0.27	0.02	0.18	42.66	54.76	0.48	0.08	0.41
20.43	0.27	0.02	0.17	42.62	54.79	0.48	0.08	0.41
20.84	0.27	0.02	0.18	42.60	54.69	0.47	0.07	0.41

21.33	0.26	0.02	0.17	42.58	54.75	0.48	0.08	0.41
21.78	0.25	0.02	0.17	42.63	54.75	0.47	0.07	0.40
22.48	0.24	0.02	0.17	42.61	54.74	0.47	0.07	0.41
23.08	0.24	0.01	0.18	42.64	54.68	0.47	0.07	0.40
23.48	0.24	0.02	0.17	42.61	54.70	0.48	0.08	0.40
24.02	0.25	0.02	0.18	42.63	54.71	0.48	0.08	0.40
24.53	0.25	0.02	0.18	42.59	54.81	0.48	0.08	0.40
25.03	0.26	0.02	0.18	42.55	54.66	0.47	0.08	0.40
25.54	0.26	0.02	0.18	42.59	54.59	0.48	0.08	0.40
25.95	0.26	0.02	0.18	42.60	54.66	0.48	0.08	0.40
26.66	0.26	0.02	0.18	42.63	54.58	0.48	0.08	0.40
27.07	0.27	0.02	0.18	42.61	54.63	0.48	0.08	0.40
27.61	0.27	0.02	0.18	42.55	54.60	0.49	0.08	0.39
28.10	0.27	0.02	0.18	42.55	54.63	0.49	0.08	0.39
28.62	0.27	0.02	0.19	42.54	54.58	0.48	0.08	0.40
29.03	0.27	0.02	0.19	42.59	54.57	0.48	0.08	0.40
29.53	0.27	0.02	0.18	42.50	54.55	0.48	0.09	0.39
29.94	0.26	0.02	0.19	42.53	54.53	0.49	0.08	0.39
30.65	0.25	0.02	0.19	42.58	54.51	0.49	0.09	0.39
31.29	0.24	0.02	0.19	42.46	54.45	0.49	0.08	0.39

References:

Agrell, S. O., Charnley, N. R., & Chinner, O. A. (1998). *Phosphoran olivine from Pine Canyon, Piute Co., Utah* (Vol. 62, Issue 2). https://doi.org/https://doi.org/10.1180/002646198547620

Albert, H., Larrea, P., Costa, F., Widom, E., & Siebe, C. (2020). Crystals reveal magma convection and melt transport in dyke-fed eruptions. *Scientific Reports*, *10*(1), 1–10. https://doi.org/10.1038/s41598-020-68421-4

Armstrong, J. T. (1988). Quantitative analysis of silicates and oxide minerals comparison of Monte-Carlo, ZAF and procedures. In *Microbeam Analysis* (pp. 239–246).

Auxerre, M., Faure, F., & Lequin, D. (2022). The effects of superheating and cooling rate on olivine growth in chondritic liquid. *Meteoritics and Planetary Science*, *57*(8), 1474–1495. https://doi.org/10.1111/maps.13830

Barboni, M., Boehnke, P., Keller, B., Kohl, I. E., Schoene, B., Young, E. D., & McKeegan, K. D. (2017). Early formation of the Moon 4.51 billion years ago. *Science Advances*, *3*(1), e1602365. https://doi.org/10.1126/SCIADV.1602365

Barkla, C. G., & Sadler, C. A. (1909). LXIX. The absorption of Röntgen rays . *The London, Edinburgh, and Dublin Philosophical Magazine and Journal of Science*, *17*(101), 739–760. https://doi.org/10.1080/14786440508636650

Barnes, J. J., Tartèse, R., Anand, M., McCubbin, F. M., Franchi, I. A., Starkey, N. A., & Russell, S. S. (2014). The origin of water in the primitive Moon as revealed by the lunar highlands samples. *Earth and Planetary Science Letters*, *390*, 244–252. https://doi.org/10.1016/j.epsl.2014.01.015

Barth, A., Newcombe, M., Plank, T., Gonnermann, H., Hajimirza, S., Soto, G. J., Saballos, A., & Hauri, E. (2019). Magma decompression rate correlates with explosivity at basaltic volcanoes — Constraints from water diffusion in olivine. *Journal of Volcanology and Geothermal Research*, *387*. https://doi.org/10.1016/j.jvolgeores.2019.106664

Basaltic Volcanism Study project, B. (1981). *Basaltic Volcanism on the Terrestrial Planets* (1st ed.). Pergamon Press, Inc. https://doi.org/QE462.B3 B27

Baziotis, I., Xydous, S., Asimow, P. D., Mavrogonatos, C., Flemetakis, S., Klemme, S., & Berndt, J. (2019). The potential of phosphorus in clinopyroxene as a geospeedometer: Examples from mantle xenoliths. *Geochimica et Cosmochimica Acta*, *266*, 307–331. https://doi.org/10.1016/j.gca.2019.04.024

Bell, A. F., La Femina, P. C., Ruiz, M., Amelung, F., Bagnardi, M., Bean, C. J., Bernard, B., Ebinger, C., Gleeson, M., Grannell, J., Hernandez, S., Higgins, M., Liorzou, C., Lundgren, P., Meier, N. J., Möllhoff, M., Oliva, S. J., Ruiz, A. G., & Stock, M. J. (2021). Caldera resurgence during the 2018 eruption of Sierra Negra volcano, Galápagos Islands. *Nature Communications*, *12*(1). https://doi.org/10.1038/s41467-021-21596-4

Beno, C. J., Bowman, J. R., Loury, P. C., Tapanila, L. M., & Fernandez, D. P. (2020). Evidence for dendritic crystallization of forsterite olivine during contact metamorphism of siliceous dolostones, Alta stock aureole, Utah. *Contributions to Mineralogy and Petrology*, *175*(10). https://doi.org/10.1007/s00410-020-01734-9

Berry, A. J., Walker, A. M., Hermann, J., O'Neill, H. St. C., Foran, G. J., & Gale, J. D. (2007). Titanium substitution mechanisms in forsterite. *Chemical Geology*, *242*(1–2), 176–186. https://doi.org/10.1016/j.chemgeo.2007.03.010

Bindi, L., Feng, T., & Pasek, M. A. (2023). Routes to reduction of phosphate by high-energy events. *Communications Earth and Environment*, *4*(1). https://doi.org/10.1038/s43247-023-00736-2

Boesenberg, J. S., & Hewins, R. H. (2010). An experimental investigation into the metastable formation of phosphoran olivine and pyroxene. *Geochimica et Cosmochimica Acta*, *74*(6), 1923–1941. https://doi.org/10.1016/j.gca.2009.12.008

Borg, L. E., Cassata, W. S., Wimpenny, J., Gaffney, A. M., & Shearer, C. K. (2020). The formation and evolution of the Moon's crust inferred from the Sm-Nd isotopic systematics of highlands rocks. *Geochimica et Cosmochimica Acta*, *290*, 312–332. https://doi.org/10.1016/j.gca.2020.09.013

Borg, L. E., Connelly, J. N., Boyet, M., & Carlson, R. W. (2011). Chronological evidence that the Moon is either young or did not have a global magma ocean. *Nature*, *477*(7362), 70–72. https://doi.org/10.1038/nature10328

Borg, L. E., Connelly, J. N., Cassata, W. S., Gaffney, A. M., & Bizzarro, M. (2017). Chronologic implications for slow cooling of troctolite 76535 and temporal relationships between the Mg-suite and the ferroan anorthosite suite. *Geochimica et Cosmochimica Acta*, *201*, 377–391. https://doi.org/10.1016/j.gca.2016.11.021

Bowen, N. L. (1956). *The Evolution of Igneous Rocks* (2nd ed.). Dover.

Bradshaw, R. W., Kent, A. J. R., & Tepley, F. J. (2018). Chemical fingerprints and residence times of olivine in the 1959 Kilauea Iki eruption, Hawaii: Insights into picrite formation. *American Mineralogist*, *103*(11), 1812–1826. https://doi.org/10.2138/am-2018-6331

Burgess, K. D., & Cooper, R. F. (2013). Extended planar defects and the rapid incorporation of Ti4+ into olivine. *Contributions to Mineralogy and Petrology*, *166*(4), 1223–1233. https://doi.org/10.1007/s00410-013-0918-x

Buseck, P. R., & Clark, J. (1984). Zaisho—a pallasite containing pyroxene and phosphoran olivine. *Mineralogical Magazine*, *48*(347), 229–235. https://doi.org/10.1017/MINMAG.1984.048.347.06

Butler, P. (1973). Lunar Sample Information Catalog, Apollo 17. In M. B. Duke & W. B. McCown (Eds.), *Lunar Sample Information Catalog, Apollo 17*. Lunar Receiving Laboratory. https://books.google.com/books?hl=en&lr=&id=4JLnadvVEsEC&oi=fnd&pg=PA1&dq=Butler+P.+(1973)+Lunar+Sample+Information+Catalog+Apollo+17.+Lunar+Receiving+Laboratory.+MSC+03211+Curator%E2%80%99s+Catalog.+pp.+447&ots=_Fv7g8ufKi&sig=jg9j6r2GSHwxUpDl0BmrP94Lsp8#v=onepage&q=76535&f=false

Büttner, R., Zimanowski, B., Blumm, J., & Hagemann, L. (1998). Thermal conductivity of a volcanic rock material (olivine-melilitite) in the temperature range between 288 and 1470 K. *Journal of Volcanology and Geothermal Research*, *80*(3–4), 293–302. https://doi.org/10.1016/S0377-0273(97)00050-4

Chakraborty, S. (2008). Diffusion in solid silicates: A tool to track timescales of processes comes of age. *Annual Review of Earth and Planetary Sciences*, *36*, 153–190. https://doi.org/10.1146/annurev.earth.36.031207.124125

Chakraborty, S. (2010). Diffusion coefficients in olivine, wadsleyite and ringwoodite. *Reviews in Mineralogy and Geochemistry*, *72*, 603–639. https://doi.org/10.2138/rmg.2010.72.13

Chen, L., Liu, X., Wang, W.-(RZ), & Liu, J. (2023). Ultrahigh-Temperature Mafic Granulites in the Rauer Group, East Antarctica: Evidence from Conventional

Thermobarometry, Phase Equilibria Modeling, and Rare Earth Element Thermometry. *Journal of Petrology*, *64*(4), 1–28. https://doi.org/10.1093/petrology/egad014

Cherniak, D. J. (1995). Diffusion of lead in plagioclase and K-feldspar: an investigation using Rutherford Backscattering and Resonant Nuclear Reaction Analysis. *Contributions to Mineralogy and Petrology*, *120*(3–4), 358–371. https://doi.org/10.1007/BF00306513

Clarke, E., de Hoog, J. C. M., Kirstein, L. A., Harvey, J., & Debret, B. (2020). Metamorphic olivine records external fluid infiltration during serpentinite dehydration. *Geochemical Perspectives Letters*, *16*, 25–29. https://doi.org/10.7185/GEOCHEMLET.2039

Colson, R. O., McKay, G. A., & Taylor, L. A. (1988). Temperature and composition dependencies of trace element partitioning: Olivine/melt and low-Ca pyroxene/melt. *Geochimica et Cosmochimica Acta*, *52*(2), 539–553. https://doi.org/10.1016/0016-7037(88)90109-3

Condit, Ralph. H. (1985). An Approach to Analyzing Diffusion in Olivine. In *AGU Monographs: Point defects in minerals* (Vol. 31, pp. 106–115). AGU. https://doi.org/10.1029

Connelly, N. G., Damhus, T., Hartshorn, R. M., & Hutton, A. T. (2005). *NOMENCLATURE OF INORGANIC CHEMISTRY IUPAC Recommendations 2005*. International Union of Pure and Applied Chemistry.

Coogan, L. A., Hain, A., Stahl, S., & Chakraborty, S. (2005). Experimental determination of the diffusion coefficient for calcium in olivine between 900°C and 1500°C. *Geochimica et Cosmochimica Acta*, *69*(14), 3683–3694. https://doi.org/10.1016/J.GCA.2005.03.002

Costa, F., Chakraborty, S., & Dohmen, R. (2003). Diffusion coupling between trace and major elements and a model for calculation of magma residence times using plagioclase. *Geochimica et Cosmochimica Acta*, *67*(12), 2189–2200. https://doi.org/10.1016/S0016-7037(02)01345-5

Costa, F., Shea, T., & Ubide, T. (2020). Diffusion chronometry and the timescales of magmatic processes. *Nature Reviews Earth and Environment*, *1*(4), 201–214. https://doi.org/10.1038/s43017-020-0038-x

Cukjati, J. T., Cooper, R. F., Parman, S. W., Zhao, N., Akey, A. J., & Laiginhas, F. A. T. P. (2019). Differences in chemical thickness of grain and phase boundaries: an atom probe tomography study of experimentally deformed wehrlite. *Physics and Chemistry of Minerals*, *46*(9), 845–859. https://doi.org/10.1007/s00269-019-01045-x

Dana, E. S., & Ford, W. E. (1932). *A Textbook of Mineralogy with an extended treatise on Crystallography and Physical Mineralogy* (4th ed.). John Wiley & Sons, Inc.

de Maisonneuve, C. B., Costa, F., Huber, C., Vonlanthen, P., Bachmann, O., & Dungan, M. A. (2016). How do olivines record magmatic events? Insights from major and trace element zoning. *Contributions to Mineralogy and Petrology*, *171*(6), 1–20. https://doi.org/10.1007/s00410-016-1264-6

Deer, W. A., Howie, R. A., & Zussman, J. (1966). *An Introduction to the Rock Forming Minerals* (1st ed.). John Wiley & Sons, Inc.

Delano, J. W. (1986). Pristine lunar glasses: Criteria, data, and implications. *Journal of Geophysical Research: Solid Earth*, *91*(B4), 201–213. https://doi.org/10.1029/JB091IB04P0D201

Demidova, S. I., Ntaflos, T., & Brandstätter, F. (2018). P-bearing Olivines from the “Luna-20” Soil Samples, Their Sources and Possible Phosphorus Substitution Mechanisms in Lunar Olivine. *Petrology*, *26*(3), 317–332. https://doi.org/10.1134/S0869591118030037

Dodd, R. T. (1981). *Meteorites: A petrologic-chemical synthesis* (1st ed.). Cambridge University Press.

Dohmen, R. (2002). Si and O diffusion in olivine and implications for characterizing plastic flow in the mantle. *Geophysical Research Letters*, *29*(21), 2030. https://doi.org/10.1029/2002GL015480

Dohmen, R., & Chakraborty, S. (2007). Fe-Mg diffusion in olivine II: Point defect chemistry, change of diffusion mechanisms and a model for calculation of diffusion coefficients in natural olivine. *Physics and Chemistry of Minerals*, *34*(6), 409–430. https://doi.org/10.1007/S00269-007-0158-6/FIGURES/8

Dohmen, R., Kasemann, S. A., Coogan, L., & Chakraborty, S. (2010). Diffusion of Li in olivine. Part I: Experimental observations and a multi species diffusion model. *Geochimica et Cosmochimica Acta*, *74*(1), 274–292. https://doi.org/10.1016/j.gca.2009.10.016

Donaldson, C. H. (1976). An experimental investigation of olivine morphology. *Contributions to Mineralogy and Petrology*, *57*(2), 187–213. https://doi.org/10.1007/BF00405225

Drouin, M., Godard, M., Ildefonse, B., Bruguier, O., & Garrido, C. J. (2009). Geochemical and petrographic evidence for magmatic impregnation in the oceanic lithosphere at Atlantis Massif, Mid-Atlantic Ridge (IODP Hole U1309D, 30°N). *Chemical Geology*, *264*(1–4), 71–88. https://doi.org/10.1016/j.chemgeo.2009.02.013

Dunn, T. (1987). Partitioning of Hf, Lu, Ti, and Mn between olivine, clinopyroxene and basaltic liquid. *Contributions to Mineralogy and Petrology*, *96*(4), 476–484. https://doi.org/10.1007/BF01166692

Dymek, R., Albee, A., & Chodos, A. (1975). Comparative petrology of lunar cumulate rocks of possible primary origin. *Proc. Lunar Sci. Conf.*, *VI*(2617), 301–341.

Edmunson, E. J., & Cohen, B. A. (2009). Characterizing the effect of shock on isotopic ages II: Mg-suite troctolite major elements. *Meteoritical Society*, *72*, M09-0553–0460. https://ntrs.nasa.gov/search.jsp?R=20090033640

Elardo, S. M., Draper, D. S., & Shearer, C. K. (2011). Lunar Magma Ocean crystallization revisited: Bulk composition, early cumulate mineralogy, and the source regions of the highlands Mg-suite. *Geochimica et Cosmochimica Acta*, *75*(11), 3024–3045. https://doi.org/10.1016/j.gca.2011.02.033

Elardo, S. M., Laneuville, M., McCubbin, F. M., & Shearer, C. K. (2020). Early crust building enhanced on the Moon’s nearside by mantle melting-point depression. *Nature Geoscience*, *13*, 339–343. https://doi.org/10.1038/s41561-020-0559-4

Elardo, S. M., McCubbin, F. M., & Shearer, C. K. (2012). Chromite symplectites in Mg-suite troctolite 76535 as evidence for infiltration metasomatism of a lunar layered intrusion. *Geochimica et Cosmochimica Acta*, *87*, 154–177. https://doi.org/10.1016/j.gca.2012.03.030

Elardo, S. M., & Shearer, C. K. (2014). Magma chamber dynamics recorded by oscillatory zoning in pyroxene and olivine phenocrysts in basaltic lunar meteorite Northwest Africa 032. *American Mineralogist*, *99*(2–3), 355–368. https://doi.org/10.2138/am.2014.4552

Ellis, D. M., Draper, N. P., & Smith, H. (1981). Applied Regression Analysis. *Applied Statistics*, *17*(2), 8–9. https://doi.org/10.2307/2985274

Ersoy, Ö., Nikogosian, I. K., van Bergen, M. J., & Mason, P. R. D. (2019). Phosphorous incorporation in olivine crystallized from potassium-rich magmas. *Geochimica et Cosmochimica Acta*, *253*, 63–83. https://doi.org/10.1016/J.GCA.2019.03.012

Evans, T. M., Hugh, H. S., & Tuff, J. (2008). The influence of melt composition on the partitioning of REEs, Y, Sc, Zr and Al between forsterite and melt in the system CMAS. *Geochimica et Cosmochimica Acta*, *72*(23), 5708–5721. https://doi.org/10.1016/j.gca.2008.09.017

Faure, F., Auxerre, M., & Casola, V. (2022). Slow cooling during crystallisation of barred olivine chondrules. *Earth and Planetary Science Letters*, *593*. https://doi.org/10.1016/j.epsl.2022.117649

Faure, F., Trolliard, G., Nicollet, C., & Montel, J.-M. (2003). A developmental model of olivine morphology as a function of the cooling rate and the degree of undercooling. *Contributions to Mineralogy and Petrology*, *145*(2), 251–263. https://doi.org/10.1007/s00410-003-0449-y

Fick, A. (1855). Ueber Diffusion. *Annalen Der Physik*, *170*(1), 59–86. https://doi.org/10.1002/andp.18551700105

First, E., & Hammer, J. (2016). Igneous cooling history of olivine-phyric shergottite Yamato 980459 constrained by dynamic crystallization experiments. *Meteoritics and Planetary Science*, *51*(7), 1233–1255. https://doi.org/10.1111/maps.12659

Galy, A., Young, E. D., Ash, R. D., & O'Nions, R. K. (2000). The formation of chondrules at high gas pressures in the solar nebula. *Science*, *290*(5497), 1751–1753. https://doi.org/10.1126/science.290.5497.1751

Ganapathy, R., & Anders, E. (1974). Bulk compositions of the Moon and Earth, estimated from meteorites. *Proceedings of the Fifth Lunar Conference*, *2*, 1181–1206.

Garrick-Bethell, I., Weiss, B. P., Shuster, D. L., & Buz, J. (2009). Early Lunar Magnetism. *Science*, *323*(5912), 356–359. https://doi.org/10.1126/science.1166804

Geary, R. C. (1954). The Contiguity Ratio and Statistical Mapping. *The Incorporated Statistician*, *5*(3), 115–127. https://about.jstor.org/terms

Ghiorso, M. S., & Sack, R. O. (1995). Chemical mass transfer in magmatic processes IV. A revised and internally consistent thermodynamic model for the interpolation and extrapolation of liquid-solid equilibria in magmatic systems at elevated temperatures and pressures. *Contributions to Mineralogy and Petrology*, *119*(2), 197–212. https://doi.org/10.1007/BF00307281

Giuliani, A. (2018). Insights into kimberlite petrogenesis and mantle metasomatism from a review of the compositional zoning of olivine in kimberlites worldwide. *Lithos*, *312–313*, 322–342. https://doi.org/10.1016/j.lithos.2018.04.029

Gooley, R., Brett, R., Warner, J., & Smyth, J. R. (1974). A lunar rock of deep crustal origin: sample 76535. *Geochimica et Cosmochimica Acta*, *38*(9), 1329–1339. https://doi.org/10.1016/0016-7037(74)90091-X

Gose, J., Schmädicke, E., Markowitz, M., & Beran, A. (2010). OH point defects in olivine from Pakistan. *Mineralogy and Petrology*, *99*(1), 105–111. https://doi.org/10.1007/s00710-009-0095-9

Graham, A. (1985). Yamato 81020 and Yamato 82042; two new carbonaceous chondrites from Antarctica. *Meteoritics*, *20*(4), 654.

Grant, T. B., & Kohn, S. C. (2013). Phosphorus partitioning between olivine and melt: An experimental study in the system Mg2SiO4-Ca2Al2Si2O9-NaAlSi3O8-Mg3(PO4)2. *American Mineralogist*, *98*(10), 1860–1869. https://doi.org/10.2138/am.2013.4237

Grimes, C. B., John, B. E., Cheadle, M. J., & Wooden, J. L. (2008). Protracted construction of gabbroic crust at a slow spreading ridge: Constraints from 206Pb/238U zircon ages from Atlantis Massif and IODP Hole U1309D (30°N, MAR). *Geochemistry, Geophysics, Geosystems*, *9*(8). https://doi.org/10.1029/2008GC002063

Gross, J., Hilton, A., Prissel, T. C., Setera, J. B., Korotev, R. L., & Calzada-Diaz, A. (2020). Geochemistry and Petrogenesis of Northwest Africa 10401: A New Type of the Mg-Suite Rocks. *Journal of Geophysical Research: Planets*, *125*(5), e2019JE006225. https://doi.org/10.1029/2019JE006225

Grossman, J., & Brearley, A. (2005). The onset of metamorphism in ordinary and carbonaceous chondrites. *Meteoritics and Planetary Science*, *40*(1), 87–122. https://doi.org/10.1111/j.1945-5100.2005.tb00366.x

Grossman, L., Beckett, J. R., Fedkin, A., Simon, S., & Ciesla, F. (2008). Redox Conditions in the Solar Nebula: Observational, Experimental, and Theoretical Constraints. *Reviews in Mineralogy and Geochemistry*, *68*, 93–140.

Grove, T. L., Baker, M. B., & Kinzler, R. J. (1984). Coupled CaAl-NaSi diffusion in plagioclase feldspar: Experiments and applications to cooling rate speedometry. *Geochimica et Cosmochimica Acta*, *48*(10), 2113–2121. https://doi.org/10.1016/0016-7037(84)90391-0

Grove, T. L., Holbig, E. S., Barr, J. A., Till, C. B., & Krawczynski, M. J. (2013). Melts of garnet lherzolite: Experiments, models and comparison to melts of pyroxenite and carbonated lherzolite. *Contributions to Mineralogy and Petrology*, *166*(3), 887–910. https://doi.org/10.1007/s00410-013-0899-9

Grützner, T., Kohn, S. C., Bromiley, D. W., Rohrbach, A., Berndt, J., & Klemme, S. (2017). The storage capacity of fluorine in olivine and pyroxene under upper mantle conditions. *Geochimica et Cosmochimica Acta*, *208*, 160–170. https://doi.org/10.1016/j.gca.2017.03.043

Gualda, G. A. R., Ghiorso, M. S., Lemons, R. v, & Carley, T. L. (2012). Rhyolite-MELTS: a Modified Calibration of MELTS Optimized for Silica-rich, Fluid-bearing Magmatic Systems. *Journal of Petrology*, *53*(5), 875–890. https://doi.org/10.1093/petrology/egr080

Hammer, J., Jacob, S., Welsch, B., Hellebrand, E., & Sinton, J. (2016). Clinopyroxene in postshield Haleakala ankaramite: 1. Efficacy of thermobarometry. *Contributions to Mineralogy and Petrology*, *171*(1), 1–23. https://doi.org/10.1007/s00410-015-1212-x

Hartman, P. (1969). Can Ti 4+ replace Si 4+ in silicates? *Mineralogical Magazine*, *37*(287), 366–369. https://doi.org/10.1180/minmag.1969.037.287.09

Hellebrand, E., Welsch, B. T., & Hammer, J. E. (2013). High Melt Porosity in the Lower Oceanic Crust Inferred from Phosphorus Zoning in Olivine. *AGU Fall Meeting, V24A-06*. https://ui.adsabs.harvard.edu/abs/2013AGUFM.V24A..06H/abstract

Hellman, O. C., Vandenbroucke, J. A., Rüsing, J., Isheim, D., & Seidman, D. N. (2000). Analysis of Three-dimensional Atom-probe Data by the Proximity Histogram. *Microscopy and Microanalysis*, *6*(5), 437–444. https://doi.org/10.1007/S100050010051

Helz, R. T. (1987). Differentiation behaviour of Kilauea Iki lava lake, Kilauea volcano, Hawaii: an overview of past and current work. *Magmatic Processes: Physicochemical Principles*, *January 1987*, 241–258.

Helz, R. T. (2020). Major-Element Compositional Data and Thermal Data for Drill Core f rom Kīlauea Iki Lava Lake, Plus Analyses of Glasses from Scoria of the 1959 Summit Eruption of Kīlauea Volcano, Hawaii. *U.S. Geological Survey Open File Report*, *1012*, 1–54.

Henderson, Knight, Redfern, & Wood. (1996). High-Temperature Study of Octahedral Cation Exchange in Olivine by Neutron Powder Diffraction. *Science*, *271*, 1713–1715.

Hess, P. C. (1994). Petrogenesis of lunar troctolites. *Journal of Geophysical Research*, *99*(E9), 19083–19093. https://doi.org/10.1029/94je01868

Hess, P. C., Rutherford, M. J., & Campbell, H. W. (1978). Ilmenite Crystallization in Nonmare Basalt: Genesis of KREEP and High-Ti Mare Basalt. *Proc. Lunar Planet. Sci. Conf*, *9*, 705–724.

Hewins, R. H. (1983). Dynamic Crystallization Experiments as Constraints on Chondrule Genesis. In King (Ed.), *Chondrules and Their Origins* (pp. 122–133). Lunar Planetary Institute.

Hillier, J., & Ramberg, E. G. (1947). The Magnetic Electron Microscope Objective: Contour Phenomena and the Attainment of High Resolving Power. *Journal of Applied Physics*, *18*(1), 48–71. https://doi.org/10.1063/1.1697554

Houlier, B., Cheraghmakani, M., & Jaoul, O. (1990). Silicon diffusion in San Carlos olivine. *Physics of the Earth and Planetary Interiors*, *62*(3–4), 329–340. https://doi.org/10.1016/0031-9201(90)90177-Y

Ito, M., & Ganguly, J. (2006). Diffusion kinetics of Cr in olivine and 53Mn-53Cr thermochronology of early solar system objects. *Geochimica et Cosmochimica Acta, 70*(3), 799–809. https://doi.org/10.1016/j.gca.2005.09.020

Izaki, M. (2010). Electrodeposition of Iron and Iron Alloys. In M. Schlesinger & M. Paunovic (Eds.), *Modern Electroplating* (5th ed., pp. 309–326). John Wiley & Sons, Inc.

Jarosewich, E., Nelen, J. A., & Norberg, J. A. (1980). Reference Samples for Electron Microprobe Analysis. *Geostandards Newsletter*, *4*, 43–47.

Johnson, M., Dungan, M. A., & Vance, J. A. (1977). Stable isotope compositions of olivine and dolomite in peridotites formed by deserpentinization, Darrington area, North Cascades, Washington. *Geochimica et Cosmochimica Acta*, *41*(3), 431–435. https://doi.org/10.1016/0016-7037(77)90272-1

Kaye, G. W. C. (1909). The Emission and Transmission of Roentgen Rays. *Philosophical Transactions of the Royal Society of London*, *209*(441–458), 123–151. https://doi.org/10.1259/arr.1909.0156

Kelemen, P. B., Kikawa, E., Miller, D. J., & et al. (2004). *Proceedings of the Ocean Drilling Program, 209 Initial Reports* (P. B. Kelemen, E. Kikawa, & D. J. Miller, Eds.; Vol. 209). Ocean Drilling Program. https://doi.org/10.2973/odp.proc.ir.209.2004

Kimura, T., Nishida, K., & Tanuma, S. (2006). Spatial resolution of a wavelength-dispersive electron probe microanalyzer equipped with a thermal field emission gun. *Microchimica Acta*, *155*(1–2), 175–178. https://doi.org/10.1007/s00604-006-0538-5

Kingery, W. D., Bowen, H. K., & Uhlmann, D. R. (1976). *Introduction to Ceramics* (E. Burke, B. Chalmers, & J. Krumhansl, Eds.). John Wiley & Sons, Inc.

Konzett, J., Hauzenberger, C., Krenn, K., Joachim-Mrosko, B., Stalder, R., Gröbner, K., Sieberer, A. K., Hoang, N., & Khoi, N. N. (2020). Neogene metasomatism in the subcontinental lithosphere beneath SE Asia—evidence from modal and cryptic phosphorus enrichment in peridotites and pyroxenites from southern Laos. *Journal of Petrology*, *60*(12), 2413–2448. https://doi.org/10.1093/petrology/egaa013

Krawczynski, M. J., & Grove, T. L. (2012). Experimental investigation of the influence of oxygen fugacity on the source depths for high titanium lunar ultramafic magmas. *Geochimica et Cosmochimica Acta*, *79*, 1–19. https://doi.org/10.1016/j.gca.2011.10.043

Kröger, F. A. (1985). Point Defects in Solids: Physics, Chemistry, and Thermodynamics. *Geophysical Monograph: Point Defects in Minerals*, *31*(1), 1–17.

Kröger, F. A., & Vink, H. J. (1956). Relations between the Concentrations of Imperfections in Crystalline Solids. *Solid State Physics*, *3*, 306–435.

Krot, A. N., Keil, K., Scott, E. R. D., Goodrich, C. A., & Weisberg, M. K. (2014). Classification of Meteorites and Their Genetic Relationships. In *Treatise on Geochemistry* (Vol. 1, pp. 1–63). Elsevier. https://doi.org/10.1016/B978-0-08-095975-7.00102-9

Lanari, P., Vidal, O., De Andrade, V., Dubacq, B., Lewin, E., Grosch, E. G., & Schwartz, S. (2014). XMapTools: A MATLAB©-based program for electron microprobe X-ray image processing and geothermobarometry. *Computers & Geosciences*, *62*, 227–240. https://doi.org/10.1016/j.cageo.2013.08.010

Leeman, W. P., & Scheidegger, K. F. (1977). Olivine/liquid distribution coefficients and a test for crystal-liquid equilibrium. *Earth and Planetary Science Letters*, *35*(2), 247–257. https://doi.org/10.1016/0012-821X(77)90128-5

Li, B., Ge, J., & Zhang, B. (2018). Diffusion in garnet: a review. *Acta Geochimica*, *37*(1), 19–31. https://doi.org/10.1007/s11631-017-0187-x

Libourel, G., & Portail, M. (2018). Chondrules as direct thermochemical sensors of solar protoplanetary disk gas. *Science Advances*, *4*(7). https://doi.org/10.1126/sciadv.aar3321

Longhi, J. (1981). Preliminary modeling of high pressure partial melting: Implications for early lunar differentiation. *Proc. Lunar. Planet. Sci*, *12*(B), 1001–1018.

Luhr, J. F. (2001). Glass inclusions and melt volatile contents at Parícutin Volcano, Mexico. *Contributions to Mineralogy and Petrology*, *142*(3), 261–283. https://doi.org/10.1007/s004100100293

Lynn, K. J., Garcia, M. O., & Shea, T. (2020). Phosphorus Coupling Obfuscates Lithium Geospeedometry in Olivine. *Frontiers in Earth Science*, *8*(May). https://doi.org/10.3389/feart.2020.00135

Lynn, K. J., Garcia, M. O., Shea, T., Costa, F., & Swanson, D. A. (2017). Timescales of mixing and storage for Keanakākoʻi Tephra magmas (1500–1820 C.E.), Kīlauea

Volcano, Hawai'i. *Contributions to Mineralogy and Petrology*, *172*(9). https://doi.org/10.1007/s00410-017-1395-4

Manzini, M., Bouvier, A. S., Baumgartner, L. P., Müntener, O., Rose-Koga, E. F., Schiano, P., Escrig, S., Meibom, A., & Shimizu, N. (2017). Weekly to monthly time scale of melt inclusion entrapment prior to eruption recorded by phosphorus distribution in olivine from mid-ocean ridges. *Geology*, *45*(12), 1059–1062. https://doi.org/10.1130/G39463.1

Marrocchi, Y., Euverte, R., Villeneuve, J., Batanova, V., Welsch, B., Ferrière, L., & Jacquet, E. (2019). Formation of CV chondrules by recycling of amoeboid olivine aggregate-like precursors. *Geochimica et Cosmochimica Acta*, *247*, 121–141. https://doi.org/10.1016/j.gca.2018.12.038

Maurice, M., Tosi, N., Schwinger, S., Breuer, D., & Kleine, T. (2020). A long-lived magma ocean on a young Moon. *Science Advances*, *6*(28), eaba8949. https://doi.org/10.1126/SCIADV.ABA8949

McBirney, A. R., & Noyes, R. M. (1979). Crystallization and Layering of the Skaergaard Intrusion. *Journal of Petrology*, *20*(3), 487–554. https://doi.org/10.1093/petrology/20.3.487

McCallum, I. S. (1983). Formation of Mg-Rich Pristine Rocks by Crustal Metasomatism. *Lunar and Planetary Science Conference*, *XIV*, 473–474.

McCallum, I. S., Domeneghetti, M. C., Schwartz, J. M., Mullen, E. K., Zema, M., Cámara, F., McCammon, C., & Ganguly, J. (2006). Cooling history of lunar Mg-suite gabbronorite 76255, troctolite 76535 and Stillwater pyroxenite SC-936: The record in exsolution and ordering in pyroxenes. *Geochimica et Cosmochimica Acta*, *70*(24), 6068–6078. https://doi.org/10.1016/j.gca.2006.08.009

McCallum, I. S., & O'Brien, H. E. (1996). Stratigraphy of the lunar highland crust: Depths of burial of lunar samples from cooling-rate studies. *American Mineralogist*, *81*(9–10), 1166–1175. https://doi.org/10.2138/am-1996-9-1015

McCanta, M. C., Beckett, J. R., & Stolper, E. M. (2016). Correlations and zoning patterns of phosphorus and chromium in olivine from H chondrites and the LL chondrite Semarkona. *Meteoritics & Planetary Science*, *51*(3), 520–546. https://doi.org/10.1111/MAPS.12604

McCarthy, A., Chelle-Michou, C., Blundy, J. D., Vonlanthen, P., Meibom, A., & Escrig, S. (2020). Taking the pulse of volcanic eruptions using plagioclase glomerocrysts. *Earth and Planetary Science Letters*, *552*, 116596. https://doi.org/10.1016/j.epsl.2020.116596

McSween, H. Y. (1999). *Meteorites and their Parent Planets* (2nd ed.). Cambridge University Press.

Milman-Barris, M. S., Beckett, J. R., Baker, M. B., Hofmann, A. E., Morgan, Z., Crowley, M. R., Vielzeuf, D., & Stolper, E. (2008). Zoning of phosphorus in igneous olivine. *Contributions to Mineralogy and Petrology*, *155*(6), 739–765. https://doi.org/10.1007/s00410-007-0268-7

Miyamoto, M., Mikouchi, T., & Jones, R. H. (2009). Cooling rates of porphyritic olivine chondrules in the Semarkona (LL3.00) ordinary chondrite: A model for diffusional equilibration of olivine during fractional crystallization. In *Meteoritics & Planetary Science* (Vol. 44). http://meteoritics.org

Moran, P. A. P. (1954). Some Experiments on the Prediction of Sunspot Numbers. *Royal Statistical Society*, *16*(1), 112–117. https://www-jstor-org.eres.library.manoa.hawaii.edu/stable/2984014?seq=1

Moreau, P., Guyomard, D., Gaubicher, J., & Boucher, F. (2010). Structure and stability of sodium intercalated phases in olivine FePO 4. *Chemistry of Materials*, *22*(14), 4126–4128. https://doi.org/10.1021/cm101377h

Morioka, M. (1981). Cation diffusion in olivine-II. Ni-Mg, Mn-Mg, Mg and Ca. *Geochimica et Cosmochimica Acta*, *45*(9), 1573–1580. https://doi.org/10.1016/0016-7037(81)90286-6

Morse, S. A. (2015). Kiglapait Intrusion, Labrador. In *Springer Geology* (pp. 589–648). Springer. https://doi.org/10.1007/978-94-017-9652-1_13

Mourey, A. J., Shea, T., & Hammer, J. E. (2023). Preservation of Magma Recharge Signatures in Kīlauea Olivine During Protracted Storage. *Journal of Geophysical Research: Solid Earth*, *128*(1). https://doi.org/10.1029/2022JB025523

Mutch, E. J. F., Maclennan, J., Shorttle, O., Edmonds, M., & Rudge, J. F. (2019). Rapid transcrustal magma movement under Iceland. *Nature Geoscience 2019 12:7*, *12*(7), 569–574. https://doi.org/10.1038/s41561-019-0376-9

Nakamura, A., & Schmalzried, H. (1983). On the nonstoichiometry and point defects of olivine. *Physics and Chemistry of Minerals*, *10*(1), 27–37. https://doi.org/10.1007/BF01204323

Nelson, Hammer, J. E., Shea, T., Hellebrand, E., & Jeffrey Taylor, G. (2021). Chemical heterogeneities reveal early rapid cooling of Apollo Troctolite 76535. *Nature Communications 2021 12:1*, *12*(1), 1–9. https://doi.org/10.1038/s41467-021-26841-4

Nelson, W., Akey, A., Hammer, J., & Parman, S. (2022, June 2). Atom by Atom: Investigating phosphorus in olivine using atom probe tomography. *Goldschmidt2022 Abstracts*. https://doi.org/10.46427/gold2022.12543

Nikogosyan, I. K., & Sobolev, A. V. (1997). Ion-microprobe analysis of melt inclusions in olivine: experience in estimating the melt-olivine distribution coefficients of impurity elements. *Geokhimiya*, *1*(2), 149–157.

Norman, M. D., Taylor, L. A., Shih, C. Y., & Nyquist, L. E. (2016). Crystal accumulation in a 4.2 Ga lunar impact melt. *Geochimica et Cosmochimica Acta*, *172*, 410–429. https://doi.org/10.1016/j.gca.2015.09.021

O'Driscoll, B., Emeleus, C. H., Donaldson, C. H., & Daly, J. S. (2010). Cr-spinel Seam Petrogenesis in the Rum Layered Suite, NW Scotland: Cumulate Assimilation and in situ Crystallization in a Deforming Crystal Mush. *Journal of Petrology*, *51*(6), 1171–1201. https://doi.org/10.1093/petrology/egq013

O'Sullivan, K. M., & Neal, C. R. (2013). Crystal stratigraphy of lunar troctolite 76535: Implications for Mg-suite origins and evolution. *Proc. Lunar Sci. Conf.*, *XLIV*, Abstract-2658. https://ui.adsabs.harvard.edu/abs/2013LPI....44.2658O/abstract

Papike, J. J., Fowler, G. W., Shearer, C. K., & Layne, G. D. (1996). Ion microprobe investigation of plagioclase and orthopyroxene from lunar Mg-suite norites: Implications for calculating parental melt REE concentrations and for assessing post crystallization REE redistribution. *Geochimica et Cosmochimica Acta*, *60*(20), 3967–3978. https://doi.org/10.1016/0016-7037(96)00212-8

Papike, J. J., Ryder, G., & Shearer, C. K. (1998). Lunar Samples. *Reviews in Mineralogy and Geochemistry*, *36*, 1–234.

Pariso, J. E., Rommevaux, C., & Sempere, J. C. (1996). Three-dimensional inversion of marine magnetic anomalies: Implications for crustal accretion along the Mid-

Atlantic Ridge (28°-31°30′ N). *Marine Geophysical Research*, *18*(1), 85–101. https://doi.org/10.1007/BF00286204

Pasquale, V., Verdoya, M., & Chiozzi, P. (2015). Measurements of rock thermal conductivity with a transient divided bar. *Geothermics*, *53*, 183–189. https://doi.org/10.1016/j.geothermics.2014.05.008

Petry, C., Chakraborty, S., & Palme, H. (2004). Experimental determination of Ni diffusion coefficients in olivine and their dependence on temperature, composition, oxygen fugacity, and crystallographic orientation. *Geochimica et Cosmochimica Acta*, *68*(20), 4179–4188. https://doi.org/10.1016/j.gca.2004.02.024

Piralla, M., Villeneuve, J., Batanova, V., Jacquet, E., & Marrocchi, Y. (2021). Conditions of chondrule formation in ordinary chondrites. *Geochimica et Cosmochimica Acta*, *313*, 295–312. https://doi.org/10.1016/j.gca.2021.08.007

Prissel, T. C., & Gross, J. (2020). On the petrogenesis of lunar troctolites: New insights into cumulate mantle overturn & mantle exposures in impact basins. *Earth and Planetary Science Letters*, *551*, 116531. https://doi.org/10.1016/j.epsl.2020.116531

Prissel, T. C., Parman, S. W., Jackson, C. R. M., Rutherford, M. J., Hess, P. C., Head, J. W., Cheek, L., Dhingra, D., & Pieters, C. M. (2014). Pink Moon: The petrogenesis of pink spinel anorthosites and implications concerning Mg-suite magmatism. *Earth and Planetary Science Letters*, *403*, 144–156. https://doi.org/10.1016/j.epsl.2014.06.027

Putirka. (2016). Amphibole thermometers and barometers for igneous systems and some implications for eruption mechanisms of felsic magmas at arc volcanoes. *American Mineralogist*, *101*(4), 841–858. https://doi.org/10.2138/am-2016-5506

Putirka, K. D. (2008). Thermometers and Barometers for Volcanic Systems. *Reviews in Mineralogy and Geochemistry*, *69*(1), 61–120. https://doi.org/10.2138/rmg.2008.69.3

Raedeke, L. , D., & McCallum, I. , S. (1980). A Comparison of Fractionation Trends in the Lunar Crust and the Stillwater Complex. *Proc. Conf. Lunar Highlands Crust*, 133–153. http://articles.adsabs.harvard.edu/cgi-bin/nph-iarticle_query?1980luhc.conf..133R&defaultprint=YES&filetype=.pdf

Rapp, J. F., & Draper, D. S. (2018). Fractional crystallization of the lunar magma ocean: Updating the dominant paradigm. *Meteoritics and Planetary Science*, *53*(7), 1432–1455. https://doi.org/10.1111/maps.13086

Reddy, S. M., Saxey, D. W., Rickard, W. D. A., Fougerouse, D., Montalvo, S. D., Verberne, R., & Van Riessen, A. (2020). *GGR Cutting-Edge Review Atom Probe Tomography: Development and Application to the Geosciences*. https://doi.org/10.1111/ggr.12313

Reed, S. J. B. (1993). *Electron Microprobe Analysis* (2nd ed.). Cambridge University Press.

Renna, M. R., & Tribuzio, R. (2011). Olivine-rich Troctolites from Ligurian Ophiolites (Italy): Evidence for Impregnation of Replacive Mantle Conduits by MORB-type

Melts. *Journal of Petrology*, *52*(9), 1763–1790. https://doi.org/10.1093/petrology/egr029

Renna, M. R., Tribuzio, R., Sanfilippo, A., & Thirlwall, M. (2018). Role of melting process and melt–rock reaction in the formation of Jurassic MORB-type basalts (Alpine ophiolites). *Contributions to Mineralogy and Petrology*, *173*(4), 1–21. https://doi.org/10.1007/s00410-018-1456-3

Ringwood, A. E., Kesson, S. E., Ringwood, A. E., & Kesson, S. E. (1976). A dynamic model for mare basalt petrogenesis. In *LPSC* (Vol. 2). https://ui.adsabs.harvard.edu/abs/1976LPSC....7.1697R/abstract

Riviere, J.-P. (1995). Radiation Induced Point Defects and Diffusion. In *Application of Particle and Laser Beams in Materials Technology* (pp. 53–76). Springer Netherlands. https://doi.org/10.1007/978-94-015-8459-3_4

Robie, R. A., Hemingway, B. S., & Wilson, W. H. (1978). Low-temperature heat capacities and entropies of feldspar glasses and of anorthite. *American Mineralogist*, *63*(1–2), 109–123. https://pubs.geoscienceworld.org/msa/ammin/article-abstract/63/1-2/109/40845/Low-temperature-heat-capacities-and-entropies-of?redirectedFrom=fulltext

Russell, S. S., Connolly, H. C., & Krot, A. N. (2018). *Chondrules Records of the Protoplanetary Disk* (S. S. Russell, H. C. Connolly Jr., & A. N. Krot, Eds.). Cambridge University Press. https://doi.org/10.1017/9781108284073

Shea, T., Hammer, J. E., Hellebrand, E., Mourey, A. J., Costa, F., First, E. C., Lynn, K. J., & Melnik, O. (2019). Phosphorus and aluminum zoning in olivine: contrasting behavior of two nominally incompatible trace elements. *Contributions to Mineralogy and Petrology*, *174*(10), 85. https://doi.org/10.1007/s00410-019-1618-y

Shea, T., Lynn, K. J., & Garcia, M. O. (2015). Cracking the olivine zoning code: Distinguishing between crystal growth and diffusion. *Geology*, *43*(10), 935–938. https://doi.org/10.1130/G37082.1

Shea, T., Ruth, D., Jollands, M., Ohtaki, K., Ishii, H., & Bradley, J. (2023). The presence of silicate melt may enhance rates of cation diffusion in olivine. *Earth and Planetary Science Letters*, *621*, 118370. https://doi.org/10.1016/j.epsl.2023.118370

Shearer, C. K., Aaron, P. M., Burger, P. V., Guan, Y., Bell, A. S., & Papike, J. J. (2013). Petrogenetic linkages among fO2, isotopic enrichments-depletions and crystallization history in Martian basalts. Evidence from the distribution of phosphorus in olivine megacrysts. *Geochimica et Cosmochimica Acta*, *120*, 17–38. https://doi.org/10.1016/j.gca.2013.06.034

Shearer, C. K., Elardo, S. M., Petro, N. E., Borg, L. E., & McCubbin, F. M. (2015). Origin of the lunar highlands Mg-suite: An integrated petrology, geochemistry, chronology, and remote sensing perspective. *American Mineralogist*, *100*(1), 294–325. https://doi.org/10.2138/am-2015-4817

Sonzogni, P. Y., & Treiman, A. H. (2015). Parent magma compositions of the lunar highlands Mg-suite rocks: a melt inclusion perspective. *Lunar Planet. Sci.*, *XLVI*, Abstract-2671. https://ui.adsabs.harvard.edu/abs/2015LPI....46.2671S/abstract

Stewart, D. B. (1975). Apollonian Metamorphic Rocks -- The Products of Prolonged Subsolidus Equilibration. *Abstracts of the Lunar and Planetary Science Conference*, *6*, 774–776.

Stolper, E., & McSween, H. Y. (1979). Petrology and origin of the shergottite meteorites. *Geochimica et Cosmochimica Acta*, *43*(9), 1475–1498. https://doi.org/10.1016/0016-7037(79)90142-X

Strauss, W. A. (2008). *Partial Differential Equations* (S. Corliss, J. Beson, & S. Dumas, Eds.; 2nd ed.). John Wiley & Sons, Inc.

Suhr, G., Hellebrand, E., Johnson, K., & Brunelli, D. (2008). Stacked gabbro units and intervening mantle: A detailed look at a section of IODP Leg 305, Hole U1309D. *Geochemistry, Geophysics, Geosystems*, *9*(10). https://doi.org/10.1029/2008GC002012

Suhr, G., Johnson, K. T., Hellebrand, E., & Brunelli, D. (2008). Stacked Gabbro Units Convert Intervening Mantle to Troctolite in Hole U1309D, IODP Expedition 304/305. *AGUFM*, *2008*, T43B-2020. https://ui.adsabs.harvard.edu/abs/2008AGUFM.T43B2020S/abstract

Tacchetto, T., Reddy, S. M., Saxey, D. W., Fougerouse, D., Rickard, W. D. A., & Clark, C. (2021). Disorientation control on trace element segregation in fluid-affected low-angle boundaries in olivine. *Contributions to Mineralogy and Petrology 2021 176:7*, *176*(7), 1–16. https://doi.org/10.1007/S00410-021-01815-3

Telbisz, T., Kovács, G., Székely, B., & Szabó, J. (2013). Topographic swath profile analysis: A generalization and sensitivity evaluation of a digital terrain analysis tool. *Zeitschrift Fur Geomorphologie*, *57*(4), 485–513. https://doi.org/10.1127/0372-8854/2013/0110

Tsuchiyama, A., Osada, Y., Nakano, T., & Uesugi, K. (2004). Experimental reproduction of classic barred olivine chondrules: Open-system behavior of chondrule formation. *Geochimica et Cosmochimica Acta*, *68*(3), 653–672. https://doi.org/10.1016/S0016-7037(03)00448-4

Turner, F. J. (1968). *Metamorphic Petrology: Mineralogical and Field Aspects* (F. Press, K. Emery, A. Engel, K. Krauskopf, B. Murray, & R. Siever, Eds.; 1st ed.). McGraw-Hill Inc.

Wagner, T. P., & Grove, T. L. (1997). Experimental constraints on the origin of lunar high-Ti ultramafic glasses. *Geochimica et Cosmochimica Acta*, *61*(6), 1315–1327. https://doi.org/10.1016/S0016-7037(96)00387-0

Walker, A. M., Wright, K., & Slater, B. (2003). A computational study of oxygen diffusion in olivine. *Physics and Chemistry of Minerals*, *30*(9), 536–545. https://doi.org/10.1007/s00269-003-0358-7

Warren, H., & Wasson, J. T. (1979). *NO. I REVIEWS OF GEOPHYSICS AND SPACE PHYSICS* (Vol. 17).

Watson, E. B., Cherniak, D. J., & Holycross, M. E. (2015). Diffusion of phosphorus in olivine and molten basalt. *American Mineralogist*, *100*(10), 2053–2065. https://doi.org/10.2138/am-2015-5416

Weeks, E. R., Crocker, J. C., & Weitz, D. A. (2007). Short- and long-range correlated motion observed in colloidal glasses and liquids. *Journal of Physics Condensed Matter*, *19*(20). https://doi.org/10.1088/0953-8984/19/20/205131

Welsch, B., Faure, F., Famin, V., Baronnet, A., & Bachèlery, P. (2013). Dendritic Crystallization: A Single Process for all the Textures of Olivine in Basalts? *Journal of Petrology*, *54*(3), 539–574. https://doi.org/10.1093/petrology/egs077

Welsch, B., Hammer, J., & Hellebrand, E. (2014). Phosphorus zoning reveals dendritic architecture of olivine. *Geology*, *42*(10), 867–870. https://doi.org/10.1130/G35691.1

Williams, D. B., & Carter, C. B. (1996). *Transmission Electron Microscopy*. Plenum Press.

Wirth, R., Dobrzhinetskaya, L. F., & Green, H. W. (2001). Electron microscope study of the reaction olivine +H2O+TiO2 → titanian clinohumite + titanian chondrodite synthesized at 8 GPa, 1300 K. *American Mineralogist*, *86*(5–6), 601–610. https://doi.org/10.2138/am-2001-5-602

Wlotzka, F. (1991). The Meteoritical Bulletin. *Meteoritics*, *71*(3), 255–262. https://doi.org/10.1111/j.1945-5100.1990.tb01004.x

Wong, K., Ferguson, D., Matthews, S., Morgan, D., Tadesse, A. Z., Sinetebeb, Y., & Yirgu, G. (2022). Exploring rift geodynamics in Ethiopia through olivine-spinel Al-exchange thermometry and rare-earth element distributions. *Earth and Planetary Science Letters*, *597*, 117820. https://doi.org/10.1016/j.epsl.2022.117820

Wood, J. A. (1975). Lunar Petrogenesis in a well-stirred magma ocean. *Proc. Lunar Sci. Conf.*, *VI*, 1087–1102. http://articles.adsabs.harvard.edu/cgi-bin/nph-iarticle_query?1975LPSC....6.1087W&defaultprint=YES&filetype=.pdf

Xing, C. M., Wang, C. Y., & Tan, W. (2017). Disequilibrium growth of olivine in mafic magmas revealed by phosphorus zoning patterns of olivine from mafic–ultramafic intrusions. *Earth and Planetary Science Letters*, *479*, 108–119. https://doi.org/10.1016/j.epsl.2017.09.005

Yang, A. Y., Wang, C., Liang, Y., & Lissenberg, C. J. (2019). Reaction Between Mid-Ocean Ridge Basalt and Lower Oceanic Crust: An Experimental Study. *Geochemistry, Geophysics, Geosystems*, *20*(9), 4390–4407. https://doi.org/10.1029/2019GC008368

Yin, Q.-Z., Zhou, Q., Li, Q.-L., Li, X.-H., Liu, Y., Tang, G.-Q., Krot, A. N., & Jenniskens, P. (2014). Records of the Moon-forming impact and the 470 Ma disruption of the L chondrite parent body in the asteroid belt from U-Pb apatite ages of Novato (L6). *Meteoritics & Planetary Science*, *49*(8), 1426–1439. https://doi.org/10.1111/MAPS.12340

Zhou, J. S., Wang, Q., Xing, C. M., Ma, L., Hao, L. L., Li, Q. W., Wang, Z. L., & Huang, T. Y. (2021). Crystal growth of clinopyroxene in mafic alkaline magmas. *Earth and Planetary Science Letters*, *568*, 117005. https://doi.org/10.1016/j.epsl.2021.117005